OPTICAL CHARACTERIZATION OF NON-IMAGING DISH CONCENTRATOR FOR OPTIMIZING INTERCONNECTION OF SOLAR CELLS IN DENSE ARRAY CONCENTRATOR PHOTOVOLTAIC SYSTEM

WONG CHEE WOON

DOCTOR OF PHILOSOPHY IN ENGINEERING

LEE KONG CHIAN FACULTY OF
ENGINEERING AND SCIENCE
UNIVERSITI TUNKU ABDUL RAHMAN
OCTOBER 2016

OPTICAL CHARACTERIZATION OF NON-IMAGING DISH CONCENTRATOR FOR OPTIMIZING INTERCONNECTION OF SOLAR CELLS IN DENSE ARRAY CONCENTRATOR PHOTOVOLTAIC SYSTEM

By

WONG CHEE WOON

A thesis submitted to the Department of Electrical and Electronic Engineering,
Lee Kong Chian Faculty of Engineering and Science,
Universiti Tunku Abdul Rahman,
in partial fulfillment of the requirements for the degree of
Doctor of Philosophy in Engineering
October 2016

ABSTRACT

OPTICAL CHARACTERIZATION OF NON-IMAGING DISH CONCENTRATOR FOR OPTIMIZING INTERCONNECTION OF SOLAR CELLS IN DENSE ARRAY CONCENTRATOR PHOTOVOLTAIC SYSTEM

Wong Chee Woon

Non-uniform solar illumination is one of the key factors that severely restrains electrical performance for the dense array concentrator photovoltaic (DACPV) module consisted of multi-junction solar cells in serial and parallel connection. The non-uniform illumination can cause the DACPV module to encounter significant deterioration in output power due to the current mismatch problem. Addressing this issue, a comprehensive study to optimize the electrical performance of DACPV system comprised of the non-imaging dish concentrator (NIDC) prototype is proposed. A numerical simulation has been developed to analyze the optical characteristics of NIDC by considering imperfection factors, i.e. circumsolar radiation, slope error, and optical misalignment. The simulated results are very useful for the designer to optimize the size of the receiver. From the simulated results, the author can conclude that the three imperfection factors can cause serious deterioration to the uniform illumination distributed on solar cells. Based on the simulated flux distribution, a systematic methodology to optimize the layout configuration of solar cells interconnection circuit in DACPV module has been proposed by minimizing the current mismatch caused by non-uniformity of concentrated sunlight. An

optimized layout of interconnection solar cells circuit with a minimum power loss of 6.5% can be achieved by minimizing the effects of imperfection factors. Last but not least, a high concentrated solar flux scanner has been designed and constructed to acquire flux distribution of the NIDC prototype. The scanner is capable of acquiring high concentrated solar flux distribution up to 1182 suns accurately and rapidly using an array of triple-junction solar cells. A systematic technique has been proposed to analyze the amount of imperfection factors for the NIDC prototype: mirror reflectivity of 0.93, slope error of 3 mrad, circumsolar ratio of 0.1, and optical misalignment angles of 0.2°.

ACKNOWLEDGEMENT

First and foremost, I would like to take this opportunity to express my sincere appreciation and deepest gratitude to my supervisor, Prof. Dr. Chong Kok Keong, for his guidance, invaluable advice, understanding and considerations on my works. I am able to gain many experiences, skills and knowledge from him.

I wish to express my gratitude to Dr. Lau Sing Liong, my co-supervisor. He had provided me continuous guidance, directions and advice when I was conducting my works. I would also wish to indicate special gratitude and deepest thankfulness to my research's partners, Siaw Fei Lu, Yew Tiong Keat, Tan Ming Hui and Tan Woei Chong, for their assistances. Furthermore, I would like to appreciate to none forgetting all of the lab officers and lab assistants, especially Mr. Ho Kok Wai. They always give me support, encouragement, advice, technical expertise and experiences.

To my beloved family, appreciate for the encouragement and mentally support throughout the duration of my study. Last but not the least, with sincere affection and love to my friends, thank you for your friendship, constant encouragement and invaluable help, I wish you all great blessing.

APPROVAL SHEET

This thesis entitled "**OPTICAL CHARACTERIZATION OF NON-IMAGING DISH CONCENTRATOR FOR OPTIMIZING INTERCONNECTION OF SOLAR CELLS IN DENSE ARRAY CONCENTRATOR PHOTOVOLTAIC SYSTEM**" was prepared by WONG CHEE WOON and submitted as partial fulfillment of the requirements for the degree of Doctor of Philosophy in Engineering at Universiti Tunku Abdul Rahman.

Approved by:

_____
(Prof. Dr. Chong Kok Keong)
Date:……..
Supervisor
Department of Electrical and Electronic Engineering
Lee Kong Chian Faculty of Engineering and Science
Universiti Tunku Abdul Rahman

_____
(Dr. Lau Sing Liong)
Date:……..
Co-supervisor
Department of Electrical and Electronic Engineering
Lee Kong Chian Faculty of Engineering and Science
Universiti Tunku Abdul Rahman

LEE KONG CHIAN FACULTY OF ENGINEERING AND SCIENCE

UNIVERSITI TUNKU ABDUL RAHMAN

Date: 7 October 2016

SUBMISSION OF THESIS

It is hereby certified that **WONG CHEE WOON** *(*ID No: **11UED02576**) has completed this thesis entitled "**OPTICAL CHARACTERIZATION OF NON-IMAGING DISH CONCENTRATOR FOR OPTIMIZING INTERCONNECTION OF SOLAR CELLS IN DENSE ARRAY CONCENTRATOR PHOTOVOLTAIC SYSTEM**" under the supervision of **Prof. Dr. CHONG KOK KEONG** (Supervisor) from the Department of Electrical and Engineering, Lee Kong Chian Faculty of Engineering and Science, and **Dr. LAU SING LIONG** (Co-Supervisor) from the Department of Electrical and Engineering, Lee Kong Chian Faculty of Engineering and Science.

I understand that University will upload softcopy of my thesis in pdf format into UTAR Institutional Repository, which may be made accessible to UTAR community and public.

Yours truly,

_____

(Wong Chee Woon)

DECLARATION

I hereby declare that the dissertation is based on my original work except for quotations and citations which have been duly acknowledged. I also declare that it has not been previously or concurrently submitted for any other degree at UTAR or other institutions.

Name: Wong Chee Woon

Date: 7 October 2016

TABLE OF CONTENTS

LIST OF TABLES

LIST OF FIGURES

LIST OF ABBREVIATIONS

ADC	Analog-to-Digital Converter
CCD	Charge-Coupled Device
CLFR	Compact Linear Fresnel Reflector
CPV	Concentrator Photovoltaic
CSR	Circumsolar Ratio
DACPV	Dense Array Concentrator Photovoltaic
DNI	Direct Normal Irradiance
GSI	Global Solar Irradiance
I-V	Current-Voltage
NIDC	Non-Imaging Dish Concentrator
NIPC	Non-Imaging Planar Concentrator
P-V	Power-Voltage
RMSD	Root-Mean-Square Deviation
SCR	Solar Concentration Ratio
SOE	Secondary Optical Element
UTAR	Universiti Tunku Abdul Rahman
VMJ	Vertical Multi-junction

CHAPTER 1

INTRODUCTION

1.1 Research Background and Motivation

The depletion of fossil fuels and global warming issues have pressed mankind to explore alternative sources of energy that are safe, clean and renewable. At present, the research and development of concentrator photovoltaic (CPV) systems for converting highly concentrated solar energy into electrical energy have been expanded rapidly. CPV systems not only have the potential for reducing the cost of solar electricity, but they are also able to reduce the dependence of the existing power generation systems on fossil and nuclear fuels consumptions (Nishioka et al., 2006; Philipps et al., 2012).

The prompt growth of CPV system is mainly due to the encouragement of multi-junction solar cells that are capable of attaining high electrical conversion efficiency of 46% (Green et al., 2015; Kurtz and Emery, 2015). The cell consists of three or more materials connected in series by using monolithic approach or mechanically stacked approach in which different materials are sensitive to the different ranges of solar spectrum (Bett et al., 2007; Philipps et al., 2012). In practice, there are several parasitic power losses to be considered in a CPV system, such as power consumption for tracking system, cooling system, measurement and data acquisition system.

These parasitic, wiring and inverter losses have caused the AC output efficiency of CPV system to drop down to a range from 25 % to 29 % (Philipps et al., 2015).

For the sake of achieving high electrical conversion efficiency, solar concentrators that are made of relatively inexpensive optics, such as mirrors or lenses, have been developed to focus solar irradiance on the multi-junction solar cells ranging from hundreds to thousands of solar concentration ratio (SCR). Lenses or mirrors in the CPV system will replace most of the solar cell material, and the price of both is taken into account for determining the optimum configuration. The price of the solar concentrator is commonly lower than that of solar cells, and hence, efforts have been put into finding ways for lowering the manufacturing cost using various types of solar concentrators to develop a CPV system (Chong et al., 2013a; Tan et al., 2014). Therefore, the motivation behind developing solar concentrator is to offset the cost of expensive semiconductor material and encourage CPV system installations.

With the different types of solar concentrators in use, the receiver of a concentrator can be configured in either individual solar cell receiver or dense array solar cells receiver. The receiver configurations are dependent on the area of focused sunlight. For individual cell receiver, the area of focused sunlight that is incident on the solar cell is about the same as the active area of single solar cell. The single cell typically only needs passive cooling. For dense array solar cells receiver, the area of focused sunlight is much larger than the active area of one solar cell. A dense array solar cells receiver

basically comprises an array of solar cells that are connected in series and parallel to convert the highly concentrated solar energy into electrical energy. Due to the larger focused sunlight area, active cooling is necessary to keep the densely packed receiver from reaching unacceptable temperatures. The most important advantage of using dense array solar cells receiver compared to single cell receiver is that it is capable of producing additional thermal energy owing to the need for active cooling. The integration of both solar electricity and solar hot water maximizes the economic and environmental value of energy harvested from the sun (Sharaf and Orhan, 2015).

1.2 The Challenges

In fact, the performance of the multi-junction solar cells has a major discrepancy between the provided testing conditions and the real operating conditions. For example, the given cell characterizations are measured under AM1.5D, uniform illumination with high SCR and operating temperature of 25 °C. It is a strenuous task to achieve these conditions in the real operation of CPV module on-site that are equipped with multi-junction solar cells. In the real operating conditions, several factors are restraining the electrical performance of solar cells, particularly the non-uniform illumination that causes current mismatch in the dense array concentrator photovoltaic (DACPV) module that consists of bypass diodes and multi-junction solar cells that are connected in series and parallel (Faiman et al, 2002; Franklin and Coventry, 2002; Andreev et al., 2003; Sherif et al., 2003; Coventry, 2005;

Nishioka et al., 2006). When non-uniform illumination is focused on the module, there will be a significant drop in efficiency as compared with the module that is operated under uniform illumination (Andreev et al., 2003; Nishioka et al., 2006; Verlinden et al., 2006). The non-uniform illumination distributed on the solar cells is mainly caused by optical design limitations, optical misalignment, low tracking accuracy, circumsolar radiation and the condition of the refractive lens or reflecting mirrors. (Baig et al., 2012).

1.3 Objectives

In order to overcome the above-identified non-uniform illumination problem, a systematic and comprehensive study on non-imaging dish concentrator (NIDC) for the application in DACPV system has been developed and explored. The main objectives are as follows:

1. To design and construct a prototype of the non-imaging dish concentrator for the application in dense array concentrator photovoltaic system.
2. To study the optical characteristics of the non-imaging dish concentrator with the use of ray-tracing numerical simulation technique by considering circumsolar radiation, mirror surface slope error and optical misalignment.

3. To develop a systematic method for optimizing the electrical interconnection of solar cells in dense array concentrator photovoltaic module configuration to achieve the maximum output power.
4. To design and construct a high concentrated solar flux scanner for measuring the solar flux distribution of the non-imaging dish concentrator prototype to validate the numerical simulation results.

1.4 Contributions

The design and construction of cost effective NIDC have been presented in this study. Instead of using a single piece of the costly parabolic dish, the NIDC comprises multi-faceted flat mirrors act as an optical aperture to collect and to focus the incident sunlight at the target with any focal distance along the optical axis. All the flat facet mirrors are used to superimpose the sunlight at the receiver, which can produce a reasonably high SCR and much more uniform solar illumination distributed on the solar cells. The optical losses of NIDC are less as compared to Fresnel lens system.

Besides, a systematic computational algorithm to study the effects of imperfection factors, i.e. circumsolar radiation, mirror surface slope error and optical misalignment, to the solar flux distribution of NIDC has been developed by using numerical simulation method. A comprehensive analysis of solar flux distribution at the target has been carried out by considering all the important criteria to improve the overall performance of DACPV system,

such as the maximum SCR, uniform illumination area, and spillage loss. With the simulated solar flux distribution, the receiver size can be optimized by minimizing the spillage loss of the DACPV system.

Despite the employment of flat facet mirrors in the NIDC, the resultant flux distribution from simple super-positioning of all the reflected sunlight is inevitably non-uniform near the peripheral area. Instead of using non-conventional solar cells, which incur extra cost and complexity, a systematic methodology to optimize the layout configuration of solar cells interconnection circuit in DACPV module has been proposed by minimizing the current mismatch caused by non-uniformity of concentrated sunlight.

A concentrated solar flux scanner equipped with an array of triple-junction solar cells has been constructed to measure the solar irradiance across a receiver plane of NIDC prototype. The flux scanner can perform real time and direct measurement of high concentrated solar flux distribution profile with a good degree of accuracy and fast scanning speed. The measured solar flux profile can be used to validate the numerical simulation that is specially designed for modeling the solar flux distribution and optimizing the electrical interconnection of DACPV module. Furthermore, the advantage of this technique is that the triple-junction solar cells as transducer mounted on the scanner is the same type as that of assembled in the DACPV module. It has simplified post-processing layout design of the solar cell interconnection circuit in the DACPV module because the short-circuit currents of solar cells

in their particular locations on the receiver have been measured directly via the scanner.

1.5 Outline of the Thesis

The organization of the thesis is outlined as follows:

- Chapter 1 of this thesis gives an introduction to the research background and motivation in developing CPV systems. This section also identifies the challenges in the development of CPV system. Besides, the project objectives and contributions are clarified in this chapter.

- At first, Chapter 2 gives an introduction to the effects of non-uniform illumination in CPV System. Next, a literature review about the various types of solar concentrators and the alternative techniques of overcoming inhomogeneous illumination in CPV system are presented. In addition, the techniques to measure solar flux distribution, which can be classified as direct and indirect measurement methods, are reviewed.

- In Chapter 3, the design and development methodology of NIDC are discussed in detail including the setup of NIDC prototype and the design of sun-tracking system.

- In Chapter 4, the numerical simulation using ray-tracing technique is presented for the modeling of solar flux distribution on the receiver of NIDC prototype. The modeling is carried out by considering various imperfection factors, i.e. circumsolar ratio, mirror surface slope error and optical misalignment. The simulated solar flux distribution results are also analyzed in detail.

- At the beginning of Chapter 5, the principle of optimizing the circuit layout of solar cells interconnection is discussed in detail including the modeling of DACPV module. The electrical performance of the optimized layout of interconnection solar cells circuit is also discussed in this chapter.

- In Chapter 6, the hardware and software designs of the high concentrated solar flux scanner are explained in detail. The measured solar flux profile is also compared with the modeled solar flux profile.

- Chapter 7 ends the thesis with the conclusions and future works. The thesis concludes with the outcomes of the overall research achievements and the advantages of the developed system.

1.6 Publications

Based on the findings from this research, several papers have been published in peer-reviewed journals and international conference proceedings. A full list of publications is presented in Table 1.1.

Table 1.1: Papers that are published in peer-reviewed journals and international conference proceedings.

No.	Paper Title	Year	Journal/ Conference	Impart Factor
1	"Analytical Model of Non-Imaging Planar Concentrator for the Application in Dense-Array Concentrator Photovoltaic System" **(Presented and Published)**	2013	1st International Symposium on Innovative Technologies for Engineering and Science	N/A
2	"Flux Distribution Analysis of Non-Imaging Planar Concentrator Considering Effects of Circumsolar Radiation and Mirror Slope Error" **(Presented and Published)**	2014	Light Energy and the Environment Congress	N/A
3	"Performance Optimization of Dense-Array Concentrator Photovoltaic System Considering Effects of Circumsolar Radiation and Slope Error" **(Published)**	2015	Optics Express	3.488
4	"Solar Flux Distribution Study of Non-Imaging Dish Concentrator Using Linear Array of Triple-Junction Solar Cells Scanning Technique" **(Published)**	2016	Solar Energy	3.469

CHAPTER 2

LITERATURE REVIEW

2.1 Introduction

To further reduce the cost of CPV power generation systems, optimal system design is necessary so that maximum solar energy can be harnessed from the solar cells (Luque et al., 2006; Nishioka et al., 2006). However, we often find that the delivered electrical power in field conditions is much lower than the array ratings because mismatch losses have affected the current-voltage (*I*-*V*) and power-voltage (*P*-*V*) curves of the solar cells. Mismatch factors such as soiling, non-uniform irradiance, shading, temperature variations, cell's quality as well as aging of solar cells, all contribute to serious array power reduction in real site testing (Kaushika and Rai; 2007; Picault e al., 2010; Baig et al., 2012).

2.2 Effects of Non-Uniform Illumination in CPV System

Non-uniform distribution of concentrated solar irradiance is one of the most significant problems faced by most of CPV systems, especially around the receiver edges, mainly caused by optical design limitations, structure misalignment, and low tracking accuracy (Baig et al., 2012). Over the recent

years, many studies can be found discussing on the improvement of solar concentrator optical design to produce more uniform solar illumination at high concentrations (Chong et al., 2013a). Nevertheless, the overall output current of multi-junction cells connected in a dense array arrangement is very much dependent on the solar flux distribution of a solar concentrator. Due to factors such as sun-shape, circumsolar effect, aberration, imperfection of mirror's geometry, etc., it is impossible to produce perfect uniform illumination on the dense array concentrator photovoltaic (DACPV) receiver and hence causing a significant loss in the overall output power and average conversion efficiency (Faiman et al, 2002; Franklin and Coventry, 2002; Andreev et al., 2003; Sherif et al., 2003; Coventry, 2005; Nishioka et al., 2006).

In recent years, researchers have presented several approaches to study the effects of non-uniform illumination on the performance of solar cells. For example, Reis et al. (2013) introduced a distributed diode model for solar cells to predict the behavior of solar cells that are integrated into CPV systems. The modeling showed that there is a power loss when solar cells operate under conditions of inhomogeneous distribution of temperature and illumination. Furthermore, Cooper et al. (2013) have experimentally validated a model with a linear semi-dense array of five series-connected triple-junction concentrator cells. Under the worst-case conditions of non-uniform illumination on the array, the efficiency of the array drops to 28.5% as compared to 39% for the case of perfect uniformity.

2.3 Optical Design of Solar Concentrators

Solar concentrator plays a vital role in the research and development of CPV power generation system. The solar concentrator makes use of geometrical optics in the design of reflective or refractive types of concentrating devices to focus the solar flux onto a receiver module equipped with multi-junction solar cells (Chong et al., 2013b). Generally, solar concentrators can be categorized into two major groups: imaging concentrator and non-imaging concentrator (Winston et al., 2005; Heinloth, 2006; Luque and Andreev, 2007). Despite being widely used in optics applications such as astronomical telescope and camera, the imaging concentrator does not aim to produce uniform flux distribution profile at the receiver that is highly required in the DACPV module (Chong et al., 2010). The DACPV module that receives non-uniform solar illumination will face a severe drop in efficiency due to the current mismatch problem as opposed to the module under uniform solar illumination (Andreev et al., 2003; Nishioka et al., 2006; Verlinden et al., 2006).

How to form a uniform solar illumination on the solar cells is a great challenge for the researchers who are working in CPV power generation system. In recent years, several researchers have paid a lot of efforts to design various types of solar concentrators for producing a uniform distribution of solar radiation on the solar cells.

2.3.1 Parabolic Dish Concentrator

Over the last few decades, a parabolic dish concentrator has been widely used for solar energy applications, especially for applications involving high solar concentration and high-temperature collection. For a large dish concentrator system, using a single parabolic mirror as a reflector is costly due to the special technology needed to fabricate special mirrors with a thickness from 0.7 to 1.0 mm and to obtain the parabolic shape (Kussul et al., 2008). For a large collective area of parabolic dish concentrator, multi-faceted spherical or concave mirrors are arranged on the approximate parabolic shape structure as a reflector instead of using a single piece of the parabolic reflector (Johnston et al., 2003; Ulmer et al., 2008). Despite alignment of mirrors being required in a faceted parabolic concentrator, its fabrication is cheaper and simpler as compared with a single precise parabolic reflector.

The implementation of a parabolic concentrator in a DACPV system encounters the difficulty to produce good uniformity of solar illumination on the receiver, but instead the tendency is more toward Gaussian type solar flux distribution (Johnston et al., 2003; Ulmer et al., 2008). Figure 2.1 shows a non-uniform solar illumination of a parabolic dish solar concentrator produced by Zenith Solar (Lockenhoff et al., 2010). The Gaussian-shaped solar flux distribution may cause the DACPV module encounters a severe drop in efficiency due to the current mismatch problem.

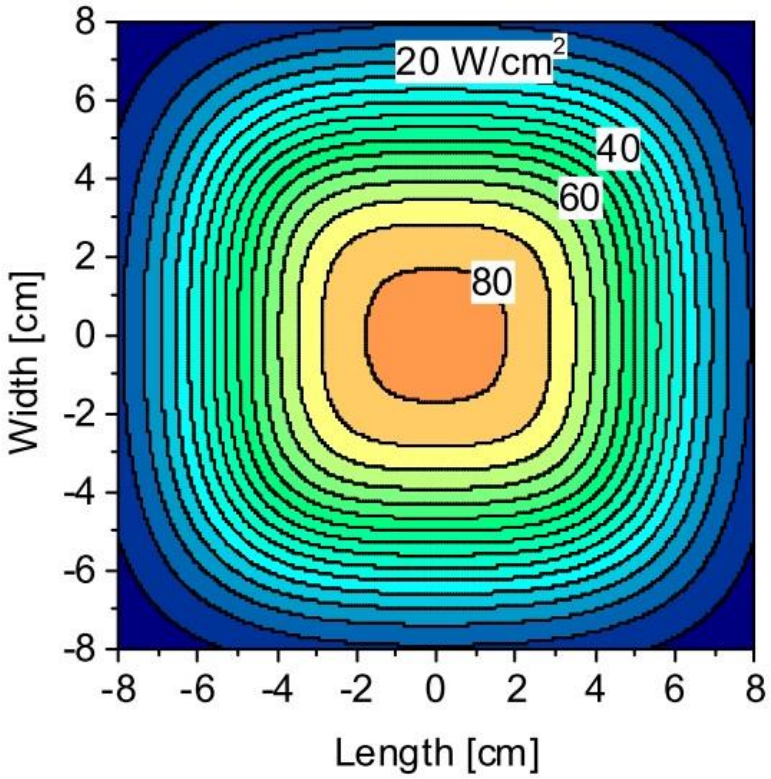

Figure 2.1: Non-uniform solar illumination of a parabolic dish solar concentrator (Lockenhoff et al., 2010).

In order to solve the current mismatch problem, two-stage solar concentrators that comprise a parabolic dish and secondary optics or homogenizer have been introduced for the application of a CPV system (Segev and Kribus, 2013; Wang et al. 2013). Ries et al. (1997) have introduced a solar concentrator comprised of a paraboloidal dish and a second-stage kaleidoscope flux homogenizer. According to Figure 2.2, the proposed two-stage solar concentrator is capable of producing uniform irradiance on the solar cell receiver. However, the introduction of an additional optical device will inflict additional losses, which can reach 10% or more for typical designs as well as additional cost and complexity (Kreske, 2002).

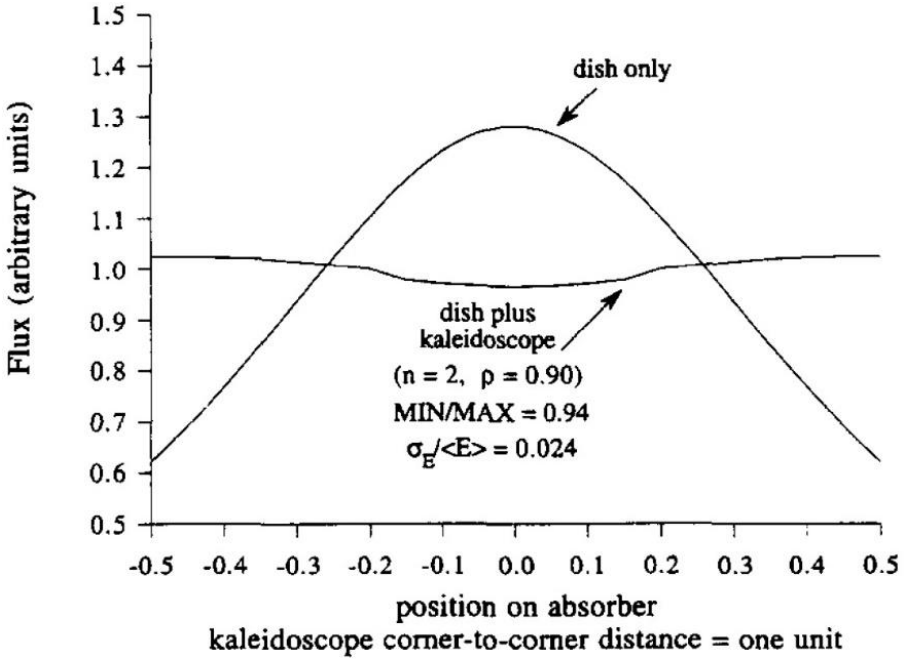

Figure 2.2: A comparison of irradiance distribution using paraboloidal-dish only and paraboloidal-dish plus kaleidoscope flux homogenizer (Ries et al., 1997).

2.3.2 Fresnel Concentrator

Besides the aforementioned parabolic dish concentrators, researchers have proposed various kinds of Fresnel concentrators for the sake of producing uniform solar flux distribution on the solar cells, which can be classified as Fresnel reflector and Fresnel lens (Chong et al., 2013). Mills and Morrison (2002) advocated the use of an advanced form of compact linear Fresnel reflector (CLFR) that can produce a better uniformity of solar irradiation compared to parabolic trough or parabolic dish systems. However, the SCR for linear Fresnel reflector is normally lower than 100 suns (Chong et al., 2010; Tan et al., 2014).

In Fresnel lens system, an additional secondary optical element (SOE) such as flux homogenizer is needed to produce uniform solar flux distribution, since the conventional Fresnel lenses always focus a collimated beam to a point, as presented in Figure 2.3 (Ota and Nishioka, 2012). This approach is capable of cutting down the expensive solar cell area by increasing the SCR and the light intensity. However, there are some other factors causing the inhomogeneous illumination distributed on the solar cells, such as tracking error, misalignment of the concentrator and the condition of the refractive lens or reflecting mirrors (Baig et al., 2012; Chong et al., 2013).

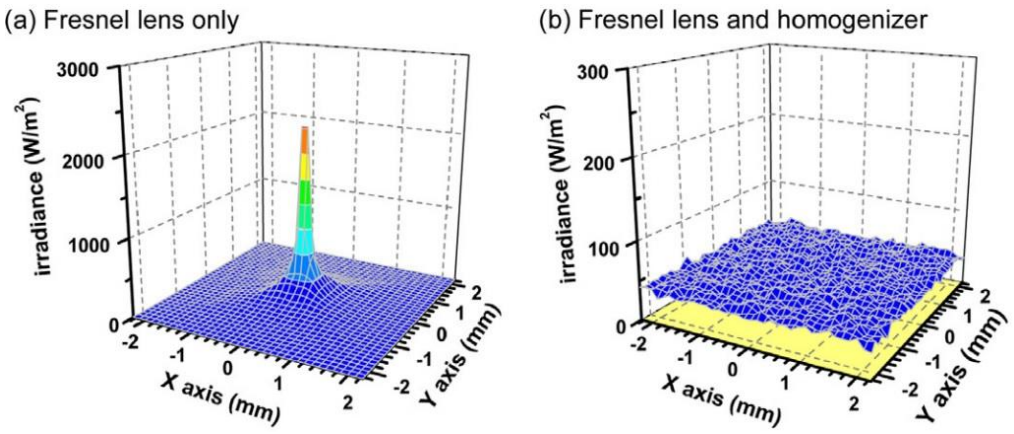

Figure 2.3: A comparison of simulated irradiance distribution on the solar cell using Fresnel lens only and Fresnel lens plus homogenizer (Ota and Nishioka, 2012).

Ryu et al. (2006) introduced a modular Fresnel concentrator for achieving moderate SCR (several hundreds of suns) and better uniform solar illumination on the solar cell. Figure 2.4 shows the superposition concept of modular Fresnel lenses for CPV system. Each modular Fresnel lens refracts the incident sunlight onto the targeted solar cell. Conversely, the transmission

efficiency of the modular Fresnel lenses is less than 80% due to the absorption by the lens material and the reflection at the surface of the lens (Chong et al., 2010; Tan et al., 2014).

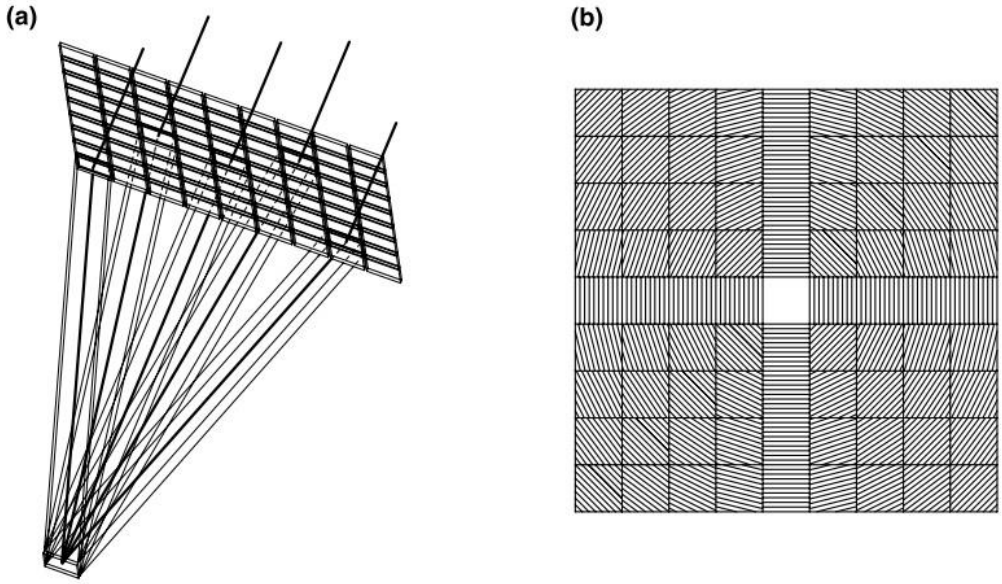

Figure 2.4: Diagrams that describe the superposition concept of modular Fresnel lenses for CPV system. (a) 3-D view of the concentration optics, and (b) top view of modularly faceted Fresnel lenses (Ryu et al., 2006).

2.3.3 Non-Imaging Planar Concentrator

Alternatively, Chong et al. (2009b; 2010) proposed a non-imaging planar concentrator (NIPC) consisting of numerous flat facet mirrors, which are arranged in a square array and spaced evenly at the same height. The planar concentrator applies the concept of non-imaging optics to concentrate the sunlight. This concentrator is an on-axis focusing device, with the target placed at the focal point. In this scheme, the resulted SCR is the algebra sum

of the solar flux reflected from the mirrors without creating a specific optical image. By superimposing the sunlight at the receiver, NIPC can produce a reasonably high SCR and uniform solar irradiance. The conceptual layout design of NIPC is illustrated in Figure 2.5 (Chong et al., 2010).

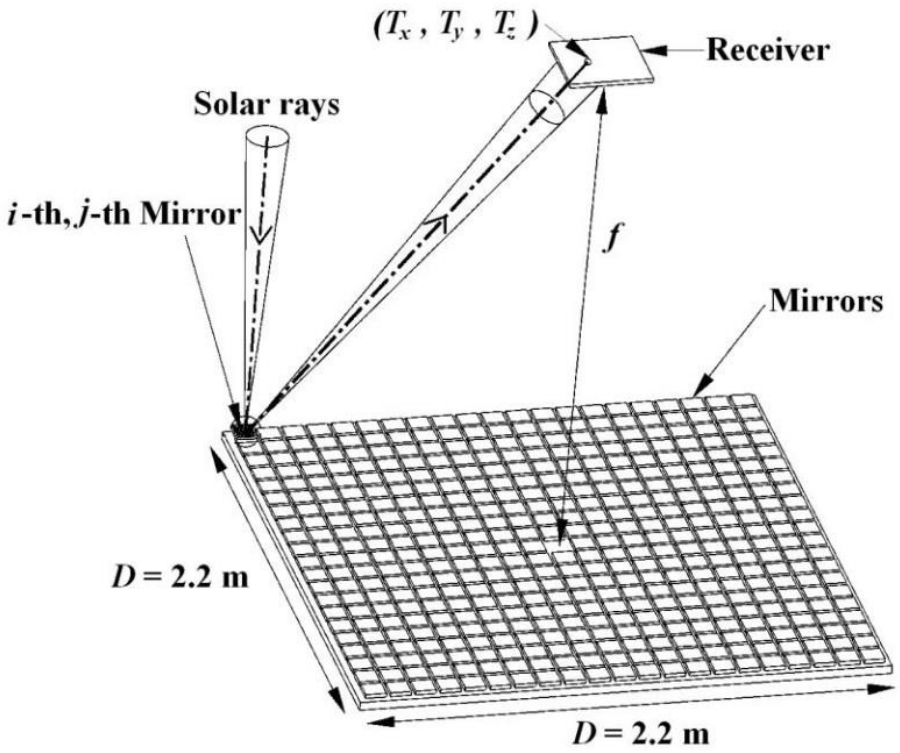

Figure 2.5: Conceptual layout design of the NIPC (Chong et al., 2010).

As shown in Figure 2.6, for those facet mirrors especially located further from the center of the NIPC, higher tilting angles are required to reflect sunlight toward the common target, but it will cause more sunlight directed from an adjacent facet mirror to be blocked (Tan et al., 2014). As the distance of the facet mirror from the center of the concentrator increases, the sunlight blocking effect among the adjacent mirrors becomes worse due to large tilted angles.

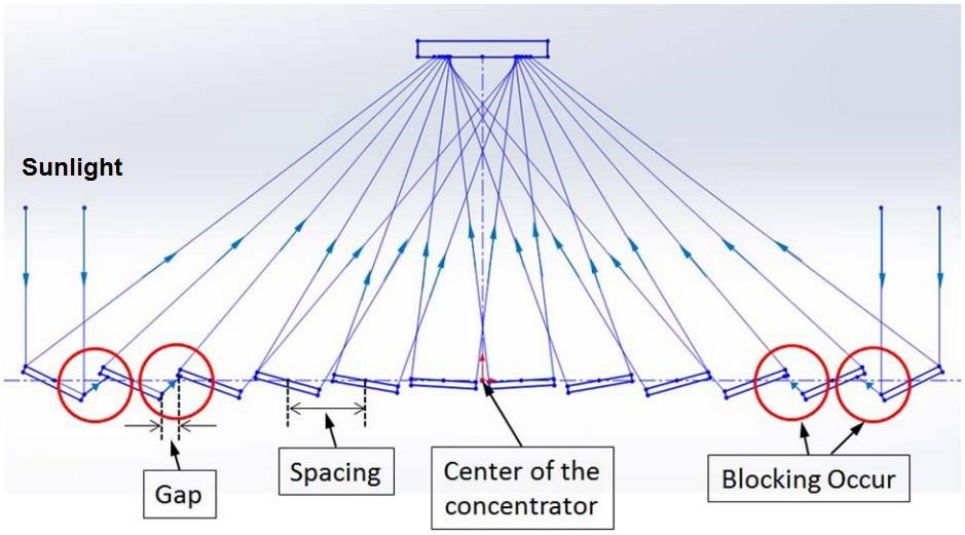

Figure 2.6: A Cross-sectional view of the planar concentrator. Blocking effect starts to occur in the fifth row of the facet mirror counting from the center of the concentrator (Tan et al., 2014).

2.4 Non-Conventional Solar Cells

Another technique of overcoming inhomogeneous illumination to increase CPV system performance is by refining optical mismatch via implementing unconventional geometry of solar cells (Siaw et al., 2014). These solar cells are custom designed for a specific type of solar concentrator according to the solar illumination profile.

2.4.1 Radial Solar Cells Receiver

In order to improve optical mismatch on the solar cells, Vivar et al. (2009) introduced a radial large area Si-cell receiver with secondary optics that uses custom-made solar cells. The radial Si-cell receiver can divide the incident solar irradiance evenly between the solar cells, as presented in Figure 2.7. As compared to the solar cells connected in series interconnection, the custom-shaped solar cells that assembled in parallel interconnection can decrease the losses from inhomogeneous illumination and optical misalignment by nearly 6 times lesser (Vivar et al., 2010). However, this method is still vulnerable to tracking errors and optical misalignment (Siaw and Chong, 2013).

Figure 2.7: Radial large area Si-cell receiver with secondary optics (Vivar et al., 2009).

2.4.2 Solar Cells with Different Geometries

AZUR SPACE Solar Power GmbH also custom designed dense array module comprises four different geometries of solar cells for the application in CPV systems (Lockenhoff et al., 2010). The custom-shaped solar cells are arranged in such a way that compensates non-uniform solar flux distribution. As shown in Figure 2.8, wider parts of solar cells are utilized to compensate the outer segment of the dense array module that receives lesser solar flux. This technique is able to compromise optical mismatch on the dense array modules, but it involves higher investment cost since there are many uniquely-sized solar cells in the module.

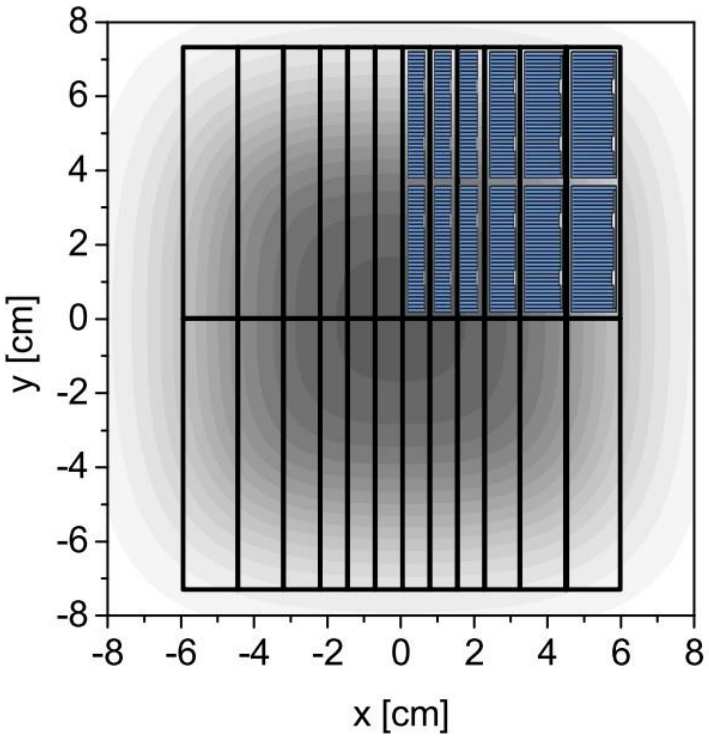

Figure 2.8: Dense array module with four different geometries of solar cells that compensate the non-uniform solar flux distribution. (Lockenhoff et al., 2010).

2.4.3 High-Voltage Solar Cells

Recently, Segev and Kribus (2013) have presented high-voltage Silicon Vertical Multi-junction (VMJ) solar cells that can accept high solar concentration with an efficiency close to 30%. Figure 2.9 shows the VMJ solar cells are designed for parallel interconnection in a dense array module. With a parallel interconnection, voltage matching rather than series matching is attempted to reduce the current mismatch losses under inhomogeneous illumination. Despite the VMJ solar cells show better tolerance to inhomogeneous illumination, a dense array module that is fully interconnected in parallel can induce high resistive losses.

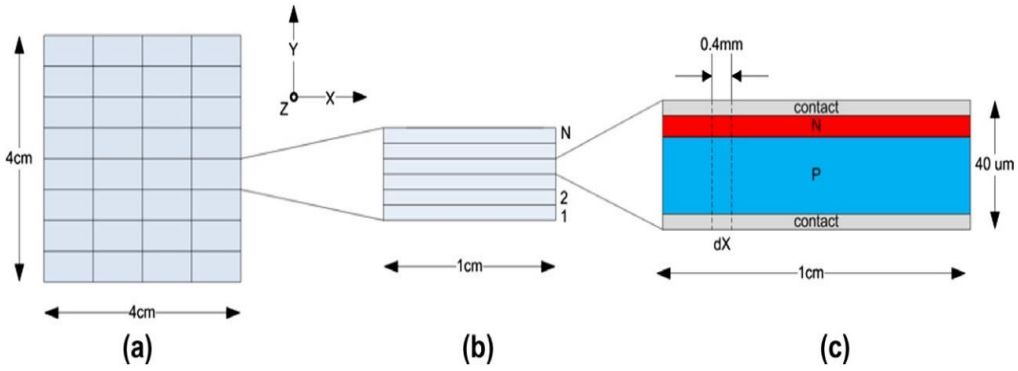

Figure 2.9: (a) The module; (b) a VMJ cell made of N vertical junctions connected internally in series; (c) a single vertical junction and its segment of length *dx* (Segev and Kribus, 2013).

2.5 Techniques to Measure Solar Flux Distribution

The major challenge for achieving high performance of DACPV module is the non-uniform illumination that results in the current mismatch among the cells connected in series. For that reason, an accurate measurement is necessary to obtain the high SCR profile for each location of the solar cell on the receiver of the solar concentrator. The high SCR profile can be used to validate the numerical simulation that is specially designed for modeling the solar flux distribution and optimizing the electrical interconnection of DACPV module.

How to measure high concentrated solar flux distribution accurately is an onerous challenge for the researchers who are working in solar facilities. In recent years, several research laboratories have paid great efforts to design various types of instruments for measuring the high concentration solar flux distribution, which can be classified as direct and indirect measurement methods (Röger et al., 2014).

2.5.1 Direct Measurement Method

In the direct measurement method, Gardon type calorimeter, also known as a thermo gauge, is the most commonly used heat flux sensor that directly delivers a measurement signal proportional to the solar flux. Estrada et al. (2007) developed a calorimeter with the utilization of the cold water

calorimetry technique for measuring the concentrated solar flux produced by a point focus solar concentrator. The solar flux was measured via determining the heat absorbed by a cooling fluid circulated through the calorimeter (see Figure 2.10). To estimate the concentrated solar flux, a balance between the energy absorbed by the fluid and the solar energy focuses on the calorimeter was carried out. In overall, calorimeter is employed to measure thermal radiation, and a series of special calibration to the solar radiation spectrum is carried out with the heat radiation from a blackbody at 850 ℃ (Ballestr ń et al., 2003; Ballestr ń et al., 2004; Parretta et al., 2007; Fernández-Reche et al., 2008).

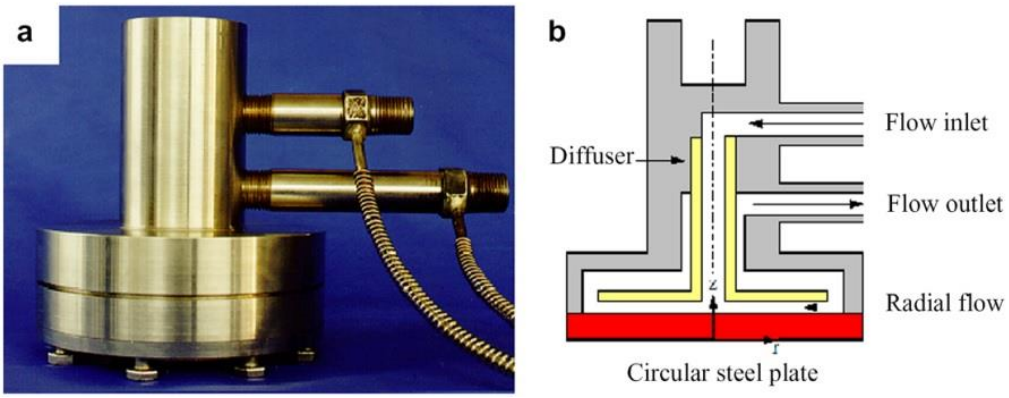

Figure 2.10: (a) A picture of the flat plate calorimeter and (b) cross-sectional diagram to show how the solar flux was measured via determining the heat absorbed by a cooling fluid circulated through the calorimeter (Estrada et al., 2007).

2.5.2 Indirect Measurement Method

As for indirect measurement method, charge-coupled device (CCD) cameras are applied to evaluate the sunlight intensity distribution on the receiver of solar concentrator via light scattering technique (Röger et al., 2014). Parretta et al. (2006) made use of CCD camera for the acquisition of the scattered light from the Lambertian diffuser that took in place of the illuminated receiver (see Figure 2.11). The spatial distribution of intensity radiation was then numerically derived from the received image via a proprietary code.

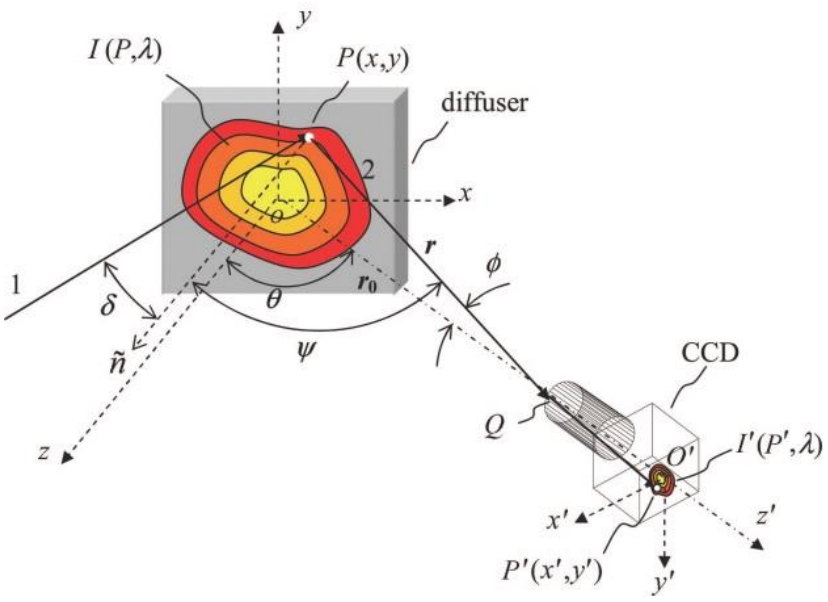

Figure 2.11: Schematic diagram to show the light-scattering–CCD method applied to a Lambertian planar diffuser. (Parretta et al., 2006).

Besides, Haueter et al. (1999) and Ulmer et al. (2002) can measure ultra-high concentrated sunlight up to 5,000 suns and 12,000 suns respectively by using appropriate combinations of neutral density filters and cooling devices. Despite the CCD camera having fast response time, flux gauges or calorimeters were required for the calibration of brightness maps provided by the CCD cameras (Röger et al., 2014; Salomé et al., 2013).

CHAPTER 3

DESIGN AND CONSTRUCTION OF NON-IMAGING DISH CONCENTRATOR

3.1 Introduction

Inspired by adopting the merit ideas from both NIPC (to produce reasonably uniform illumination with the use of flat facet mirrors) and parabolic dish concentrator (to avoid the sunlight blocking and shadowing effects with the geometry gradually increase in height), the author and his research teammates have proposed the non-imaging dish concentrator (NIDC) with single-stage focusing by extracting the best designs from both solar concentrators (Chong et al, 2012b; Chong et al, 2013b; Tan et al, 2014). The proposed NIDC is an optical device that is specially designed for the application in DACPV system, which requires uniform flux distribution on the receiver.

3.2 Principle of NIDC

To achieve a good uniformity of the solar irradiation with a reasonably high SCR on the target, a NIDC has been proposed by applying the concept of non-imaging optics to concentrate the sunlight. The NIDC is formed by

numerous square flat mirrors act as the optical aperture to collect and to focus the incident sunlight into a target. The conceptual layout design of the NIDC is illustrated in Figure 3.1. The idea of concentrating the sunlight in the NIDC is similar to that of NIPC, where the uniform flux distribution on the target can be acquired from the superposition of the reflected sunlight. In this design, the incident sunrays are reflected by an array of identical flat mirrors to the target, in which their size and shape are nearly same as that of the receiver. In order to eliminate blocking and shadowing effects from the adjacent facet mirrors, Tan et al. (2014) introduced a computational algorithm to determine the facet mirrors configuration for the NIDC. The NIDC geometry was designed according to the proposed algorithm. As shown in Figure 3.1, the facet mirrors are gradually lifted from central to peripheral regions of the dish concentrator.

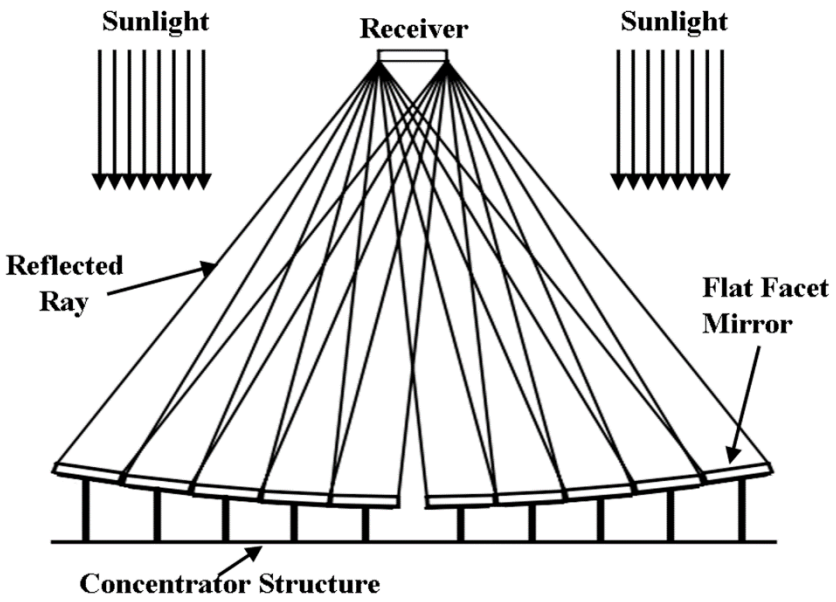

Figure 3.1: Conceptual layout design of the NIDC. All the flat facet mirrors are gradually lifted from central to peripheral regions of the concentrator to prevent shadowing and blocking among adjacent mirrors.

3.3 Prototype of NIDC

Figure 3.2 shows the prototype of NIDC located in Universiti Tunku Abdul Rahman (UTAR), Kuala Lumpur campus, Malaysia (3.22° North, 101.73° East). This prototype is capable of producing much more uniform spatial irradiance for the application in DACPV system. Instead of using a single piece of the parabolic dish, the NIDC consisting of multi-faceted mirrors act as the optical aperture to collect and to focus the incident sunlight at the common receiver that is placed at a focal distance of 210 cm.

Figure 3.2: The prototype of NIDC located in Universiti Tunku Abdul Rahman (UTAR), Kuala Lumpur campus, Malaysia (3.22° North, 101.73° East).

3.3.1 Hardware Design

The structure of the dish concentrator can be divided into two main components: concentrator frame and flat facet mirror sets. The main material that is selected for constructing the solar concentrator frame is 20 mm × 20 mm square hollow aluminum bars with a thickness of 1 mm. The hollow bar is preferred because of weather resistant, significant savings in raw material cost and light weight compared to the solid bar. Because of that, the concentrator frame will not apply much load on the turning mechanism, and subsequently, eases the process of structure development. Sections of the square hollow steel bars are joined in vertically and horizontally to form the concentrator frame. Another structure, which is the target supporter, is built by using two sets of square hollow bars. The target is fixed at a focal point with the distance of 210 cm away from the center of solar concentrator frame.

Figure 3.3 shows the prototype consists of 96 flat facet mirror sets to be arranged into ten rows and ten columns on the concentrator frame. Four mirror sets in the central region of concentrator are omitted due to the shading by the receiver. Flat facet mirrors with a dimension of 20 cm × 20 cm and a thickness of 0.3 cm are selected to form a total reflective area of 3.84 m^2. There is a gap spacing of 0.5 cm in between the mirrors. This gap will avoid any possible blocking when the mirrors are tilted and can also reduce the wind pressure on the concentrator frame. Besides, the flat facet mirror sets consist of several other components, namely, the compression springs, machine screws, silicone pastes and wing nuts (Chong et al., 2009b). The idea of this

design is for the presetting of each mirror along the row and column directions. There are three contact points in each of this screw–spring assembly from which one of them acts as the pivot point, and the remaining two are adjustable points. Each mirror can thus be freely tilted to focus sunlight onto the target by turning the nuts of the adjustable screw–spring sets manually.

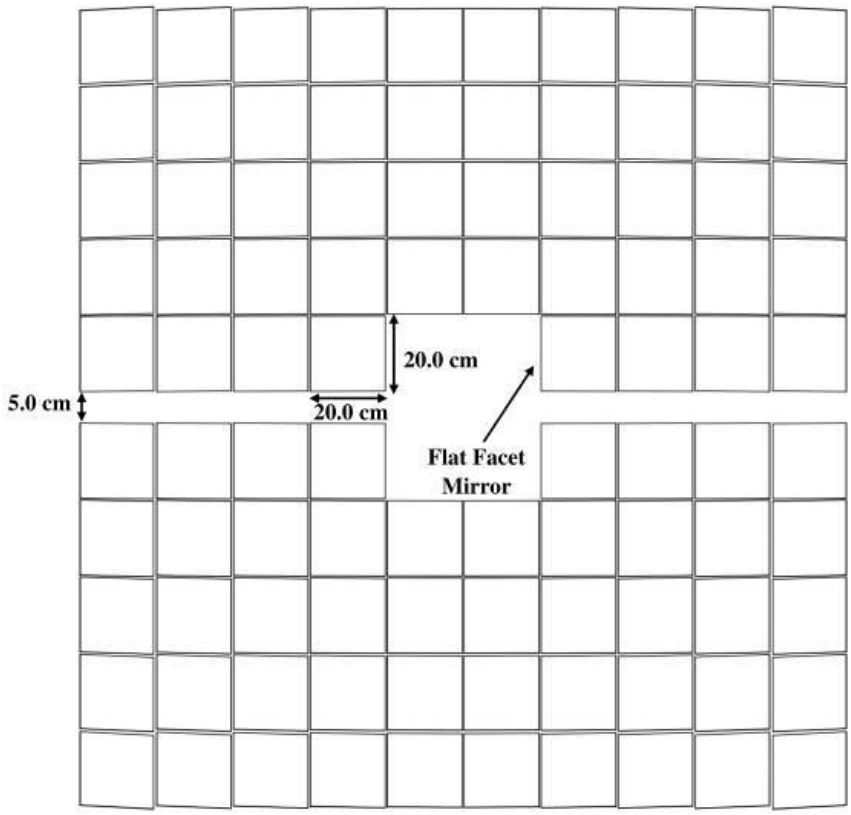

Figure 3.3: Schematic diagram shows the arrangements of 96 flat facet mirror sets with a dimension of 20 cm × 20 cm each that are arranged in ten rows and ten columns on the prototype in which four mirror sets at the central region of concentrator are omitted.

3.3.2 Automotive Radiator Cooling System

As sunlight is concentrated on the solar cell, the non-converted sunlight will generate heat that will raise the solar cell's temperature. If the temperature of the solar cell is higher than the standard operating temperature, the energy conversion efficiency will drop significantly. Therefore, an automotive radiator cooling system is applied in the prototype to obtain better heat dissipation effect and to maintain the temperature of solar cells at around 50 ℃ (Chong et al, 2012a). As shown in Figure 3.4, the automotive radiator cooling system comprises automotive radiator, water-cooling block, water pump, and reservoir.

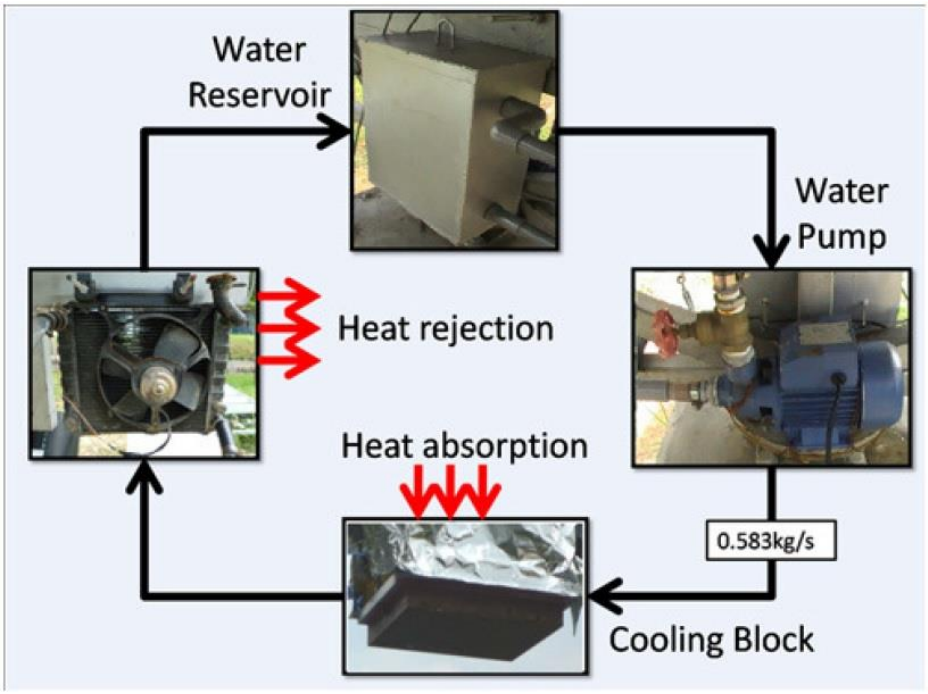

Figure 3.4: Automotive radiator cooling system (Chong et al., 2012a).

An automotive radiator has been used as the key device for the heat rejection in the cooling system. The materials of automotive radiator casing and tubes are aluminum alloy with high heat conductivity and light weight. It is easy to be installed into the prototype of NIDC with minimum load added to the driving system. The external fins sandwiched between the ducts in the radiator are made of copper in order to have higher heat conductivity for increasing heat dissipation rate. The total heat transfer area of radiator is reasonably large, which includes the surface areas of radiator ducts and of copper fins.

A copper water-cooling block is selected as a receiver to obtain better heat dissipation effect and to prevent the solar cell from operating at a high temperature. In this study, the preferred material of the cooling block is copper owing to its high thermal conductivity. A DC water pump is utilized for circulating water between the radiator and the cooling block. Its role is to create a constant water speed in whole automotive radiator cooling system at mass flow rate of 0.583 kg/s. Last but not least, the final component is a reservoir tank which acts as the start point and end point of the water circulation in the automotive radiator cooling system. It also provides additional space for storing back flow water when the system stops operation and to control the total volume of water in the whole cooling system at about 12 liters.

3.3.3 Sun-Tracking System

In order to maintain a high output power and stability of the DACPV system, a high-precision of the sun-tracking system is required to follow the sun's trajectory throughout the day. This prototype is designed to operate on the most common two-axis sun tracking system, which is azimuth-elevation sun-tracking system.

The drive mechanism for the solar concentrator consists of stepper motors and associated gears. Two stepper motors, with the specification of 0.05 degree in full step, are coupled to the elevation and azimuth shafts respectively for driving the concentrator to its desired position. Each stepper motor is coupled to its respective shaft via a worm gearbox with a gear ratio of 60:1, yielding an overall resolution of 8.33×10^{-4} °/step. Compared with ordinary gear trains using spur gears, the direction of worm gear transmission is irreversible because a larger friction involved between the worm and worm-wheel. In other words, worm gear configurations in which the gear cannot drive the worm are said to be *self-locking*. In this way, there is no motor energy consumption on stationary positions and the usage of complex load brake mechanisms is not required.

An open-loop control system is preferable for the prototype of solar concentrator so as to keep the design of the sun-tracking system simple and cost effective. Open-loop sensors, two 12-bit absolute optical encoders are attached to the shafts of the azimuth and elevation axes of the concentrator

respectively to monitor the turning angles and to send feedback signals to the controller if there is any abrupt change in the encoder reading. The sensors not only ensure that the instantaneous azimuth and elevation angles are matched with the calculated values from the controller but also eliminate any tracking errors due to the mechanical backlash, accumulated error, wind effects and other disturbances to the solar concentrator. With the optical encoders, any discrepancy between the calculated angles and real-time angles of solar concentrator can be detected, whereby the drive mechanism will be activated to move the solar concentrator to the correct position.

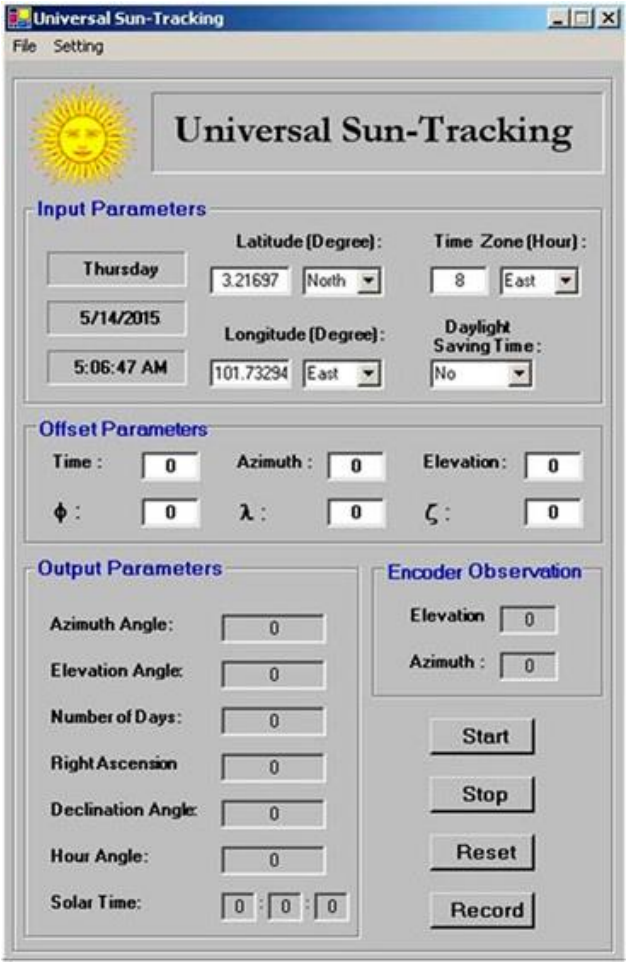

Figure 3.5: A Windows-based control program, Universal Sun-Tracking that has been integrated with the on-axis general formula.

A Windows-based control program was developed by integrating the general sun-tracking formula to control the sun-tracking mechanism along the azimuth and elevation axes (see Figure 3.5). The merit of the general sun-tracking formula is that it can simplify the fabrication and installation work of solar concentrator with higher tolerance in terms of the tracking axes alignment (Chong and Wong 2009; Chong et al., 2009a; Chong and Wong, 2010).

In the control algorithm, the sun-tracking angles (azimuth and elevation) are first computed according to the given information, i.e. local clock time, date, geographical location, time zone, daylight saving time and three misalign angles. The control program then generates digital pulses that are sent to the stepper motor driver via parallel port to drive the solar concentrator to the pre-calculated angles along azimuth and elevation movements in sequence. Each time, the control program only activates one of the two stepper motors through a relay switch. The tracker is programmed to follow the sun at all times since the program is run in repeated loops (every 1 minute). A feedback signal is sent when the difference between the calculated angles and encoders' reading is larger than the encoder resolution, which is 0.176°. Figure 3.6 shows the block diagram of the open-loop sun-tracking system implemented in this prototype.

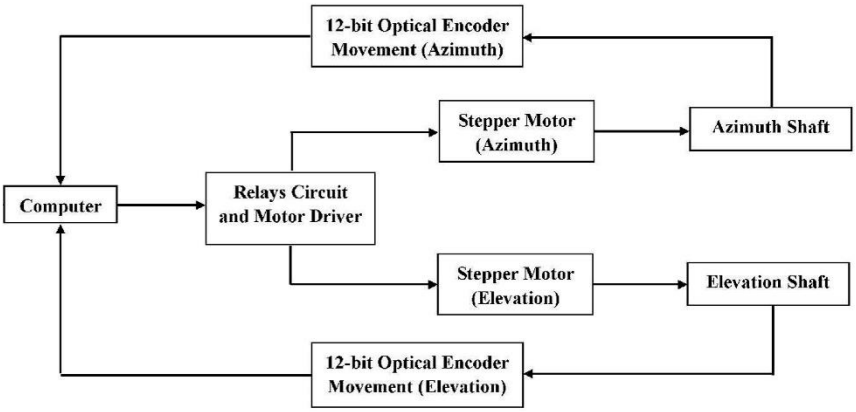

Figure 3.6: Block diagram to show the complete open-loop sun-tracking system of the NIDC.

3.4. Mirror Alignment

Based on the principle of NIDC, mirror alignment is essential to produce a uniform solar flux distribution through the superposition of all the reflected sunlight on the receiver. There are two stages in the mirror alignment process. The first stage is to fine tune the input parameters for the sun-tracking system so that the solar concentrator can track the sun accurately. The parameters that will affect the tracking accuracy are latitude, longitude, local clock time and the misalign angles. At this stage, four mirrors which are close to the center of the concentrator frame are selected to concentrate sunlight onto the target during the sun-tracking, whereas the remaining mirrors are covered. When the exposed mirrors achieve the smallest tracking error, a small offset value from the reflected sunlight to the expected target area, the second stage of mirror alignment can be started. The second stage is to tilt the remaining mirrors to focus sunlight towards the target. This mirror alignment

work must be carried out while the concentrator mirrors are in operation and tracking the sun.

3.5 Summary

A new configuration of solar concentrator, which is the non-imaging dish concentrator, has been designed and constructed. This prototype is capable of producing reasonably uniform solar flux distribution and high SCR for the application in DACPV system. Instead of using a single piece of parabolic dish, the NIDC consisting of 96 flat facet mirrors with a dimension of 20 cm $\times$ 20 cm act as the optical aperture. Each facet mirror has been tilted to collect and to reflect the incident sunlight onto the common receiver that is placed at a focal distance of 210 cm. Besides, the automotive radiator cooling system is applied in the prototype for the heat management purpose to lower down the temperature of solar cells. The prototype is orientated to face the direct sunlight by using the most common two-axis sun-tracking system, which is azimuth-elevation tracking system.

CHAPTER 4

OPTICAL CHARACTERIZATION OF NON-IMAGING DISH CONCENTRATOR

4.1 Introduction

The NIDC comprised of multi-faceted mirrors act as an optical aperture to collect and focus the incident sunlight at any focal distance along the optical axis. Different from imaging optical devices such as parabolic reflectors, the geometry of NIDC cannot be explicitly defined by any analytical surface formula, and thus, numerical simulation is a necessary means in optical analysis. For the optical modeling of the NIDC, the author has employed coordinate transformations and ray-tracing technique to express the reflection of sunlight by the dish concentrator as well as to generate the solar flux distribution on the receiver plane (Wong et al., 2015).

4.2 Optical Characterization

A numerical simulation using ray-tracing method has been developed for modeling the solar flux distribution profile on the receiver of NIDC prototype by assuming unity mirror reflectivity. In reflection-based solar concentrators, reflected rays could deviate from the specular reflection

direction and eventually not hitting on the receiver mainly caused by circumsolar radiation, mirror surface slope error and optical misalignment. This small angular deviation of sunray may bring a significant effect to the solar flux distribution at the receiver. As a result, the modeling of solar flux distribution is carried out by considering various imperfection factors, i.e. circumsolar ratio, mirror surface slope error and optical misalignment (Wong et al., 2015). The imperfection factors mentioned above are never discussed in the design and development of NIPC, which proposed by Chong et al. (2009b; 2010).

4.2.1 Tilted Angles of Flat Facet Mirrors

Referring to Figure 4.1, Cartesian coordinate system is applied for representing the main coordinate system (x, y, z) attached to the dish concentrator and the sub-coordinate system (x', y', z') attached to the i, j-facet mirror, where i and j refer to the mirror location at i-th row and j-th column of the dish concentrator respectively. The origins of the main coordinate system and sub-coordinate system are located at the center of the concentrator, $\boldsymbol{O}$ (0, 0, 0), and the center of i, j-facet mirror respectively. The coordinate of the central point of i, j-facet mirror is written as $\boldsymbol{H_{C\text{-}ij}} = (H_{Cx}, H_{Cy}, H_{Cz})_{ij}$. The incident angle ($\theta_{ij}$) of the sunray, relative to i, j-facet mirror, and the tilted angles of i, j-facet mirror about x'-axis (γ_{ij}) and y'-axis (σ_{ij}) can be derived as follows:

$$\theta_{ij} = \frac{1}{2}\arctan\left[\frac{\sqrt{H_{Cx}^2 + H_{Cy}^2}}{f - H_{Cz}}\right]_{ij} \tag{4.1}$$

$$\gamma_{ij} = \arctan\left[\frac{H_{Cx}}{\left(f - H_{Cz}\right) + \sqrt{H_{Cx}^2 + H_{Cy}^2 + \left(f - H_{Cz}\right)^2}}\right]_{ij} \tag{4.2}$$

$$\sigma_{ij} = \arctan\left[\frac{H_{Cx}}{\sqrt{\begin{pmatrix} H_{Cx}^2 + 2H_{Cy}^2 + 2\left(f - H_{Cz}\right)^2 \\ +2\left(f - H_{Cz}\right)\sqrt{H_{Cx}^2 + H_{Cy}^2 + \left(f - H_{Cz}\right)^2} \end{pmatrix}}}\right]_{ij} \tag{4.3}$$

where f is the focal length of the dish concentrator or the perpendicular distance of central points between the dish concentrator and the receiver.

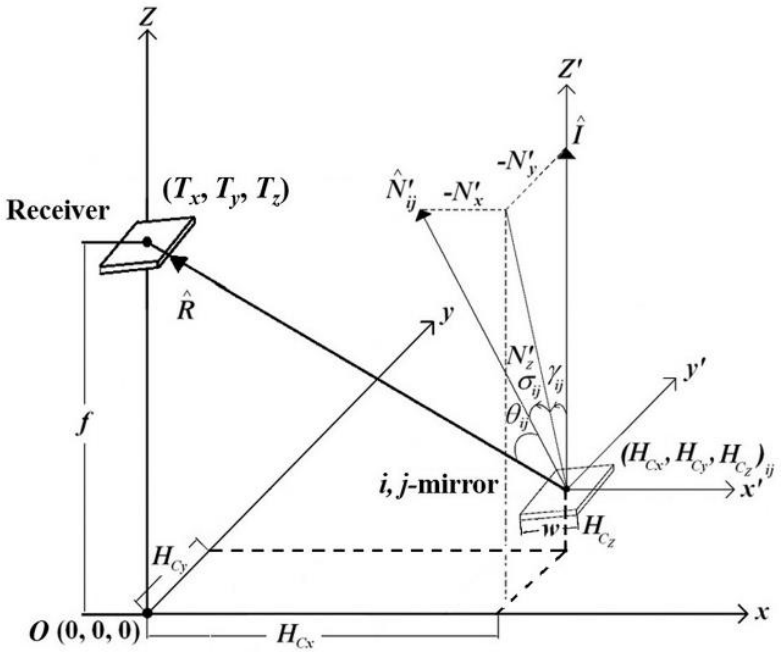

Figure 4.1: The Cartesian coordinate system used to represent the main coordinate system (x, y, z) attached to the plane of the dish concentrator and the sub-coordinate system (x', y', z') is defined attached to the i, j-facet mirror.

According to the principle of NIDC, all the flat facet mirrors need to be aligned precisely to produce a uniform solar flux distribution through the superposition of all the sunlight on the receiver. In fact, it is an arduous work to achieve perfect optical alignment in the flat facet mirrors of the concentrator. After the solar concentrator has been constructed, there are many factors to induce the optical misalignment of facet mirrors, which include manufacturing defect, imperfect optical alignment, and self-weight mechanical deflection. The induced optical misalignment makes the normal axis of the facet mirror deviated from its ideal orientation. The deviation of the normal axis of facet mirror can contribute to the distortion of the solar flux distribution. As shown in Figure 4.2, the optical misalignment angles of each facet mirror are introduced in the numerical modeling of the NIDC prototype in which the new tilted angles of *i*, *j*-facet mirror about *x*-axis (γ'_{ij}) and *y*-axis (σ'_{ij}) can be calculated by using the following expressions:

$$\gamma'_{ij} = \gamma_{ij} + \varepsilon r_{\gamma} \qquad -1 \le r_{\gamma} \le 1 \tag{4.4}$$

$$\sigma'_{ij} = \sigma_{ij} + \varepsilon r_{\sigma} \qquad -1 \le r_{\sigma} \le 1 \tag{4.5}$$

where r_{γ} and r_{σ} are the pseudorandom numbers, ε is the optical misalignment angle of the mirror, γ_{ij} and σ_{ij} are the tilted angles of *i*, *j*-facet mirror about x'-axis and y'-axis respectively without considering the optical misalignment.

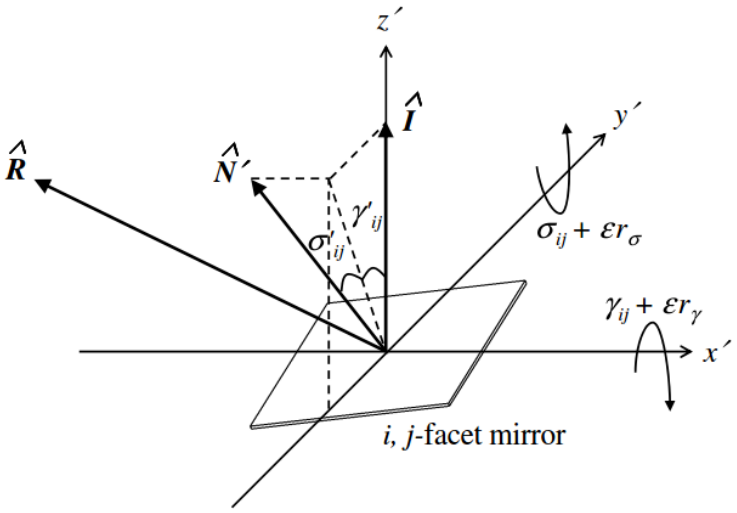

Figure 4.2: Two new tilted angles of *i*, *j*-facet mirror about *x*´-axis (γ'_{ij}) and *y*´-axis (σ'_{ij}) caused by optical misalignment.

4.2.2 Coordinate Transformation

An initial coordinate of the reflective point on the *i*, *j*-facet mirror is designated as $\boldsymbol{H_{ijkl}} = (H_x, H_y, H_z)_{ijkl}$, where *k* and *l* represent the position of the reflective point at the *k*-th row and *l*-th column of the facet mirror respectively. To ease the mathematical representation of coordinate transformations, we can make the translation a linear transformation by increasing the dimensionality of space. Thus, the coordinates $(H_x, H_y, H_z)_{ijkl}$ can also be represented by $(H_x, H_y, H_z, 1)_{ijkl}$, which is also treated as a vector in matrix form

$$[H]_{ijkl} = \begin{bmatrix} H_x \\ H_y \\ H_z \\ 1 \end{bmatrix}_{ijkl} \tag{4.6}$$

A new coordinate $\boldsymbol{H'_{ijkl}} = (H'_x, H'_y, H'_z)_{ijkl}$ is formed when each mirror has to be aligned with its corresponding tilted angles (γ'_{ij} and σ'_{ij}) for superposing all the incident sunlight at the common receiver. The final position of reflective point can also be written in a matrix form as

$$[H']_{ijkl} = \begin{bmatrix} H'_x \\ H'_y \\ H'_z \\ 1 \end{bmatrix}_{ijkl} \tag{4.7}$$

If the pivot point of the *i*, *j*-facet mirror $(H_{Cx}, H_{Cy}, H_{Cz})_{ij}$ is not located at the origin of the main coordinate system, the reflective point will be treated under translation transformation before rotation transformations. The initial coordinates of the reflective point will be first transformed from the main coordinate system that is attached to the concentrator frame to the sub-coordinate system that is attached to the local facet mirror via a translation transformation. The translation transformation matrix is

$$[T_1]_{ij} = \begin{bmatrix} 1 & 0 & 0 & -H_{Cx} \\ 0 & 1 & 0 & -H_{Cy} \\ 0 & 0 & 1 & -H_{Cz} \\ 0 & 0 & 0 & 1 \end{bmatrix}_{ij} \tag{4.8}$$

Then, it is followed by the first rotation transformation with the angle σ'_{ij} about the *y*-axis of the sub-coordinated system to transform the reflective point from the sub-coordinate system to a column movement coordinate system. The first rotation transformation matrix can be written as

$$\left[\sigma'_{ij}\right]=\begin{bmatrix}\cos\sigma'_{ij} & 0 & -\sin\sigma'_{ij} & 0\\ 0 & 1 & 0 & 0\\ \sin\sigma'_{ij} & 0 & \cos\sigma'_{ij} & 0\\ 0 & 0 & 0 & 1\end{bmatrix} \tag{4.9}$$

The following second rotation transformation with the angle γ'_{ij} about the *x*-axis of the column movement coordinate system transforms the reflective point from the column movement coordinate system to a row movement coordinate system. The second rotation transformation matrix can be written as

$$\left[\gamma'_{ij}\right]=\begin{bmatrix}1 & 0 & 0 & 0\\ 0 & \cos\gamma'_{ij} & -\sin\gamma'_{ij} & 0\\ 0 & \sin\gamma'_{ij} & \cos\gamma'_{ij} & 0\\ 0 & 0 & 0 & 1\end{bmatrix} \tag{4.10}$$

Finally, to transform the row movement coordinate system back to the main coordinate system, we need the last translation matrix that is written as

$$\left[T_2\right]_{ij}=\begin{bmatrix}1 & 0 & 0 & H_{Cx}\\ 0 & 1 & 0 & H_{Cy}\\ 0 & 0 & 1 & H_{Cz}\\ 0 & 0 & 0 & 1\end{bmatrix}_{ij} \tag{4.11}$$

As a result, the matrix for the coordinate transformations from the initial coordinate $\boldsymbol{H_{ijkl}} = (H_x, H_y, H_z)_{ijkl}$ to the final coordinate $\boldsymbol{H'_{ijkl}} = (H'_x, H'_y, H'_z)_{ijkl}$ can be shortly represented as

$$[H']_{ijkl} = [T_2]_{ij} [\gamma'_{ij}] [\sigma'_{ij}] [T_1]_{ij} [H]_{ijkl} \tag{4.12}$$

4.2.3 Mirror Surface Slope Error

In a real system, mirror surface slope error is unavoidable due to cost and technical restraints during the manufacturing process. Typically, this error is assumed random and is reported in standard deviation units. According to the literature (Johnston, 1995; Johnston et al., 1997; Pottler e al., 2005; Marz et al., 2011), it has been verified that the slope error of mirror surface in typical solar concentrators ranges from 2 to 4 mrad. In practice, the mirror surface is not perfect due to the slope error as depicted in Figure 4.3. The deviation from the perfect surface normal of the ideal mirror shape has caused distortion in the reflected sunlight. The imperfect surface normal of the mirror (Liu et al., 2006) can be determined by the following angles:

$$\theta_r = \sqrt{\left(-2\delta^2\right)\ln\left(1-r_\theta\right)} \qquad 0 \le r_\theta \le 1 \tag{4.13}$$

$$\varphi = 2\pi\, r_\varphi \qquad 0 \le r_\varphi \le 1 \tag{4.14}$$

where r_θ and r_φ are the random numbers, δ is the standard deviation of slope error.

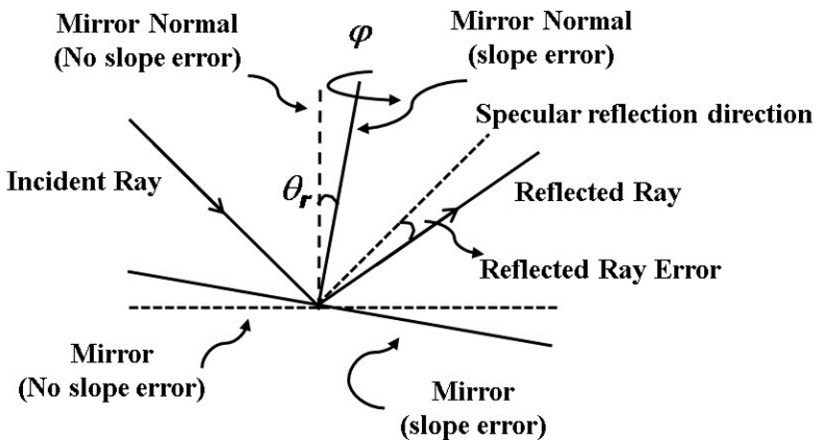

Figure 4.3: A mirror surface with slope error can cause the reflected ray deviated from the specular reflection direction.

Similar to the case of the reflective point, Eq. (4.15) shows that the new unit vector normal of the reflective point on the *i*, *j*-facet mirror (N'_x, N'_y, $N'_z)_{ijkl}$ can be obtained in the matrix form via the coordinate transformations and translations from its initial unit vector normal. Since all the facet mirrors are oriented in such a way that the normal of their surface are pointing toward +z-direction before they are tilted to direct the sunlight toward the receiver, the facet mirror's normal unit vector in the initial orientation can be described as $\hat{N}_{ijkl} = \hat{z}$.

$$[N']_{ijkl} = [\gamma'_{ij}][\sigma'_{ij}][\varphi]_{ijkl}[\theta_r]_{ijkl}[N]_{ijkl}$$

$$\begin{bmatrix} N'_x \\ N'_y \\ N'_z \\ 1 \end{bmatrix}_{ijkl} = \begin{bmatrix} 1 & 0 & 0 & 0 \\ 0 & \cos\gamma'_{ij} & -\sin\gamma'_{ij} & 0 \\ 0 & \sin\gamma'_{ij} & \cos\gamma'_{ij} & 0 \\ 0 & 0 & 0 & 1 \end{bmatrix} \times \begin{bmatrix} \cos\sigma'_{ij} & 0 & -\sin\sigma'_{ij} & 0 \\ 0 & 1 & 0 & 0 \\ \sin\sigma'_{ij} & 0 & \cos\sigma'_{ij} & 0 \\ 0 & 0 & 0 & 1 \end{bmatrix} \times \begin{bmatrix} \cos\varphi & -\sin\varphi & 0 & 0 \\ \sin\varphi & \cos\varphi & 0 & 0 \\ 0 & 0 & 1 & 0 \\ 0 & 0 & 0 & 1 \end{bmatrix}_{ijkl} \times \begin{bmatrix} 1 & 0 & 0 & 0 \\ 0 & \cos\theta_r & -\sin\theta_r & 0 \\ 0 & \sin\theta_r & \cos\theta_r & 0 \\ 0 & 0 & 0 & 1 \end{bmatrix}_{ijkl} \times \begin{bmatrix} 0 \\ 0 \\ 1 \\ 1 \end{bmatrix} \quad (4.15)$$

In the ray-tracing technique, the unit vector of the reflected ray from the mirror element has to be obtained first before determine its intersection point on the receiver plane. According to Snell-Descartes law, the unit vector of incident sunray $(I_x, I_y, I_z)_{ijkl}$ and the unit vector normal of the reflective point on the *i, j*-facet mirror $(N'_x, N'_y, N'_z)_{ijkl}$ are required to obtain the unit vector of principle reflected sunray. The unit vector of the principal reflected ray can be expressed as

$$\begin{bmatrix} R_x \\ R_y \\ R_z \end{bmatrix}_{ijkl} = \begin{bmatrix} 2\left(I_x N'_x + I_y N'_y + I_z N'_z\right)N'_x - I_x \\ 2\left(I_x N'_x + I_y N'_y + I_z N'_z\right)N'_y - I_y \\ 2\left(I_x N'_x + I_y N'_y + I_z N'_z\right)N'_z - I_z \end{bmatrix}_{ijkl} \quad (4.16)$$

where $I_x = 0$, $I_y = 0$, $I_z = 1$ by considering the incident ray exactly normal relative to the dish concentrator plane.

4.2.4 Circumsolar Radiation

In addition to mirror slope error, circumsolar radiation also contributes to the distortion of the flux distribution cast on the receiver. Buie et al. (2003a; 2003b) showed that the amount of energy in the circumsolar region is important because sun-shape plays an important role in determining the overall flux distribution and overestimated of output power may occur if all the power is assumed to fall within the extent of the solar disc only. The seriousness of circumsolar radiation effect is rated in term of the circumsolar ratio (CSR). Noring et al. (1991) demonstrated that the CSR values typically vary in the range from zero to 0.3. Circumsolar radiation is also considered in the optical analysis of the dish concentrator, where the solar rays that strike the mirror surface and the receiver are treated as cone rays.

In order to study the influence of circumsolar radiation to the solar flux distribution, for each principal reflected sunray, $\hat{R}_{ijkl}$, P sub-rays are generated within the solar cone, which subtends to the effective half angle of 43.6 mrad (Buie et al., 2003a; Buie et al., 2003b). Each sub-ray is denoted as $\hat{R}_m = R_{mx} 盒 R_{my} y + R_{mz} \hat{z}$, where m = 1, 2, 3,…P. By solving the line equation of the sub-ray and the surface equation of the receiver plane, the coordinate of the intersection point on the receiver can be calculated as

$$\begin{bmatrix} T_x \\ T_y \\ T_z \end{bmatrix} = \begin{bmatrix} \frac{R_{mx}}{R_{mz}}\left(f - H'_z\right) + H'_x \\ \frac{R_{my}}{R_{mz}}\left(f - H'_z\right) + H'_y \\ f \end{bmatrix} \tag{4.17}$$

The magnitude of sun-shape model implemented in the optical modeling (Buie et al., 2003a; Buie et al., 2003b) can be written as follows:

$$\phi(\theta_i) = \begin{cases} \dfrac{\cos(0.326\theta_i)}{\cos(0.308\theta_i)} & 0 \le \theta_i \le \theta_{sun} \\ e^{\kappa}\theta_i^{\gamma} & \theta_{sun} \le \theta_i \le 43.6 \end{cases} \tag{4.18}$$

where $\kappa = 0.9\ln(13.5\chi)\chi^{-0.3}$, $\gamma = 2.2\ln(0.52\chi)\chi^{-0.43} - 0.1$, χ is the CSR, θ_i is the radial displacement about the solar vector, θ_{sun} is the solar disc half angle of 4.65 mrad, i = 1, 2, 3, … P with P is the total number of sub-rays within the solar cone.

The pattern of solar flux distribution on the receiver plane can be plotted according to the computed intersection point (T_x, T_y). In order to achieve a smooth simulated result of illumination distribution at the receiver plane, each facet mirror of dimension 20 cm × 20 cm is sub-divided into 201 × 201 reflective points and the sub-rays within a cone has a resolution of 101 rays per aperture diameter. In addition, a matrix of 401 rows and 401 columns of pixels represent the receiver area of 40.0 cm × 40.0 cm and hence the modeled SCR, $C_{modeled}$ on each pixel can be calculated as

$$C_{\mathrm{mod}eled} = \sum_{n=1}^{N} \left(\frac{\text{area of reflective point (cm}^2\text{)}}{\text{area of receiver pixel (cm}^2\text{)}} \times \phi(\theta_i) \times \frac{\cos\theta}{\sum_{i=1}^{P} \phi(\theta_i)} \right) \tag{4.19}$$

where the area of a reflective point = $(20/201)^2$, the area of a receiver pixel = $(40/401)^2$, N is the total count of sub-rays hitting on the corresponding pixel on the receiver plane.

4.3 Results and Discussions

In this study, an optical characterization of the prototype of NIDC has been carried out using the aforementioned ray-tracing method by changing the values of optical misalignment angle (ε) in the range from 0 to 0.4°, circumsolar ratio (χ) in the range from 0 to 0.4, and, mirror surface slope error (δ) in the range from 0 to 4 mrad. Figure 4.4 shows the simulated results of solar flux distribution of NIDC in 2-D and 3-D mesh plots provided that all the parameters, i.e. ε, δ and χ, are null. By omitting the imperfection factors, the NIDC is capable of producing 338 cm^2 of uniform illumination area, which consists of a flat top area in the central region of flux distribution where the SCR is nearly constant, with a maximum SCR of 88 suns at the receiver.

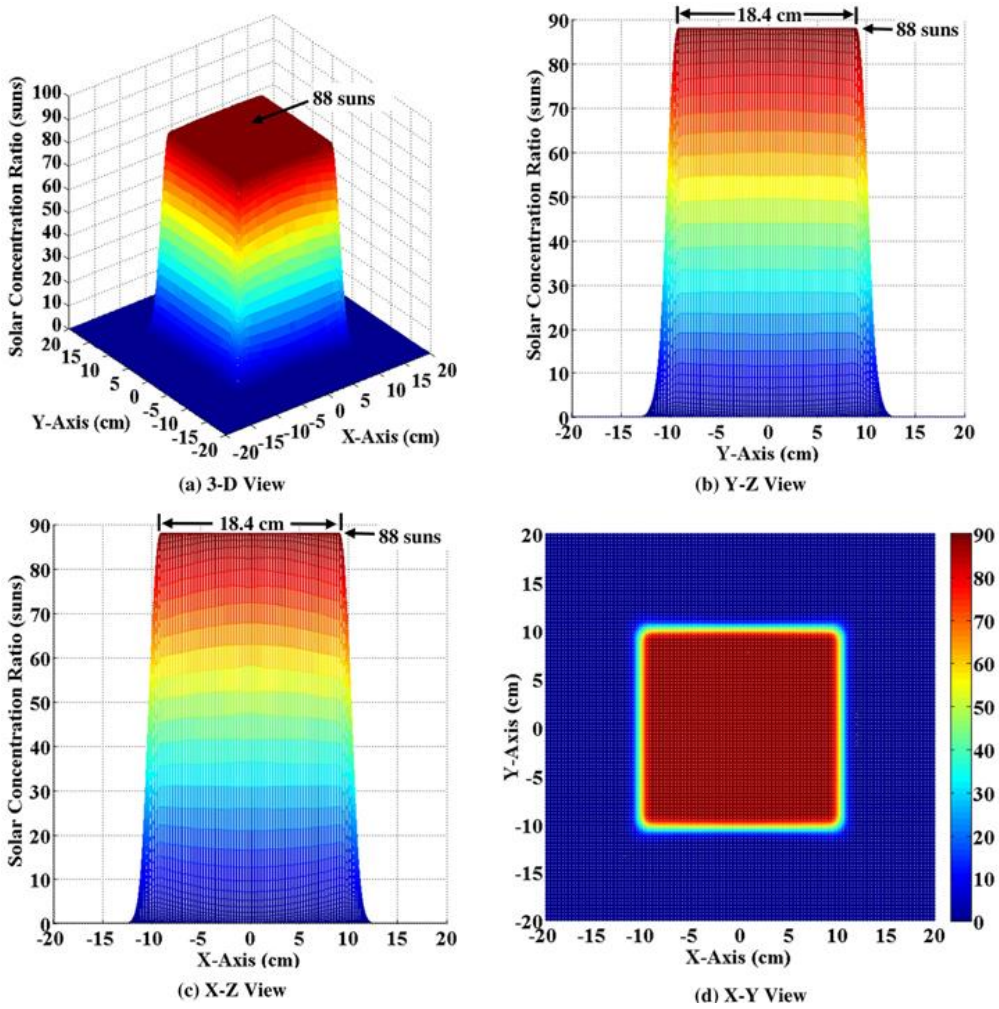

Figure 4.4: The simulated results of solar flux distribution of NIDC in 2-D and 3-D mesh plots by assuming $\varepsilon = 0°$, $\delta = 0$ mrad and $\chi = 0$.

By assuming perfect optical alignment, the solar flux distribution pattern with the highest SCR of 88 suns for different values of χ and δ are simulated and plotted as shown in Figure 4.5. From the simulated results, the uniform illumination area reduces as the values of χ and δ increase. By increasing the slope error, the uniform illumination region narrows while the base region of flux distribution broadens. This phenomenon is insignificant in the case of increasing the effect of circumsolar radiation as compared to that of slope error. To quantify the influence of circumsolar radiation and slope

error effects towards the quality of solar flux distribution at the receiver, optical characterization of the NIDC have been performed for different values of χ and δ, including uniformity of solar illumination, spillage loss, the optimization of receiver size and the optimization of DACPV module configuration.

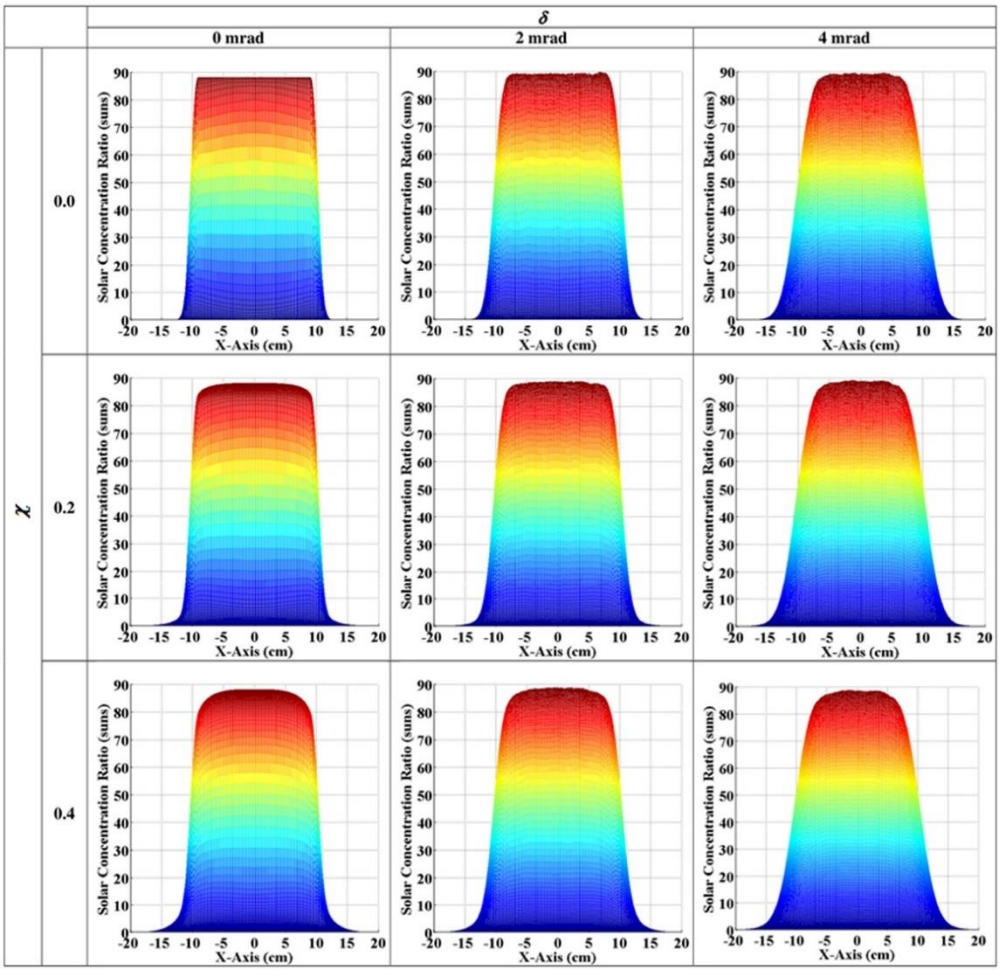

Figure 4.5: The simulated results show the influence of circumsolar ratio (χ) and slope error (δ) to the flux distribution of NIDC for 96 facet mirrors at a focal distance of 210cm. Assume that all flat facet mirrors are aligned precisely.

Spillage loss (or percentage of solar irradiance falling beyond the boundary of the receiver) and SCR at the edge of the receiver were simulated by adopting different sizes of square receiver. Figure 4.6 illustrates the spillage loss (with marker) and its corresponding lowest SCR at receiver edge (without marker) versus the receiver size (square in shape) from 10 cm to 30 cm for five different values of δ, i.e. 0 mrad, 1 mrad, 2 mrad, 3 mrad and 4 mrad, are plotted in the case of $\chi = 0$ and $\varepsilon = 0°$. According to the results, the increment of the slope error from 0 mrad to 4 mrad can cause the uniform illumination area decreasing from 338 cm^2 to 144 cm^2. The optimized receiver size to capture a reasonably uniform solar flux distribution with less than 5% variation of flux distribution (the difference between the highest and the lowest SCR within the receiver in percentage) and its corresponding spillage loss is summarized as the following. The optimized receiver size (spillage loss) for the cases of the slope error at 0 mrad, 1 mrad, 2 mrad, 3 mrad and 4 mrad are 18.8 cm (17.6 %), 18.4 cm (21.2 %), 17.2 cm (31.2 %), 15.8 cm (42.0 %) and 14.2 cm (53.2 %) respectively. The higher the slope error, the smaller the optimized receiver size will be.

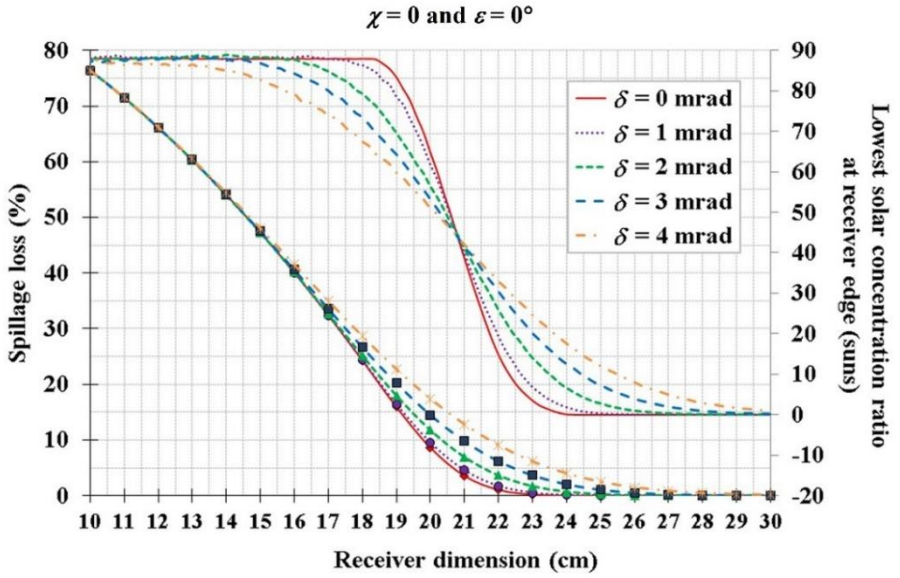

Figure 4.6: Spillage loss (with marker) and its corresponding lowest SCR at receiver edge versus receiver size (square in shape) for five different values of δ, i.e. 0 mrad, 1 mrad, 2 mrad, 3 mrad and 4 mrad, are plotted in the case of χ = 0 and ε = 0°.

Figure 4.7 shows the spillage loss (with marker) and its corresponding lowest SCR at receiver edge (without marker) versus the receiver size (square in shape) from 10 cm to 30 cm for five different values of χ, i.e. 0, 0.1, 0.2, 0.3 and 0.4, are plotted in the case of δ = 0 mrad and ε = 0°. For the case of without slope error and misalignment, the uniform illumination area decreases from 338 cm^2 to 154 cm^2 when the circumsolar ratio is increased from 0 to 0.4. Besides, the optimized receiver sizes (spillage loss) for the circumsolar ratios (χ) 0, 0.1, 0.2, 0.3 and 0.4 are 18.8 cm (17.6 %), 18.6 cm (19.9 %), 18.2 cm (23.7 %), 17.4 cm (30.4 %) and 16.2 cm (39.7 %) respectively. Therefore, the reduction of optimized receiver area for DACPV system is less significant as the circumsolar ratio increases up to 0.2.

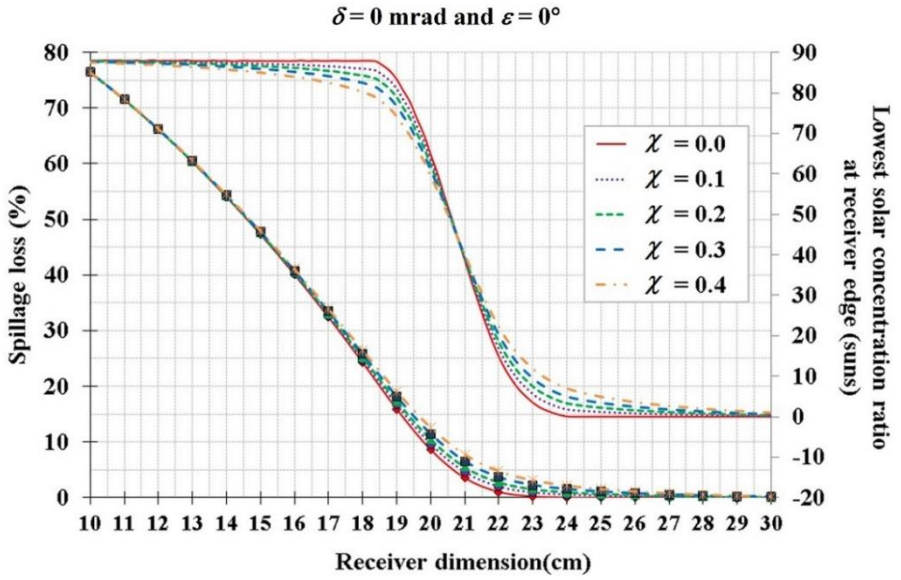

Figure 4.7: Spillage loss (with marker) and its corresponding lowest SCR at receiver edge versus receiver size (square in shape) for five different values of χ, i.e. 0, 0.1, 0.2, 0.3 and 0.4, are plotted in the case of δ = 0 mrad and ε = 0°.

According to the simulated results, the spillage loss for the optimized receiver size becomes very severe, as high as 58.7 %, if we increase slope error to 4 mrad and χ to 0.4 and hence the percentage of energy within uniform illumination area is less than 50%. Practically, it is not a wise idea to design the DACPV module that just only covers the uniform illumination area especially for the case of high spillage loss. Despite there is a current mismatch problem for the DACPV module working under non-uniform flux distribution, the electrical performance of the DACPV module can be optimized in such a manner that the appropriateness of serial and parallel interconnection among the solar cells can compensate the inhomogeneous illumination. In order to minimize the spillage loss and oversizing of the receiver, proper selection and detailed analysis of receiver size are very

important tasks. In this study, the receiver with a dimension of 25 cm × 25 cm is chosen. As shown in Figure 4.8, the receiver has a maximum spillage loss of 4.3 % for all the values of χ and δ when $\varepsilon = 0°$.

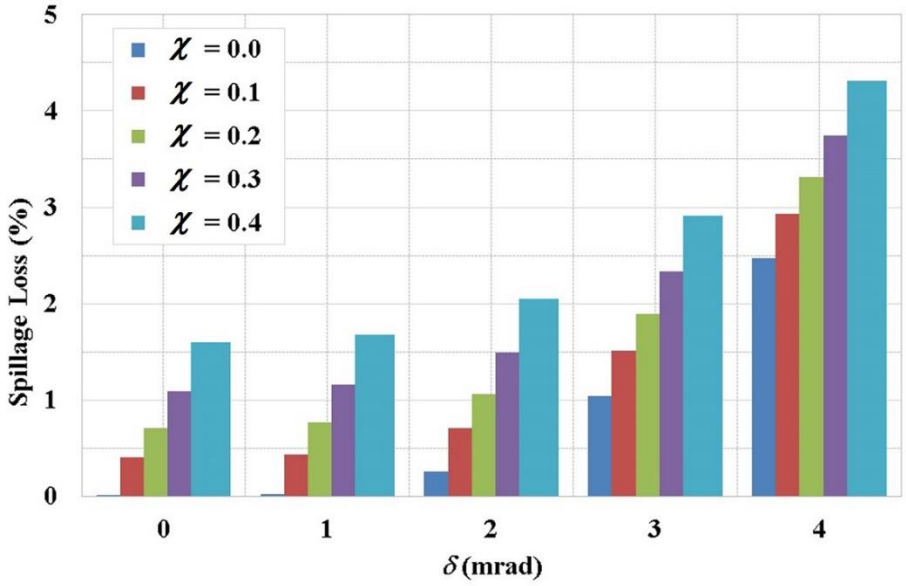

Figure 4.8: The spillage loss of receiver with a dimension of 25 cm × 25 cm all the values of χ and δ when $\varepsilon = 0°$.

In practice, optical alignment has been a general tough task for non-imaging multi-facet focusing concentrator to adjust all the facet mirrors precisely. To quantify the influence of optical misalignment towards the quality of solar flux distribution at the receiver, optical characterization of the NIDC have been performed for different values of optical misalignment angles (ε). Figure 4.9 illustrates the spillage loss (with marker) and its corresponding lowest SCR at receiver edge (without marker) versus the receiver size (square in shape) from 10 cm to 30 cm for five different values of ε i.e. 0°, 0.1°, 0.2°, 0.3° and 0.4°, are plotted in the case of $\chi = 0$ and $\delta = 0$ mrad.

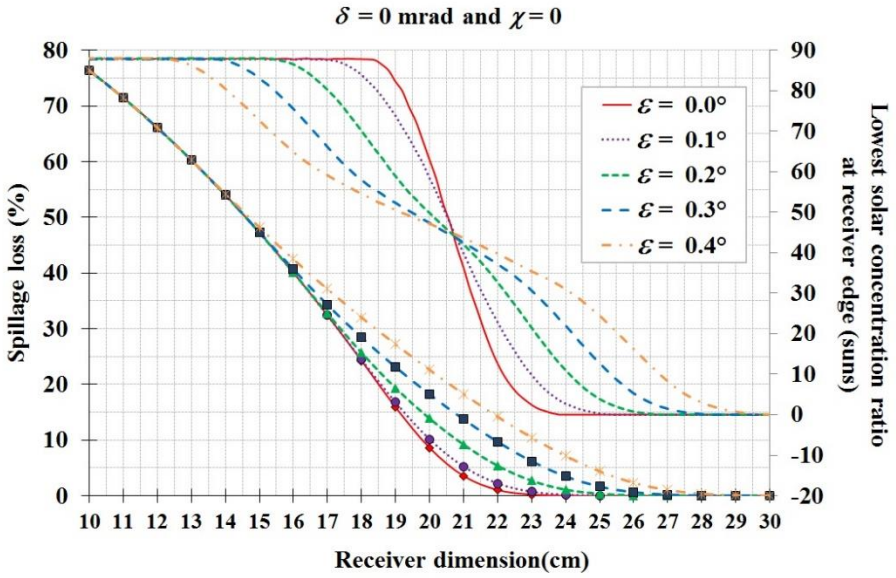

Figure 4.9: Spillage loss (with marker) and its corresponding lowest SCR at receiver edge versus receiver size (square in shape) for five different values of ε, i.e. 0°, 0.1°, 0.2°, 0.3° and 0.4°, are plotted in the case of χ = 0 and δ = 0 mrad.

The results show that the increment of the optical misalignment angle from 0° to 0.4° can cause the uniform illumination area decreasing from 338 cm^2 to 158 cm^2. Moreover, the optimized receiver sizes (spillage loss) for optical misalignment angles (ε) 0°, 0.1°, 0.2°, 0.3° and 0.4° are 18.8 cm (17.6 %), 18.0 cm (24.4 %), 16.6 cm (32.2 %), 15.2 cm (47.4 %) and 13.8 cm (54.3 %) respectively. According to the simulated results, the higher the optical misalignment, the smaller the optimized receiver size will be. For the receiver with a dimension of 25 cm × 25 cm, the spillage loss for optical misalignment angles (ε) 0°, 0.1°, 0.2°, 0.3° and 0.4° are 0%, 0%, 0.3%, 1.6% and 4.4% respectively (see Figure 4.9). The spillage loss for the receiver with a dimension of 25 cm × 25 cm is less significant as the optical misalignment

angles increase up to 0.2°. As a result, an accurate, inexpensive and fast approach is necessary to align the facet mirrors of the solar concentrator for minimizing the distortion of solar flux distribution.

4.4 Summary

A numerical simulation using ray-tracing method to model the solar flux distribution of NIDC prototype has been developed by considering three imperfection factors, i.e., circumsolar ratio, mirror slope error and optical misalignment. A comprehensive analysis on the simulation results has been carried out by considering all the important criteria to optimize the performance of DACPV system, such as the maximum SCR, uniform illumination area, and spillage loss. According to the simulated results, the three imperfection factors can cause serious deterioration to the uniform flux distribution area and the percentage of energy within the uniform illumination area. It is not a wise idea to design the DACPV module that just only covers the uniform illumination area. Therefore, the receiver size of a DACPV system can be optimized with the simulated flux distribution by minimizing the spillage loss. In this study, the receiver with a dimension of 25 cm × 25 cm is chosen to capture more than 95% of solar irradiance.

CHAPTER 5

INTERCONNECTION OPTIMIZATION FOR DENSE ARRAY CONCENTRATOR PHOTOVOLTAIC SYSTEM BY SIMULATION OF MATLAB/SIMULINK SOFTWARE

5.1 Introduction

Instead of using unconventional solar cells to overcome the inhomogeneous illumination, which incur extra cost and complexity, the author has proposed a systematic approach of optimizing the electrical interconnection of solar cells in DACPV module to achieve the maximum output power by considering the effects of both circumsolar radiation and mirror slope error (Wong et al., 2015). As a case study, the author applied this systematic approach to design an optimized DACPV module incorporated with the NIDC prototype as discussed in Chapter 3. The electrical interconnection of DACPV module can be optimized according to the simulated solar flux distribution of the dish concentrator as presented in Chapter 4 by minimizing the current mismatch caused by non-uniformity of concentrated sunlight.

5.2 Interconnection Optimization for DACPV Module

In the real operating conditions, the mirror surface slope error (δ) and circumsolar radiation (χ) are the key factors that distort the solar flux distribution on receiver, since the facet mirror misalignment (ε) can be eliminated by using an accurate optical alignment technique. Therefore, the interconnection of DACPV module is optimized according to the case of both χ and δ.

5.2.1 Dense Array Solar Cell

In this study, the Spectrolab CPV dense array solar cells (GaInP/GaInAs/Ge) with a dimension of 1.5 cm × 1.0 cm are used to assemble the DACPV module. According to the literature (King et al., 2010; Vossier et al., 2012), both short-circuit current, I_{SC} and open-circuit voltage, V_{OC} of the solar cells can be represented by the following equations:

$$I_{SC} = I^{1}_{SC} C \tag{5.1}$$

$$V_{OC} \cong V^{1}_{OC} + N \frac{kT_{cell}}{q} \ln C \tag{5.2}$$

where I^{1}_{SC} and V^{1}_{OC} are the short-circuit current and open-circuit voltage of the solar cell under one sun respectively, C is the SCR (suns), N is the

effective diode ideality factor, T_{cell} is the solar cell operating temperature (Kelvin), k is the Boltzmann constant and q is the electronic charge.

For this study, the solar cells are assumed to have zero value in series resistance, R_S = 0 Ω and effective diode ideality factor, N = 3. According to the Spectrolab CPV dense array solar cells datasheet, the one sun short-circuit current and open-circuit voltage under standard test condition are 20.9 mA and 2.76 V respectively (Spectrolab, 2010). Moreover, the solar cells are assumed operate at the standard temperature of 298 Kelvin and the irradiance level of 1000 W/m^2.

5.2.2 Electrical Interconnection

For optimizing the electrical interconnection of DACPV module to achieve maximum electrical power, the average SCR within the area that matches with the solar cell size has to be computed based on the simulated solar flux distribution as presented in Chapter 4. Figure 5.1 shows the dense array of solar cells with each of them mapped with the computed average SCR at its respective position on the receiver plane. The SCR was determined according to the numerical simulation result of solar flux distribution in the case of ε, χ and δ are zero. Increasing in both values of χ and δ can cause the SCR of solar cells located near the central region to be spread towards solar cells located near the peripheral region of the receiver.

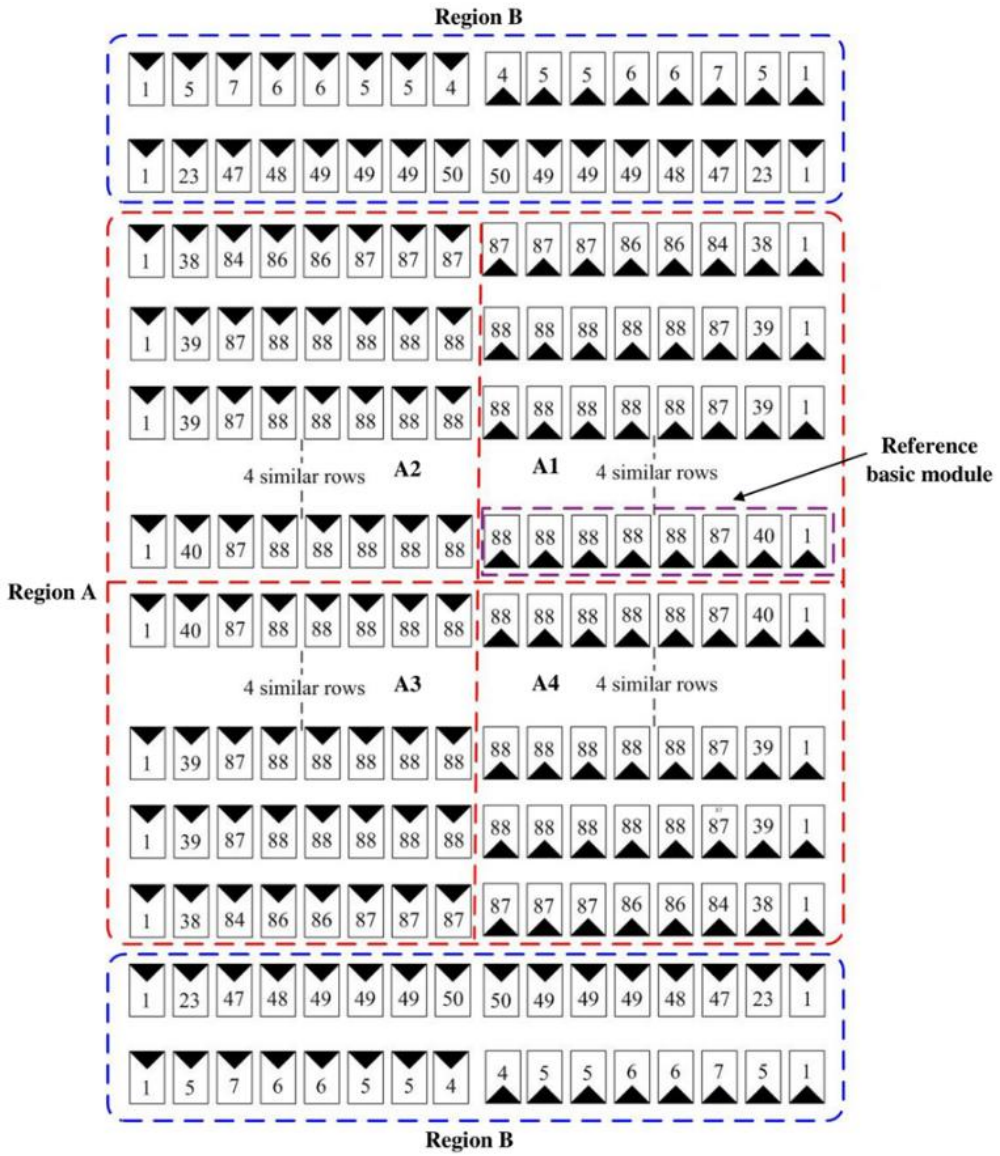

Figure 5.1: Based on the simulated solar flux distribution in the case of ε, χ and δ are zero, the average SCR of each solar cell was computed and mapped to its respective position on the receiver plane with a total dimension of 25.5 cm $\times$ 24.0 cm.

There is a total of 320 solar cells to be arranged into twenty rows and sixteen columns on the receiver plane with a dimension of 25.5 cm $\times$ 24.0 cm. The arrangement of the solar cells is organized in such a way that it keeps a gap spacing among the adjacent solar cells of 0.1 cm along the row direction

and 0.2 cm along the column direction. The gap is necessary for practical consideration in the assembling process of DACPV module, i.e. solder reflow process to attach the solar cells on the direct bond copper (DBC) substrate, and ribbon bonding process to connect the solar cells in serial or parallel interconnection. From Figure 5.1, the solar cells were grouped into two major regions: those rows of solar cells with higher SCR are assigned as region A (Region A is further divided into four symmetrical quadrants), and those rows of solar cells with the lower SCR are assigned as region B.

Referring to Figure 5.2, the flowchart illustrates the procedure of how to optimize the layout of solar cells interconnection circuit in the DACPV module. After mapping the solar concentrator ratio to each solar cell, both I_{SC} and V_{OC} of the solar cells are determined by using the Eqs. (5.1) and (5.2) respectively. In the region A, a basic module is defined as the maximum number of solar cells connected in parallel and located in the same row within the same quadrant. There are thirty-two basic modules that each of them connects eight solar cells in parallel are formed in the region A as shown in Figure 5.1. The connection from one basic module to another basic module is in series via ribbon bonding. The short-circuit current and open-circuit voltage of each basic module can be determined by adding the I_{SC} and averaging the V_{OC} of the solar cells that are connected in parallel in a basic module respectively. Both short-circuit current and open-circuit voltage of each basic module can be represented by the following equations:

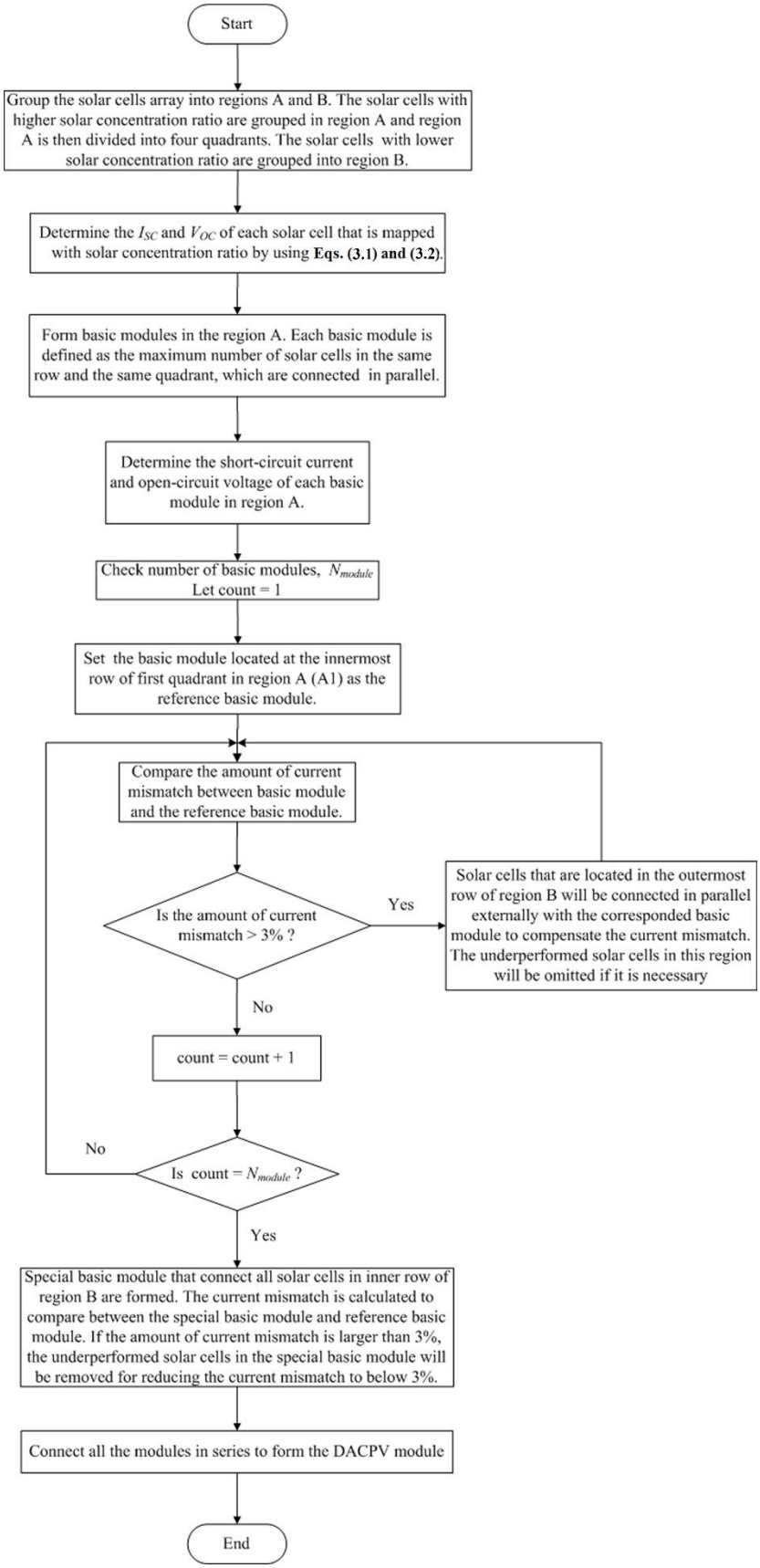

Figure 5.2: Flowchart shows the algorithm to optimize the electrical interconnection of dense array solar cells in DACPV module.

$$I_{\mathrm{SC-module}} = \sum_{1}^{n} I_{SC} \tag{5.3}$$

$$V_{\mathrm{OC-module}} = \frac{\sum_{1}^{n} V_{OC}}{n} \tag{5.4}$$

where I_{SC} and V_{OC} are the short-circuit current and open-circuit voltage of single solar cell accordingly, and n is the number of solar cells connected in parallel in a basic module.

The basic module located in the innermost row of the quadrant in the region A is set as the reference basic module. For example, reference basic module is selected in the region A1 as shown in Figure 5.1. The current mismatch is computed to compare the amount of output current between the other basic modules and the reference basic module. If the amount of current mismatch is larger than 3 %, the algorithm will select solar cells that are located in the outermost row of region B to connect in parallel externally with the corresponding basic modules for reducing the current mismatch to below 3%. Those solar cells in the outermost row of region B that is not utilized for compensating current mismatch will be removed at the end of the optimization process.

The subsequent row of solar cells after the outermost row in region B is defined as a special basic module in which all solar cells are connected in parallel. The current mismatch is also calculated to compare with the reference basic module. If the amount of current mismatch is larger than 3%, the

underperformed solar cells in the special basic module will be removed so that the current mismatch is well to below 3%.

5.2.3 Optimal Configurations of DACPV Module

As discussed in Chapter 4, the deterioration of solar flux distribution on receiver is insignificant in the case of increasing the circumsolar radiation (χ) as compared to that of mirror slope error (δ). Therefore, five different optimal configurations (the most optimized layout of solar cells interconnection circuits) of DACPV module are designed based on the simulated solar flux distribution with mirror slope error (δ) at 0, 1 mrad, 2 mrad, 3 mrad and 4 mrad respectively in the case of $\chi = 0$. Figure 5.3 to 5.7 show the schematic diagrams of the optimal configuration I, II, III, IV and V respectively, which are determined using the aforementioned optimizing algorithm as discussed in Figure 5.2.

For the optimal configuration I, the outermost row of solar cells in each region B are all omitted because the current mismatch of all basic modules in region A is minimum and thus compensation of current mismatch is not required (see Figure 5.3). For the special modules in this configuration, twelve solar cells are connected in parallel so that the current mismatch is less than 3% as compared to that of the reference basic module. There are eight solar cells in the inner row of each region B are omitted. The deterioration of solar flux distribution on receiver is significant when δ = 4 mrad. For that

reason, in the optimal configuration V, there are eight basic modules in region A being connected in parallel externally with all solar cells that are located in the outermost row of region B for reducing the current mismatch to below 3% as compared to that of the reference basic module (see Figure 5.7). In addition, fourteen solar cells located in the innermost row of each region B are connected in parallel externally to form the special modules in the optimal configuration V. There are two solar cells in the inner row of each region B are omitted.

By comparing the schematic diagrams shown in Figure 5.3 to 5.7, the number of solar cells used is increased for designing the optimized layout of solar cell interconnection circuits as the value of δ is increased. The deteriorated solar flux distribution on receiver requires more solar cells for compensating the current mismatch among the basic modules. As the value of δ is increased, the solar cells near to the peripheral region of the receiver will receive additional solar flux. At the same time, the flux density around the central region is reduced. Therefore, the number of solar cells in the basic module that near to the peripheral has to be increased in order to make up the current mismatch to be less than 3 %. The number of solar cells used in optimal configuration I, II, III, IV and V are 280, 288, 296, 308 and 316 respectively.

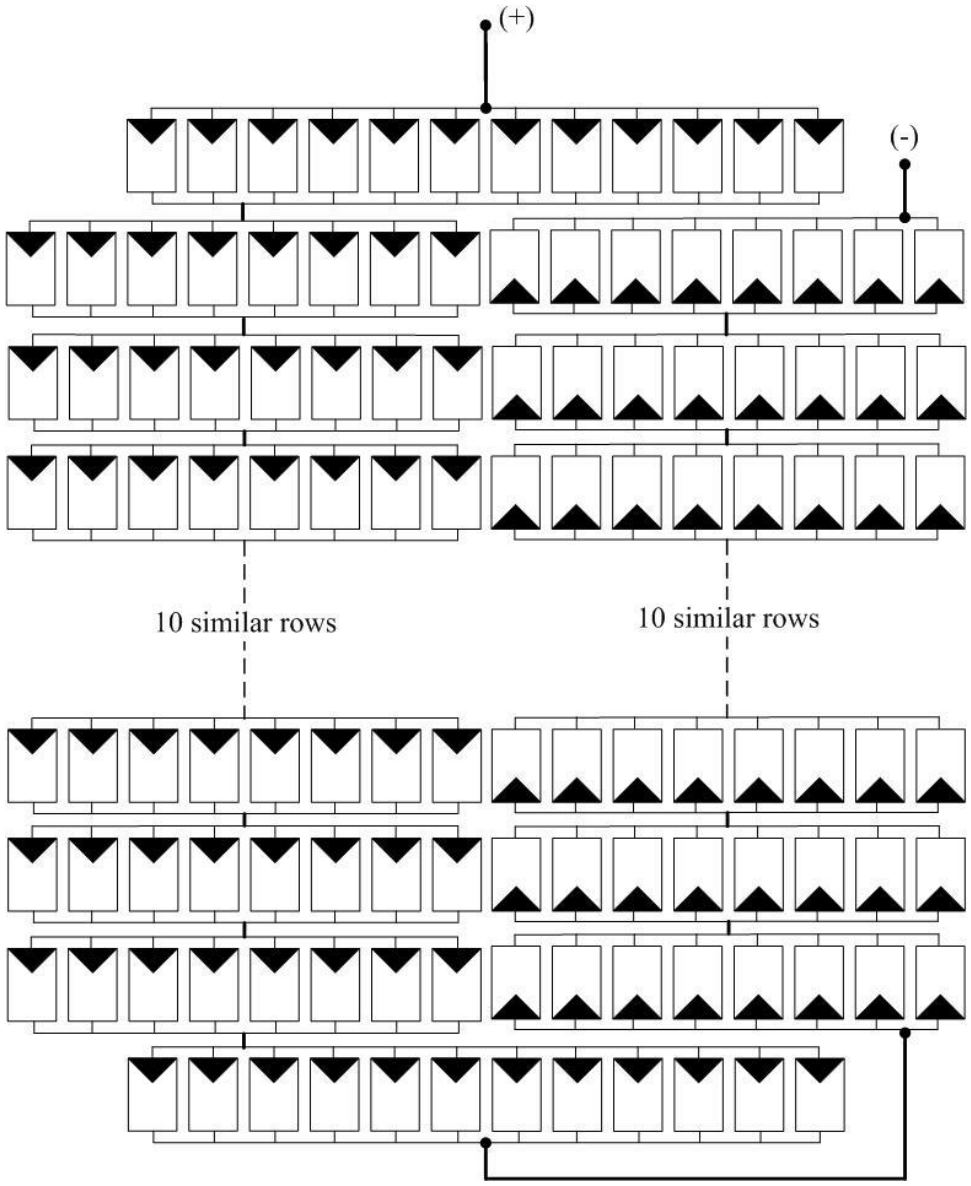

Figure 5.3: Schematic diagram to show optimal configuration I for the case of $\delta = 0$ mrad and $\chi = 0$.

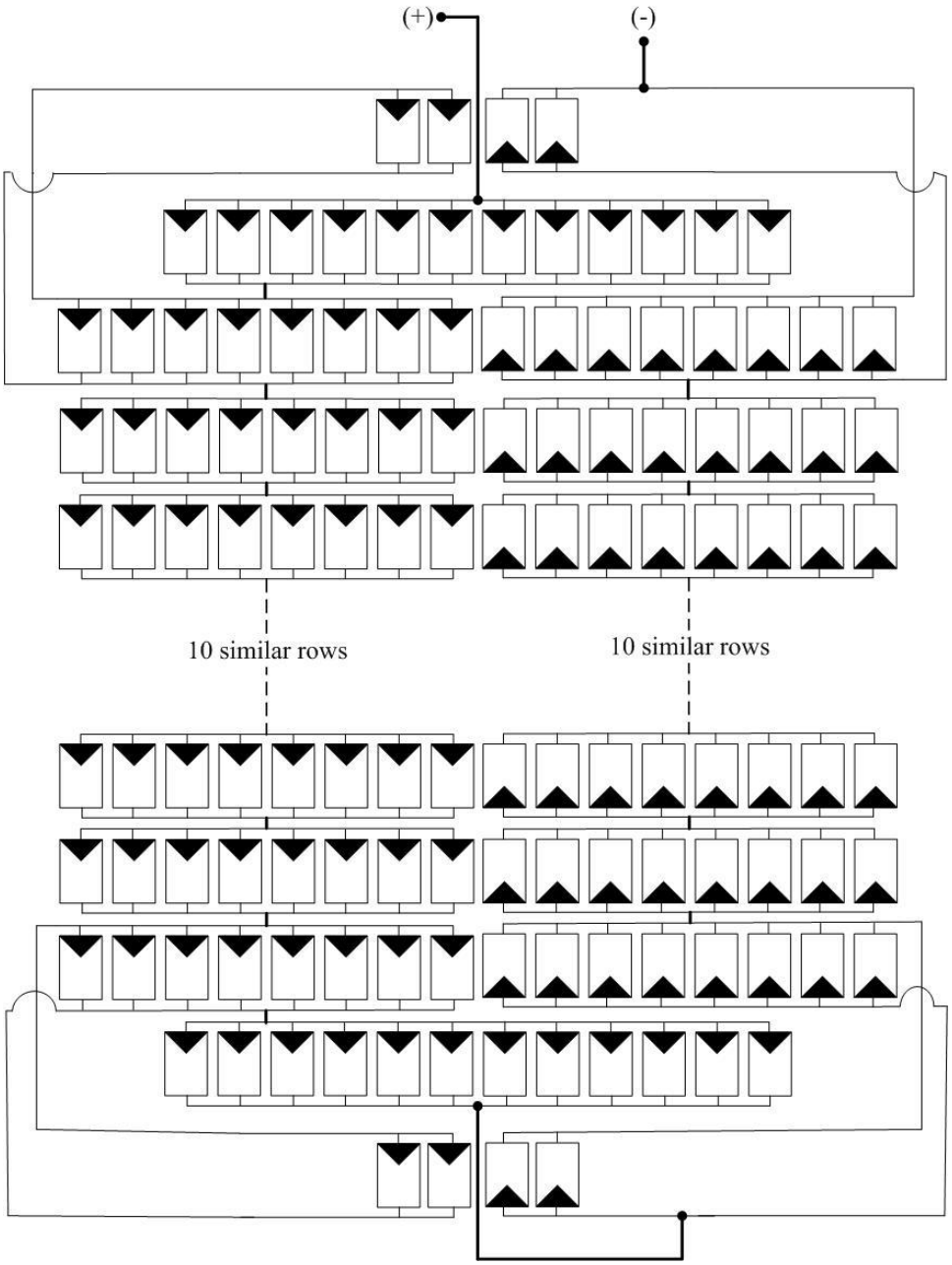

Figure 5.4: Schematic diagram to show optimal configuration II for the case of δ = 1 mrad and χ = 0.

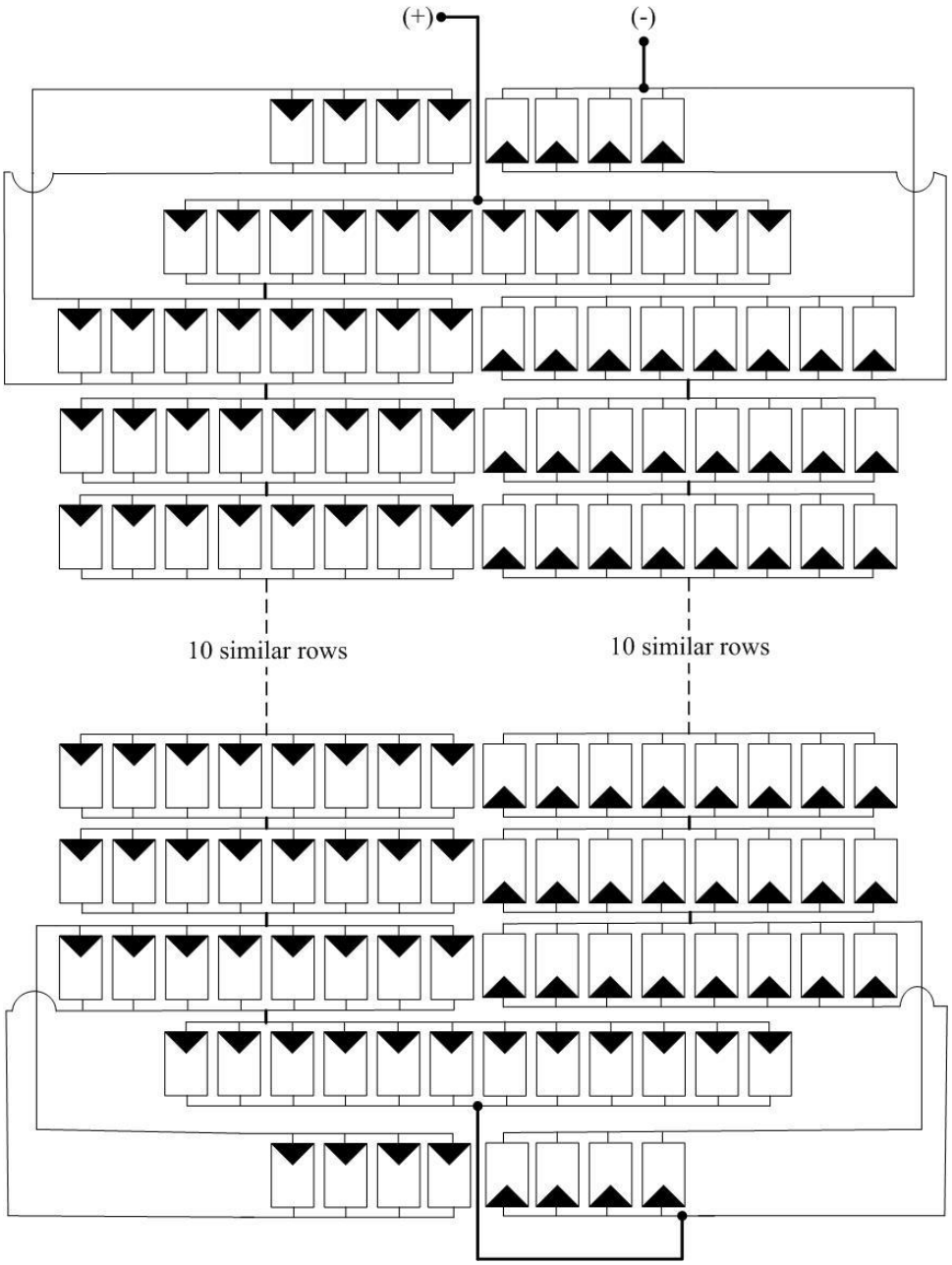

Figure 5.5: Schematic diagram to show optimal configuration III for the case of $\delta = 2$ mrad and $\chi = 0$.

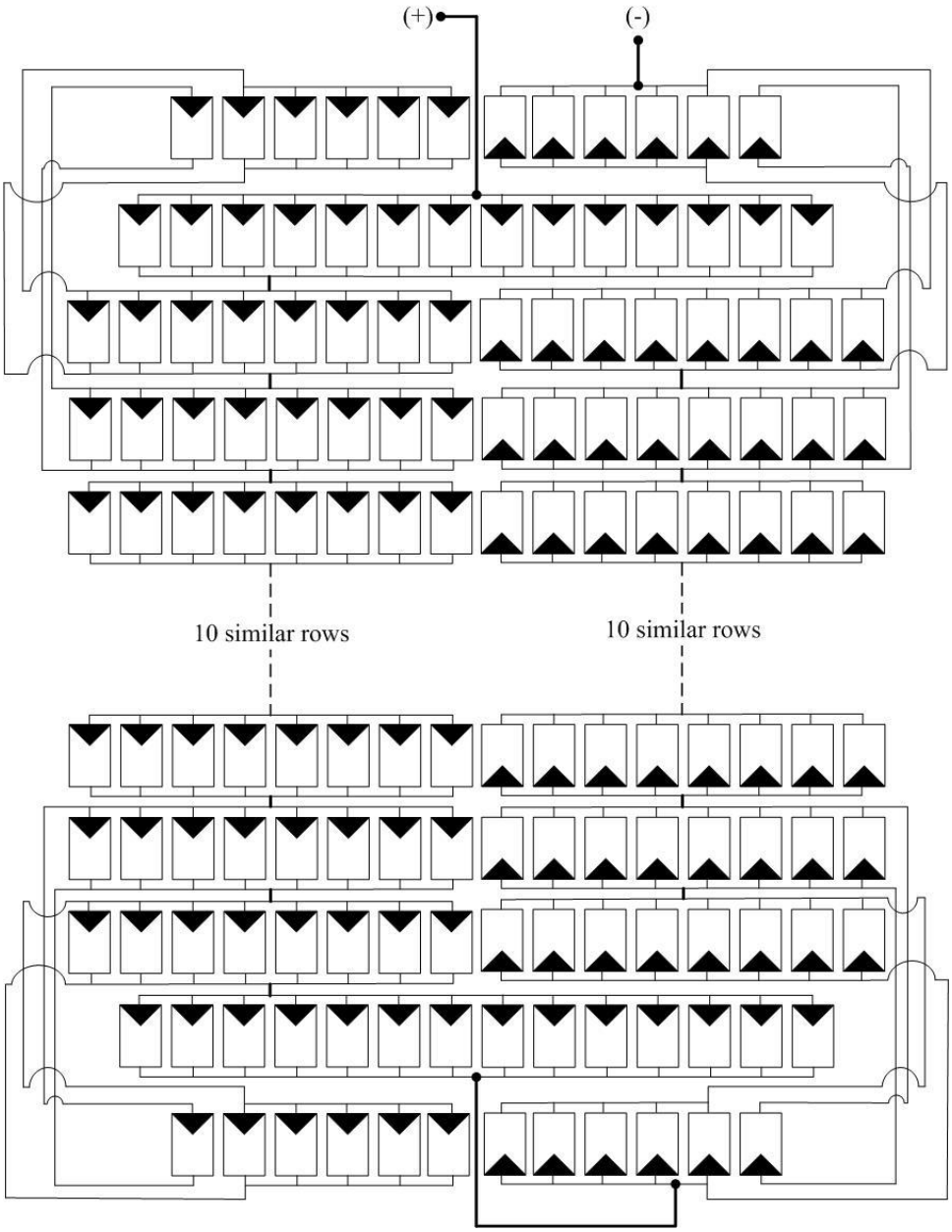

Figure 5.6: Schematic diagram to show optimal configuration IV for the case of δ = 3 mrad and χ = 0.

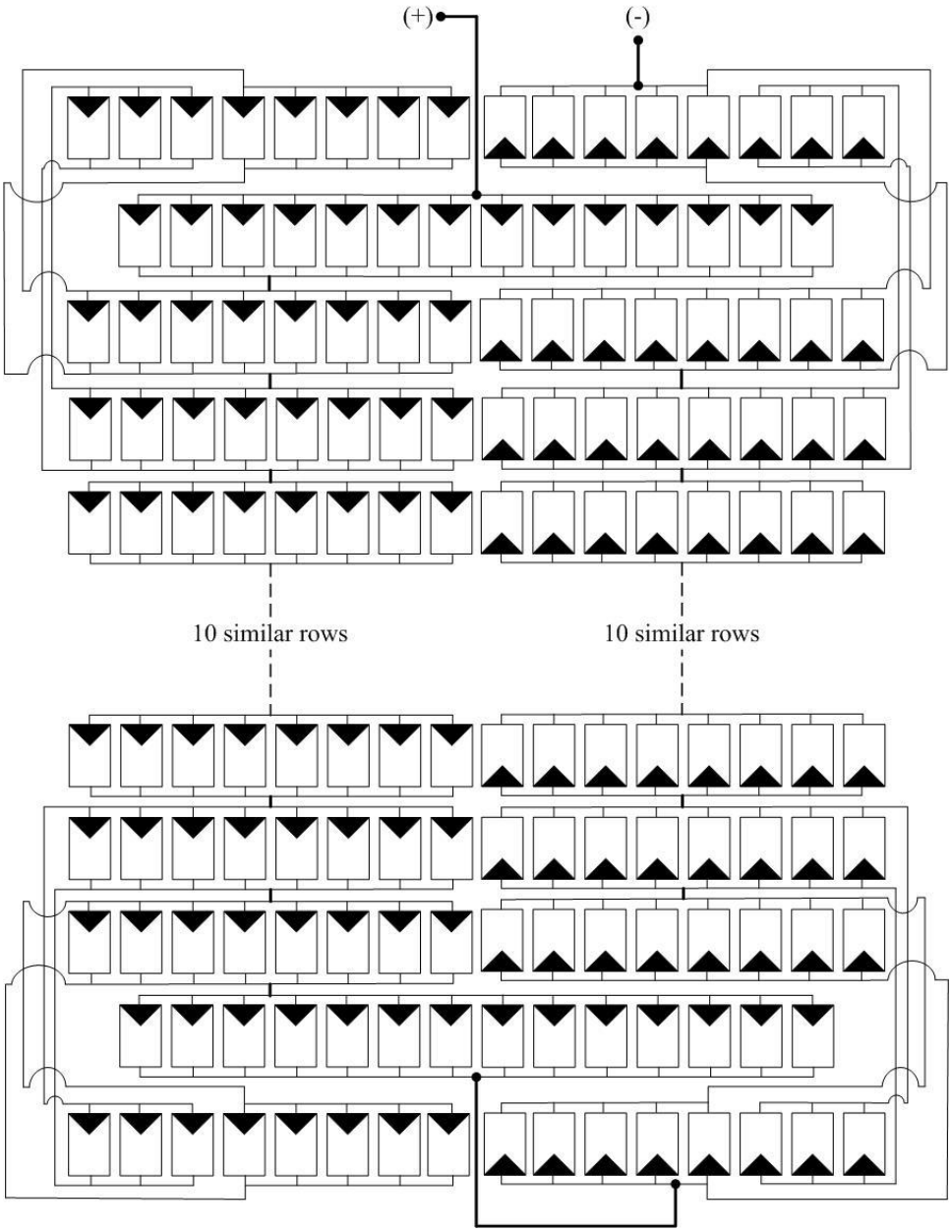

Figure 5.7: Schematic diagram to show optimal configuration V for the case of $\delta = 4$ mrad and $\chi = 0$.

5.3 Modeling and Simulation of DACPV Module

In this study, the author and his research teammates have presented MATLAB/Simulink-based modeling approach to accurately analyze the electrical performance of DACPV module (Chong and Siaw, 2012; Siaw and Chong, 2012; Siaw et al., 2014). A comprehensive equivalent circuit model for a triple-junction solar cell can be represented by three current sources connected in series. Nonetheless, not all of the parameters that are required by the model can be readily collected from field measurements nor obtained from a standard manufacturer's datasheet. Therefore the two-diode model, a model that is capable of representing triple-junction cells, is chosen for this study (see Figure 5.8).

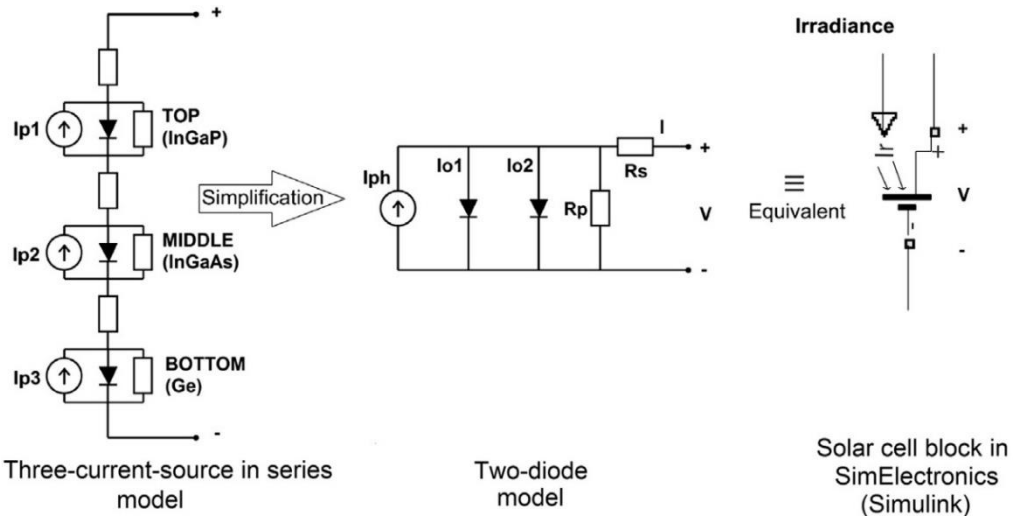

Figure 5.8: A schematic diagram to show the representation of a triple-junction solar cell which is simplified from three-current-source in the series model to the two-diode model, which is equivalent to a solar cell block in SimElectronics.

Solar cell block represented by a single solar cell as a current source with two exponential diodes, a parallel resistor (R_P), and connected in series with a series resistance (R_S) are arranged into subsystems in Simulink to form an array. The output current, I, can be represented by the equation

$$I = I_{ph} - I_{o1} \times \left(e^{(V+IR_S)/(N_1 V_t)} - 1 \right) - I_{o2} \times \left(e^{(V+IR_S)/(N_2 V_t)} - 1 \right) - \left(V + IR_S \right) / R_P \quad (5.5)$$

where I_{ph} is the solar-induced current, I_{o1} is the saturation current of the first diode, I_{o2} is the saturation current of the second diode, V_t is the thermal voltage, N_1 is the diode ideality factor of the first diode, N_2 is the diode ideality factor of the second diode, and V is the voltage across the solar cell.

In Simulink, it is possible to choose either an eight-parameter model in which the preceding equation describes the output current or a five-parameter model. In the five-parameter model, two simplifying assumptions are made: the first assumption is that saturation current of the second diode is zero in value and the second assumption is that the impedance of its parallel resistor is infinite. The five-parameter model is good enough to perform a reasonably accurate analysis, and Siaw et al. (2014) have successfully verified it in the field test that will be presented in the later section.

For this study, the five-parameter model is applied to solar cell blocks from SimElectronics, which are the component libraries for modeling and simulating electronic and mechatronic systems in Simulink. Therefore, solar cells are parameterized in terms of short-circuit current (I_{SC}) and open-circuit

voltage (V_{OC}). Both short-circuit current and open-circuit voltage values are common parameters which are readily available in a manufacturer's datasheet or measured as field data. To complete the modeling of the entire array, parameters such as short-circuit current (I_{SC}), open-circuit voltage (V_{OC}), diode ideality factor (N), the series resistance (R_S) and irradiance level of each solar cell are keyed-in to the program.

To protect CPV cells from the reverse-bias breakdown that could cause permanent damage to the cells, every solar cell must be connected in parallel with bypass diode in opposite polarity. When the cell is shaded or receives lower solar irradiance, the bypass diode is forward biased so that the current of the array can safely pass through the combination of cell-bypass-diode. For an array exposed to non-uniform solar irradiance, the role of bypass diode is very vital to avoid those CPV cells receiving low irradiance become the load of other CPV cells receiving high irradiance. The bypass diode creates an alternative path for the current so that the underperforming CPV cell is protected. When the array current passes through the bypass diode, the diode will turn on and hold the corresponding cell or group of cells to only a small negative voltage which can help to limit any further drop in the total voltage of the whole array (Karatepe et al., 2007).

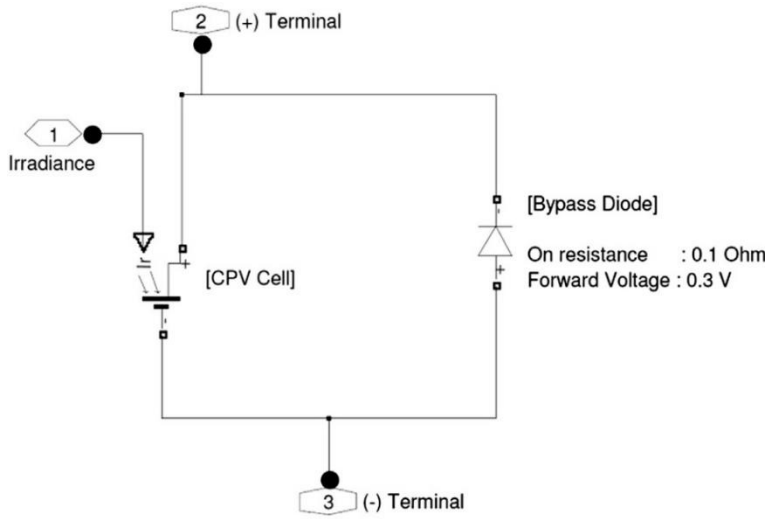

Figure 5.9: The first stage modeling is a sub-system consisting of a CPV cell and bypass diode.

In the modeling of DACPV module, the combination of solar cell and bypass diode is referred as the first stage of modeling, and it acts as the lowest layer of a sub-system for ease of array connection as revealed in Figure 5.9. For second stage modeling, the full connection consists of several number of sub-systems that are connected in series and parallel interconnection to represent a complete DACPV module (see Figure 5.10).

The manner of computing both *I-V* and *P-V* curves is summarized in block diagram for computational modeling under Simulink environment, which is known as the last stage implementation. The last stage of the dense array solar cells modeling is depicted in Figure 5.11 while all other stages are masked as sub-systems under “DACPV array” block.

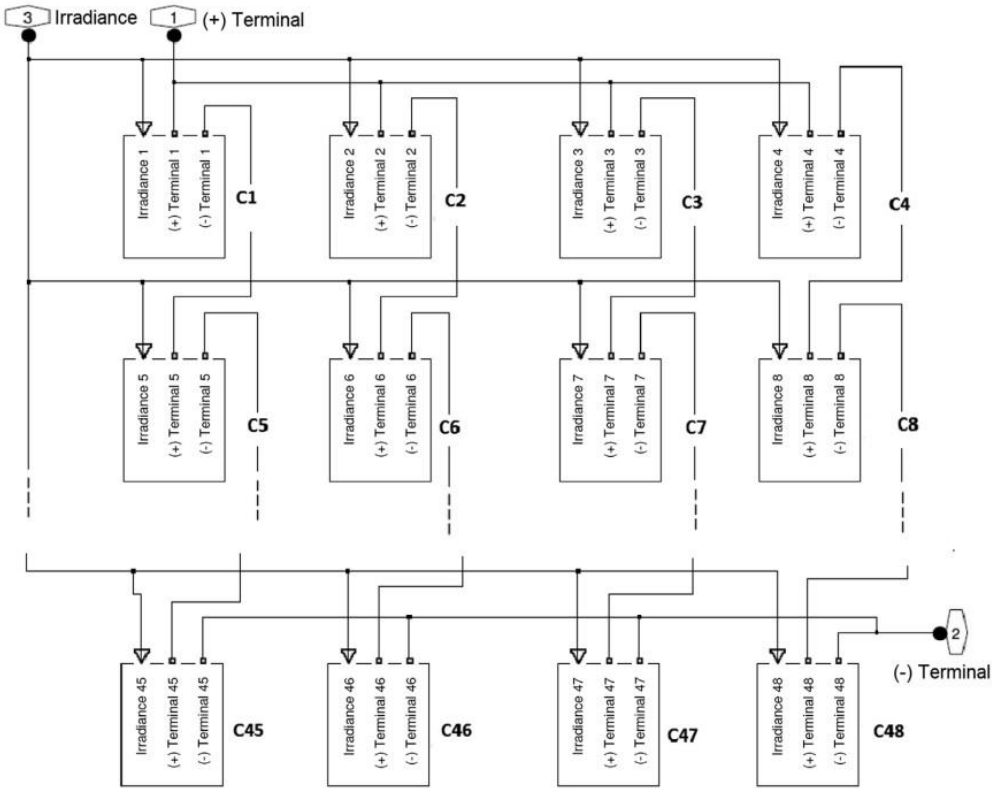

Figure 5.10: The second stage modeling is a Simulink sub-system assembly. In this example, 12 × 4 solar cells are connected using Series-Parallel configuration to form a DACPV module (Siaw et al., 2014).

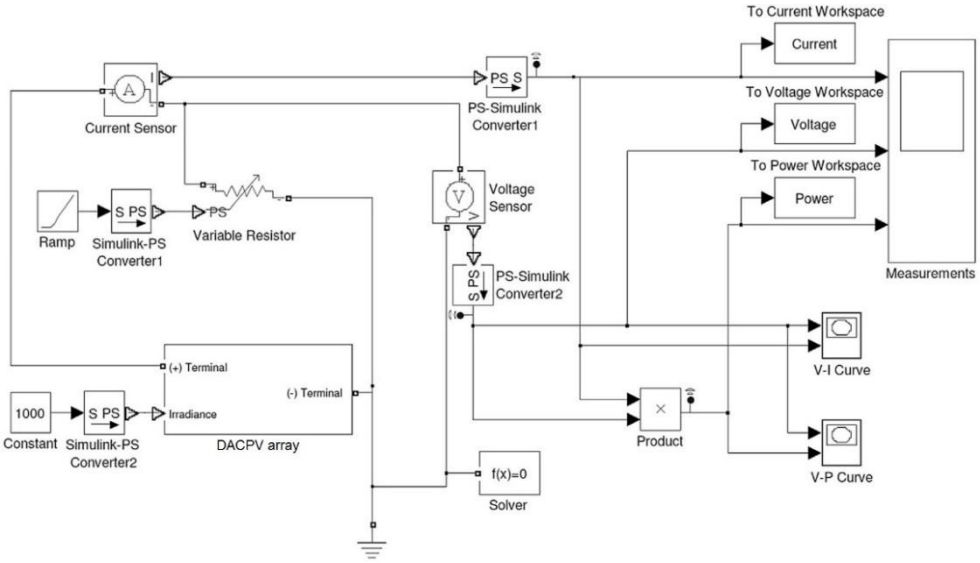

Figure 5.11: Overall Simulink implementation of DACPV module simulation with block diagram.

Upon completing the above steps, this model is ready for simulation with a selected simulation time that will affect the resolution of *I-V* and *P-V* curve. Results generated from simulation, such as the current, voltage and output power values are stored in MATLAB workspace and can be exported to excel for further analysis. The flow chart to illustrate the procedure of dense array solar cells modeling is shown in Figure 5.12.

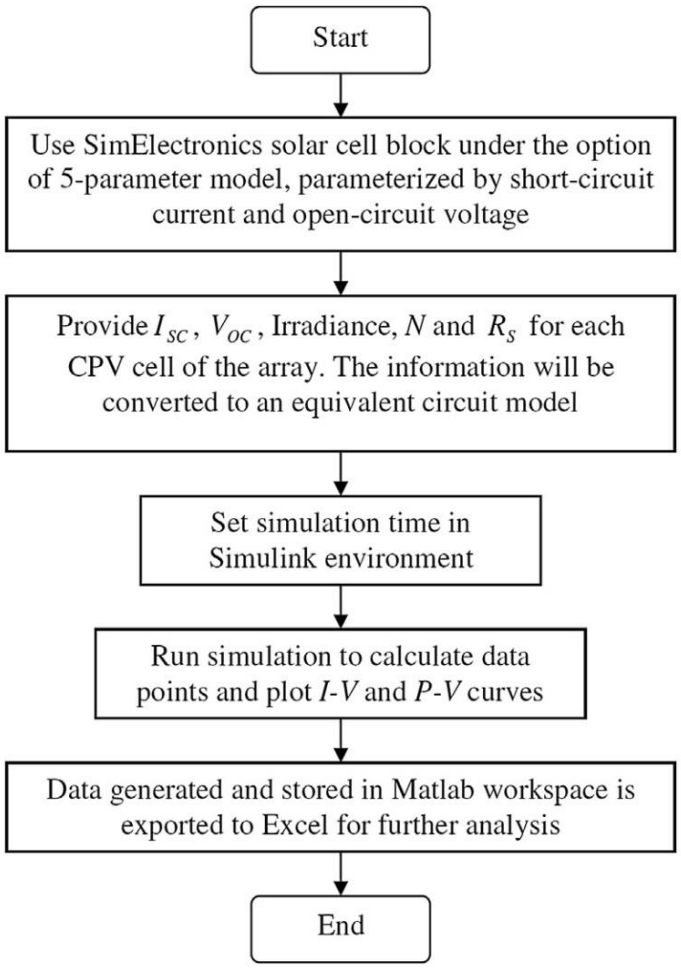

Figure 5.12: A flow chart shows the DACPV module modeling and simulation approach using Simulink.

5.4 Results and Discussions

After the optimization process, the five optimal configurations (i.e. optimal configuration I, II, III, IV and V) of DACPV module have been simulated in Simulink platform to obtain the maximum output power for the typical values of χ ranging from 0 to 0.4 and, δ ranging from 0 to 4 mrad. In this simulation, each basic module is modeled to be connected in parallel with bypass diode in opposite polarity to protect solar cells from the reverse-bias breakdown that could cause permanent damage to the cells. When a current mismatch occurs in a basic module, bypass diode will be forward biased so that the current of the array can safely pass through.

Figure 5.13 shows the *I-V* and *P-V* curves, which are simulated by using MATLAB/SIMULNK software, for the optimal configuration I of DACPV module for the case of zero values in χ and δ. The maximum electrical output power of the DACPV module can be extracted from the *P-V* curve. Both *I-V* and *P-V* curves are also plotted for different values of χ (i.e. 0, 0.1, 0.2, 0.3 and 0.4) and δ (i.e. 0 mrad, 1 mrad, 2 mrad, 3 mrad and 4 mrad). The maximum electrical output power for different values of χ and δ are extracted respectively from the aforementioned simulated *P-V* curves. According to the results, the five optimal configurations are capable of producing maximum output power of 1.1 kW for the ideal case of zero values in χ and δ. The electrical power losses of the five optimal configurations have been analyzed for different values of χ and δ. The electrical power losses can be calculated with the equation

$$\text{Power loss} = \frac{P_{\text{elec}}}{P_{\text{elec}-\max}} \times 100\ \% \tag{5.6}$$

where P_{elec} is the maximum output power for different values of χ and δ, and $P_{\text{elec-max}}$ is the maximum output power of 1.1 kW for the ideal case of zero values in χ and δ.

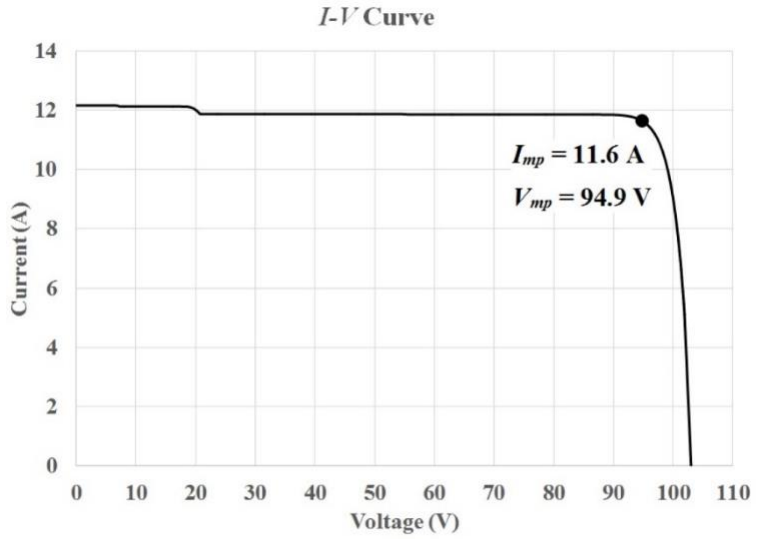

(a)

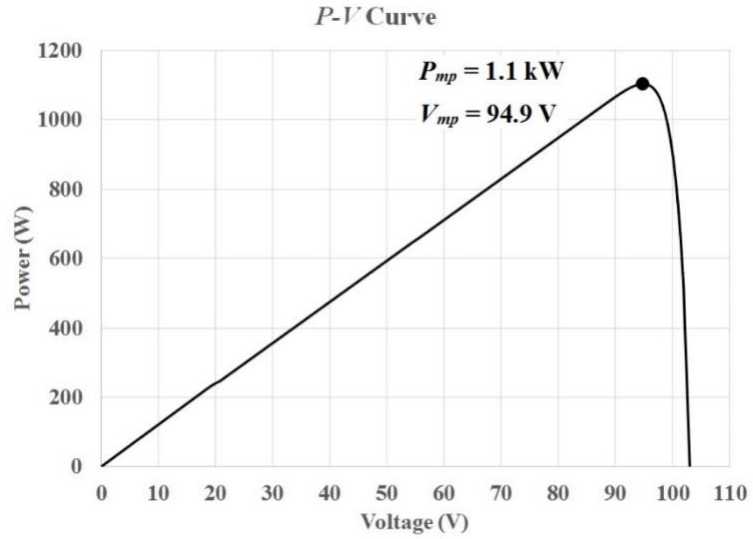

(b)

Figure 5.13: (a) *I-V* curve; (b) *P-V* curve for the optimal configuration I of DACPV module for the case of zero values in χ and δ.

The electrical power losses of the optimal configuration I, II, III, IV and V for the values of χ, ranging from 0 to 0.4 and δ, ranging from 0 to 4 mrad are shown in Figure 5.14 to 5.18, respectively. By comparing the results shown in Figure 5.14 to 5.18, the optimal configuration I has the highest electrical power losses and the optimal configuration V has the lowest electrical power losses for all values of χ and δ as compared to the others configurations. This indicates that a significant performance drop will happen to the configuration of DACPV that is designed without considering the effect of slope error. The higher the slope error, the higher the power loss will be in the optimal configuration I. In addition, when χ increases from 0 to 0.4, the increment of electrical power losses of optimal configuration IV and V are less significant for the case of δ, ranging from 0 to 2 mrad as compared with others configurations.

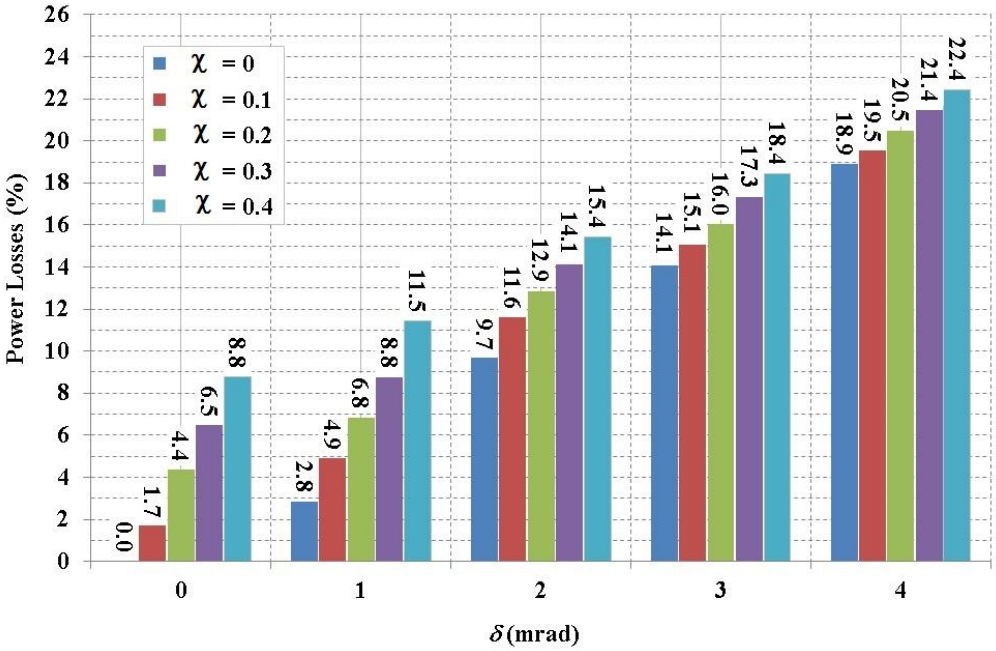

Figure 5.14: Bar chart to show the power losses in percentage for optimal configuration I with χ ranging from 0 to 0.4, and δ ranging from 0 to 4 mrad.

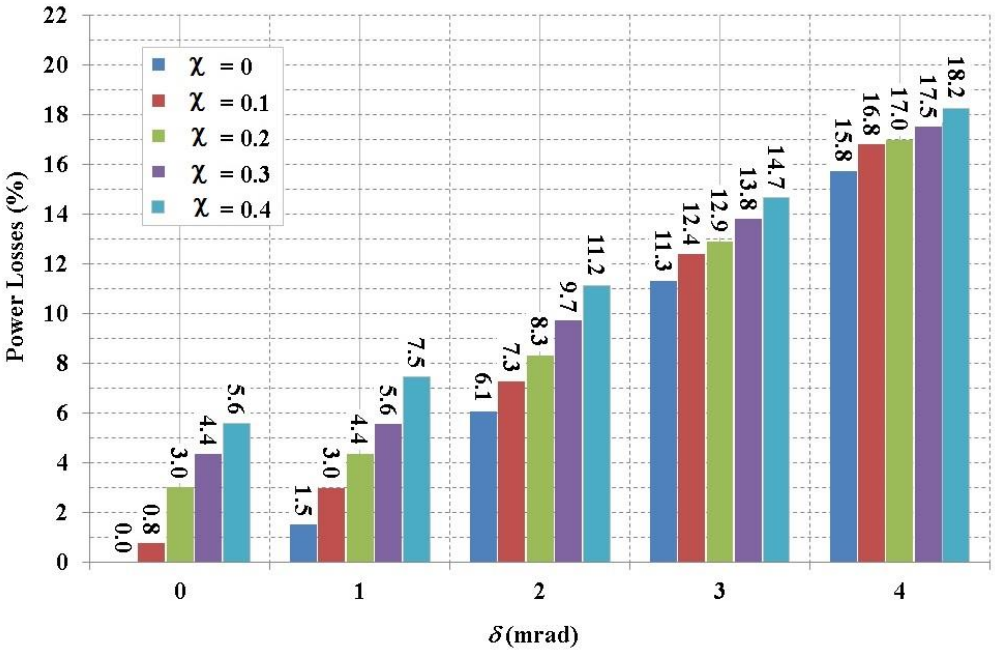

Figure 5.15: Bar chart to show the power losses in percentage for optimal configuration II with χ ranging from 0 to 0.4, and δ ranging from 0 to 4 mrad.

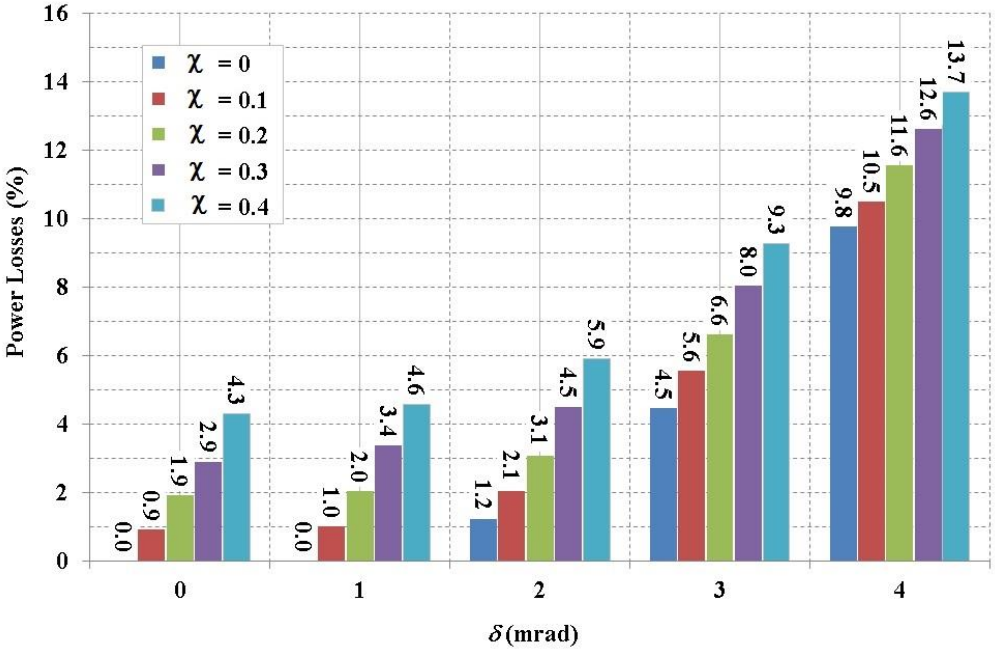

Figure 5.16: Bar chart to show the power losses in percentage for optimal configuration III with χ ranging from 0 to 0.4, and δ ranging from 0 to 4 mrad.

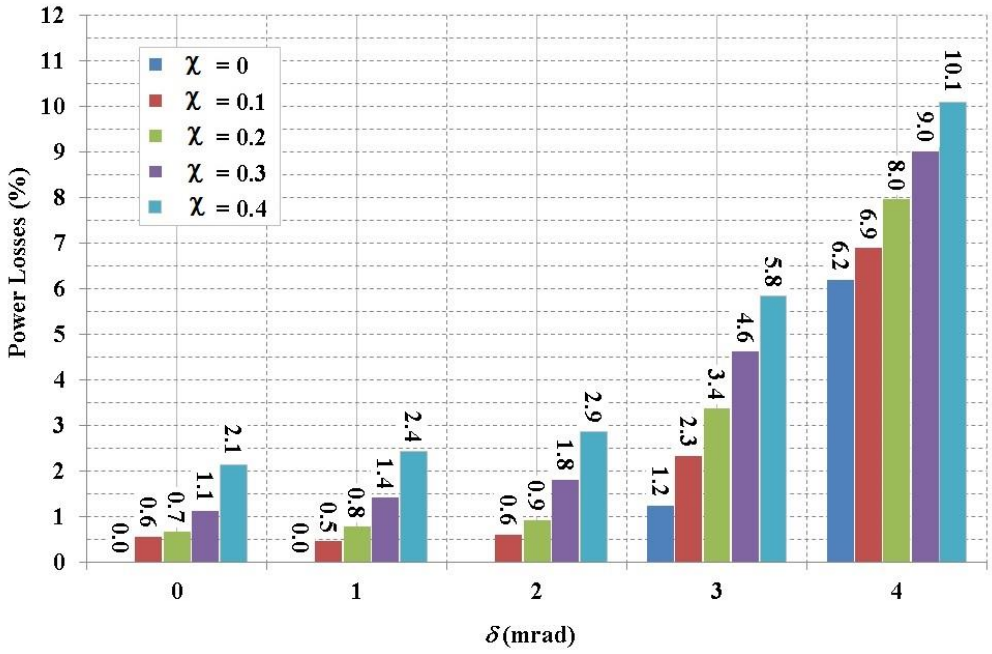

Figure 5.17: Bar chart to show the power losses in percentage for optimal configuration IV with χ ranging from 0 to 0.4, and δ ranging from 0 to 4 mrad.

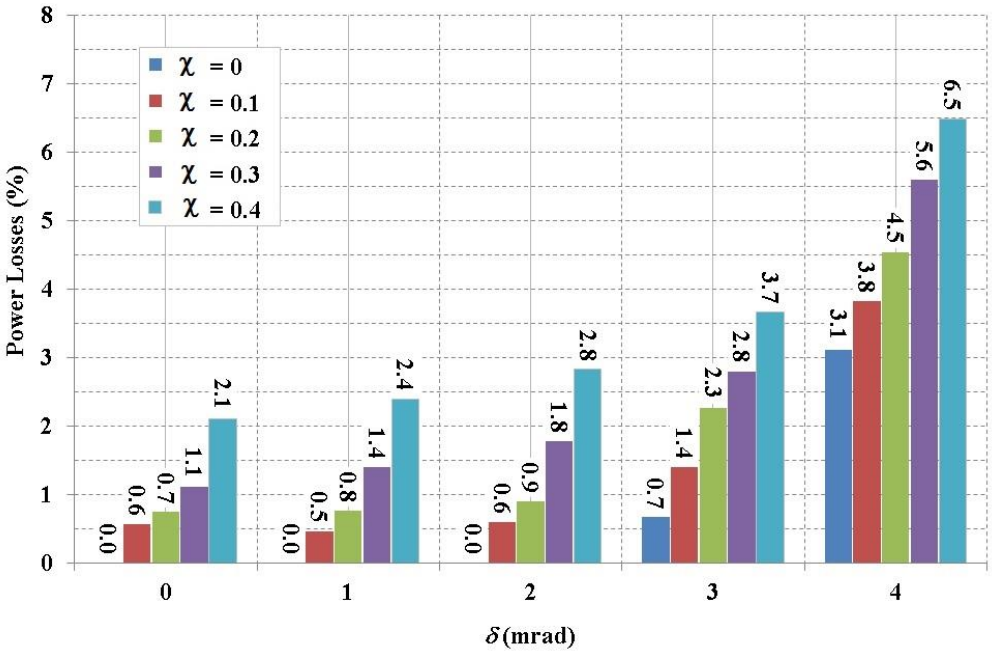

Figure 5.18: Bar chart to show the power losses in percentage for optimal configuration V with χ ranging from 0 to 0.4, and δ ranging from 0 to 4 mrad.

Figure 5.19 shows the comparison of electrical power losses among the five optimal configurations for the case of χ = 0.4 and δ = 4 mrad. The maximum power loss of 22.4 % (246.4 W) happens to the optimal configuration I when χ = 0.4 and δ = 4 mrad. Referring to Fig. 5.19, the optimal configuration V is the best configuration to minimize the electrical power losses caused by the increases of χ and δ. The maximum electrical power loss of this configuration is only 6.5 % (71.5 W) at χ = 0.4 and δ = 4 mrad. Consequently, the result shows that the optimal configuration V, which is designed based on the simulated flux distribution at the highest value of slope error, δ = 4 mrad, is capable of reducing the impacts of circumsolar radiation and slope error to the electrical performance of DACPV module.

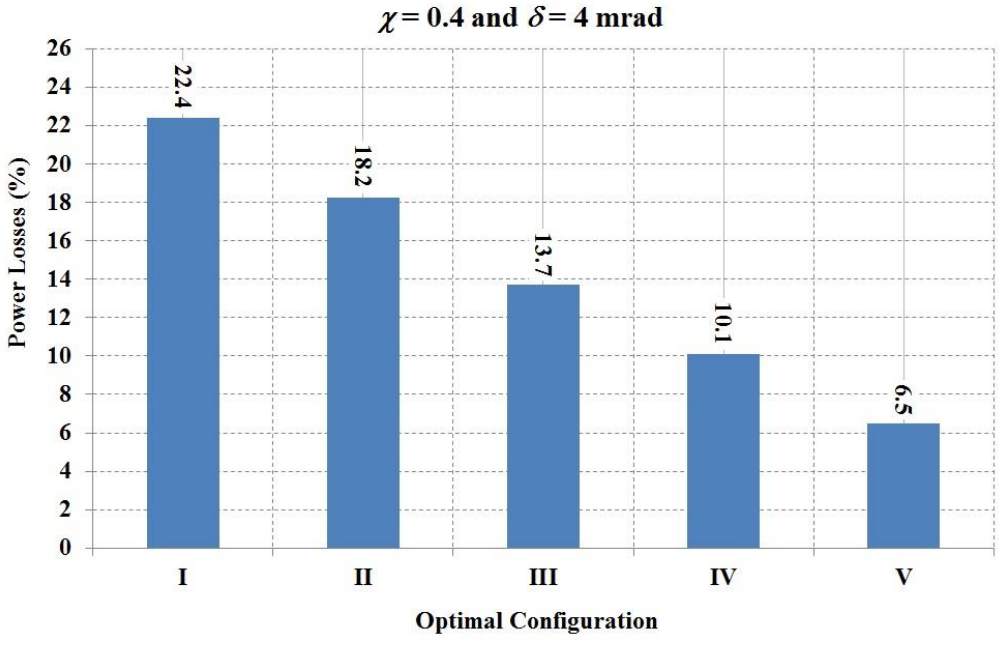

Figure 5.19: The comparison of electrical power losses among the five optimal configurations (i.e. optimal configuration I, II, III, IV and V) of DACPV module for the case of χ = 0.4 and δ = 4 mrad.

5.5 Summary

A systematic methodology to optimize the electrical performance of DACPV system has been proposed by considering both circumsolar radiation (χ) and mirror slope error (δ). Based on the simulated solar flux distribution, optimal electrical interconnection of solar cells in DACVP module can be designed by minimizing the current mismatch caused by non-uniformity of concentrated sunlight. The optimal configuration I, II, III, IV and V are the most optimized layout of solar cells interconnection circuits for the mirror slope error (δ) at 0, 1 mrad, 2 mrad, 3 mrad and 4 mrad respectively in the case of χ = 0. The optimal configuration V is the best configuration for the typical values of δ in the range from 0 to 4 mrad, and χ in the range from 0 to 0.4. The maximum electrical power loss of this configuration is only 6.5 % (71.5 W) as compared to the ideal case (zero values in χ and δ) that produces a maximum output power of 1.1 kW. As a result, the optimal configuration V is capable of reducing the impacts of circumsolar radiation and mirror slope error to the electrical performance of DACPV module.

CHAPTER 6

DESIGN AND CONSTRUCTION OF HIGH CONCENTRATED SOLAR FLUX SCANNER

6.1 Introduction

In DACPV system, an accurate and rapid measurement is necessary to obtain the solar flux distribution for each location of the solar cell on the receiver of a solar concentrator. The measured solar flux distribution can be used to validate the numerical simulation that is specially designed for modeling the solar flux distribution and optimizing the electrical interconnection of DACPV module.

For measuring low-intensity solar flux distribution less than 1000 W/m^2, an optical scanner consisted of silicon planar photodiode array has been proposed by the author and his research teammates (Chong and Yew, 2011; Chong et al., 2011). However, there are two drawbacks for the optical scanner: sensitive to limited solar spectrum range, from 400 nm to 1100 nm, and capable of measuring low solar irradiance, less than one sun. To overcome the limitations, the author proposed the use of triple-junction solar cells as the transducers for replacing the silicon planar photodiode in order to acquire high concentrated solar irradiance up to thousands of suns and covering the almost full spectrum of sunlight ranging from 300 nm to 1800 nm (Wong and Chong,

2016). Since the transducer used in the solar flux scanning device is the same type of solar cell to be assembled in the DACPV module, it is a perfect match for the characterization study of any new solar concentrator.

6.2 High Concentrated Solar Flux Scanner

A high concentrated solar flux scanner, also known as a flux mapping system, has been designed and constructed to acquire flux distribution profile of a solar concentrator. The profile is determined by measuring the short-circuit currents of the calibrated triple-junction solar cells. The advantage of this technique is that the triple-junction solar cell as transducer mounted on the scanner is the same type as that of assembled in the DACPV module. It has simplified post-processing layout design of the solar cell interconnection circuit in the DACPV module because the short-circuit currents of solar cells in their particular locations on the receiver have been measured directly via the scanner. Figure 6.1 illustrates the major components needed to construct the scanner, including an array of solar cells, relay module, current sensors, amplifier, microcontroller, stepper motor and computer. This system is controlled by a computer with a custom designed user interface program. It is capable of sending commands to the microcontroller to perform desired functions, such as to collect and to process the results of measurements.

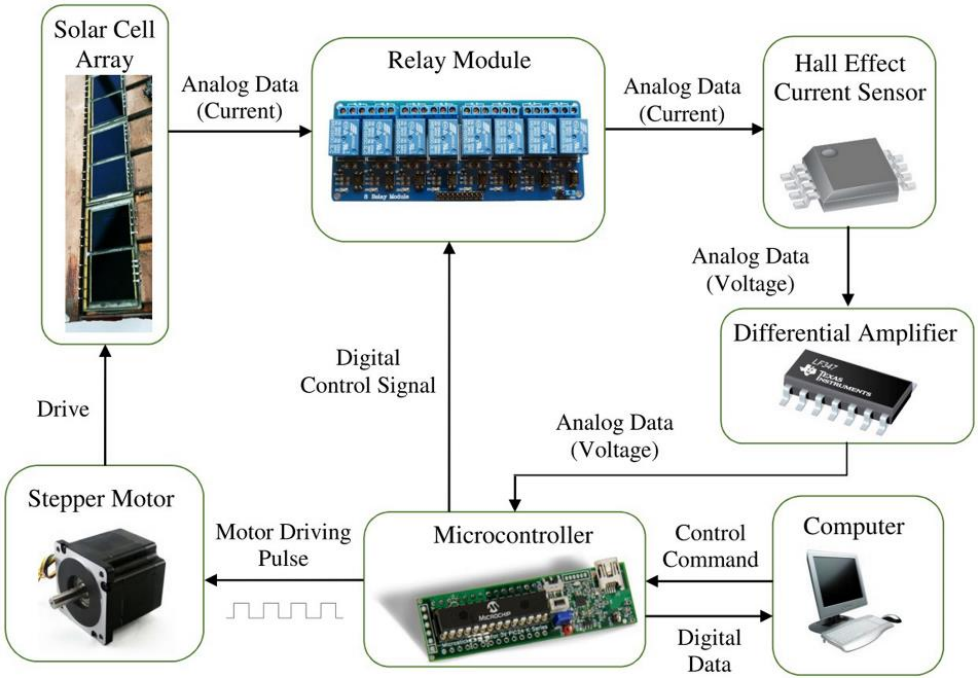

Figure 6.1: Schematic diagram to show the detailed configuration of high concentrated solar flux scanner.

6.2.1 Transducer

The EMCORE product of high-efficiency triple-junction solar cell (InGaP/InGaAs/Ge) with a dimension of 1.0 cm × 1.0 cm is chosen as a transducer for measuring the concentrated solar flux distribution focused on the receiver of a solar concentrator. The selection is essentially due to the solar cell has highly linear behavior and instantaneous response to high concentrated solar radiation, which ranges from hundreds to thousands of SCR. Figure 6.2 shows the external quantum efficiency of the solar cell with respect to the wavelength of incident sunlight (EMCORE Corporation, 2008).

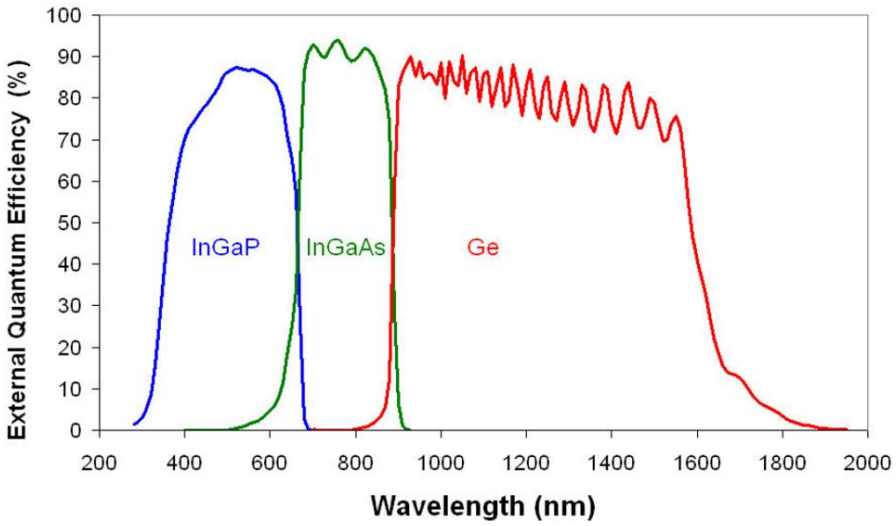

Figure 6.2: External quantum efficiency of the triple-junction solar cell with respect to the wavelength of incident sunlight provided by EMCORE Corporation (EMCORE Corporation, 2008).

The solar cell comprises of three different types of p-n junctions that are sensitive to different spectral ranges of the solar spectrum, i.e. InGaP (top junction, responsive to the range from 300 to 700 nm), InGaAs (middle junction, responsive to the range from 500 to 900 nm) and Ge (bottom junction, responsive to the range from 800 to 1800 nm) (EMCORE Corporation, 2008). The three junctions are connected in series and hence operating current of the solar cell is limited by the junction generated the least current. In general, the optimal electrical performance of the solar cell is designed based on AM1.5D spectral irradiance, and can be described as the current-voltage characteristic curve. When the solar cell is applied under local spectral irradiance different from AM1.5D spectrum, the electrical performance of the solar cell will be deviated from that of listed in the Emcore datasheet due to the spectral mismatch (Araki et al., 2003; Bonnet-Eymard et al., 2013; Pravettoni et al., 2013). According to the

datasheet by the manufacturer, current measurement demonstrates far better linearity than voltage measurement under different SCR (EMCORE Corporation, 2008). The short-circuit current produced by the solar cell increases linearly with SCR from one sun to as high as 1182 suns and thus the solar flux map on the receiver can be determined by purely measuring the short-circuit current of the solar cell.

6.2.2 Hardware Design

Instead of using a two-dimensional array of solar cells, the high solar flux scanner consists of twenty solar cells that are arranged in a linear array. The linear array of solar cells measures the solar flux map across a receiver plane in a direction from left to right. This linear scanning technique can significantly cut down the cost and complexity of the acquisition system for solar flux map with much less number of solar cells required. With a linear array, it is possible to have the arrangement of the solar cells with very minimum gap spacing between the adjacent cells that will affect the resolution of the solar flux distribution map. The resolution of the scanner is 1.0 cm $\times$ 1.2 cm equal to the dimension of the solar cell (1 cm $\times$ 1 cm) plus the gap spacing between the adjacent cells (1.0 cm $\times$ 0.2 cm) along the column direction.

Prior to the assembling of solar flux scanner, the electrical characteristics of solar cells must be investigated with the application of the semiconductor parameter analyzer to ensure all of the solar cells have almost

the same *I-V* characteristic. Electrical characterization is an important process to validate the cell quality by observing the *I-V* curve under illumination as well as the dark condition. The solar cells with the most similar electrical characteristics were selected and attached to direct bond copper (DBC) substrates, which has high thermal conductivity and high voltage isolation, to form a linear solar cell array through solder reflow process with a vacuum. The solder reflow process with a vacuum provides low void content bonding (bubbles in the finished solder joint) and excellent thermal conductivity between the solar cells and DBC substrates (see Figure 6.3). The DBC substrate is made of a ceramic isolator Al_2O_3 that is sandwiched in between two copper layers. The large void content bonding may degrade the performance of the solar cell since the thermal conductivity between the solar cells and DBC substrates is not uniform, which incurs hot-spot heating and high operating temperature. For that reason, low void content bonding is preferable in the application of CPV system.

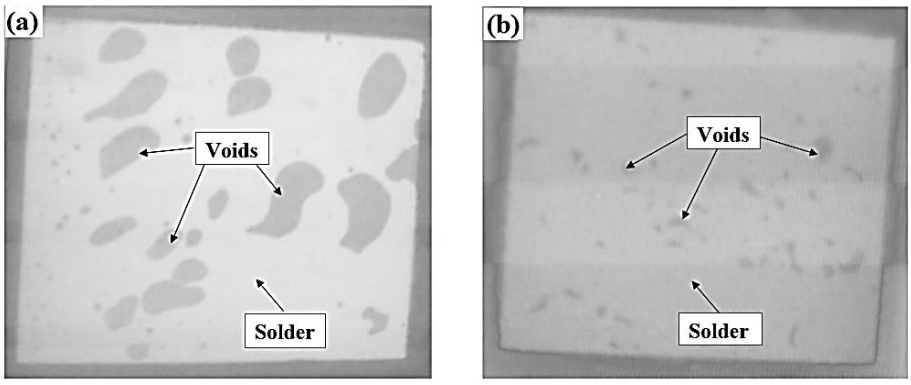

Figure 6.3: X-ray scanning is carried out after the solder reflow. (a) High void content bonding (without vacuum) and (b) Low void content bonding (with vacuum).

Since the rear contact or positive terminal of each solar cell is electrically connected to the same top layer of DBC substrates, the top layer is functioned as the common point of signal measurement. A cross-sectional sketch of various materials for the solar flux scanner assembled in stack is presented in Figure 6.4. The solar cells are encapsulated with conformal coating for increasing their chemical resistance, surface hardness, and moisture resistance. As sunlight is concentrated on the solar cells, the non-converted sunlight will generate heat and then cause the solar cell temperature to rise. The change in temperature of solar cells causes the change in the output currents of the cells that affect the measurement accuracy. As a result, the bottom layer of the DBC substrates is attached to a water-cooling block by high thermal conductivity adhesive to dissipate the accumulated heat so that the cells can operate at reasonably constant temperature during data acquisition.

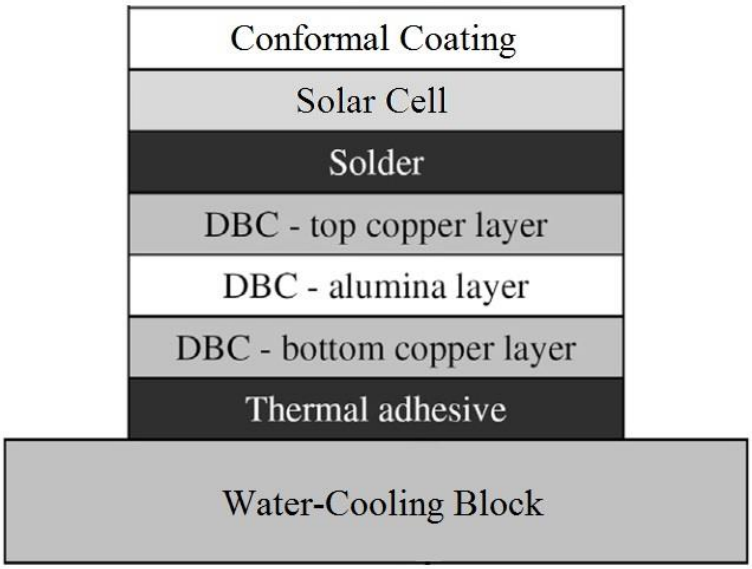

Figure 6.4: A cross-sectional sketch of various materials for the solar flux scanner assembled in stack.

The water-cooling block was mounted on a linear slider driven by a stepper motor via a metal chain. The stepper motor can be controlled by the step pulses generated by the microcontroller in which the microcontroller generates 405 pulses/s to drive the water-cooling block at a speed of 2.5 cm/s. The positioning of the water-cooling block has been proven robust, consistent, and high accuracy even after many measurement runs have been performed. Figure 6.5 shows the completed high solar flux scanner with a linear array of twenty multi-junction solar cells.

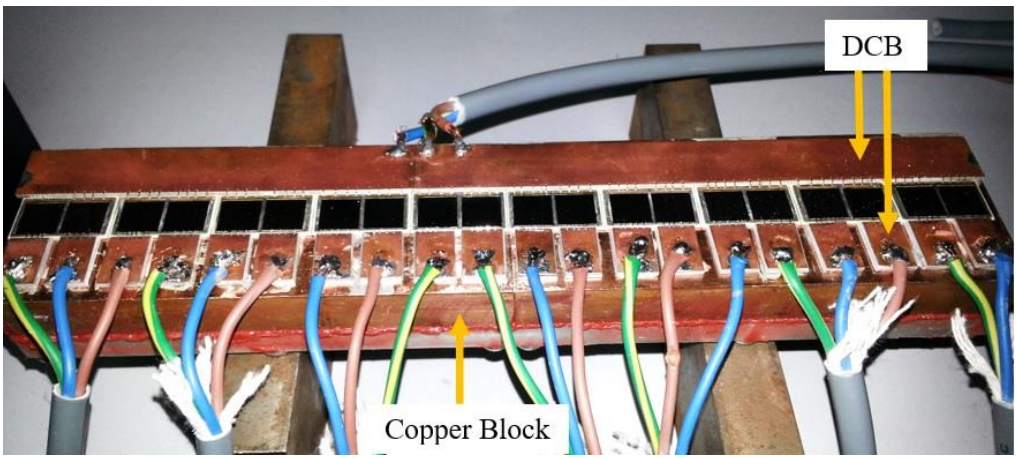

Figure 6.5: The completed high solar flux scanner consists of twenty solar cells that are arranged in a linear array.

6.2.3 Calibration of Solar Cells

After assembling of the scanner, onsite calibration is needed because the short-circuit current of solar cells responding to the local direct normal irradiance (DNI) might be different from that of listed in the Emcore

datasheet, which is calibrated based on AM1.5D spectrum. The onsite calibration is essential to eliminate the factor of spectral mismatch between local irradiance and AM1.5D irradiance. The short-circuit current of cells were calibrated against the DNI because direct sunlight is the key resource for the measured concentrated solar flux. During the calibration of solar cells, pyrheliometer and pyranometer were kept pointing towards direct sunlight while measurements of short-circuit current was carried out. The following three conditions were fulfilled during the calibration process, i.e. DNI was higher than 700 W/m^2, ratio of DNI to global solar irradiance (GSI) was greater than 0.7 and short-circuit current of the cell had shown a stable reading. The short-circuit current of solar cell that respond to the DNI can be calculated using the following equation:

$$I_{sc}^{\mathrm{DNI}} = I_{sc}^{measured} \frac{\mathrm{DNI}}{\mathrm{GSI}} \tag{6.1}$$

where $I_{sc}^{measured}$ is the measured short-circuit current of solar cell (mA), DNI is the direct normal solar irradiance reading from pyrheliometer (Wm^{-2}) and GSI is the global solar irradiance reading from pyranometer (Wm^{-2}).

Figure 6.6 shows a calibration graph for one of the solar cells used in the flux scanner. The data were selected from the measurement performed on three different days with clear sky conditions. The calibration graphs of all the twenty solar cells show an excellent linear relationship between short-circuit current under one sun, I_{sc}^{1} and local DNI with the R-squared values of all the linear graphs higher than 0.95.

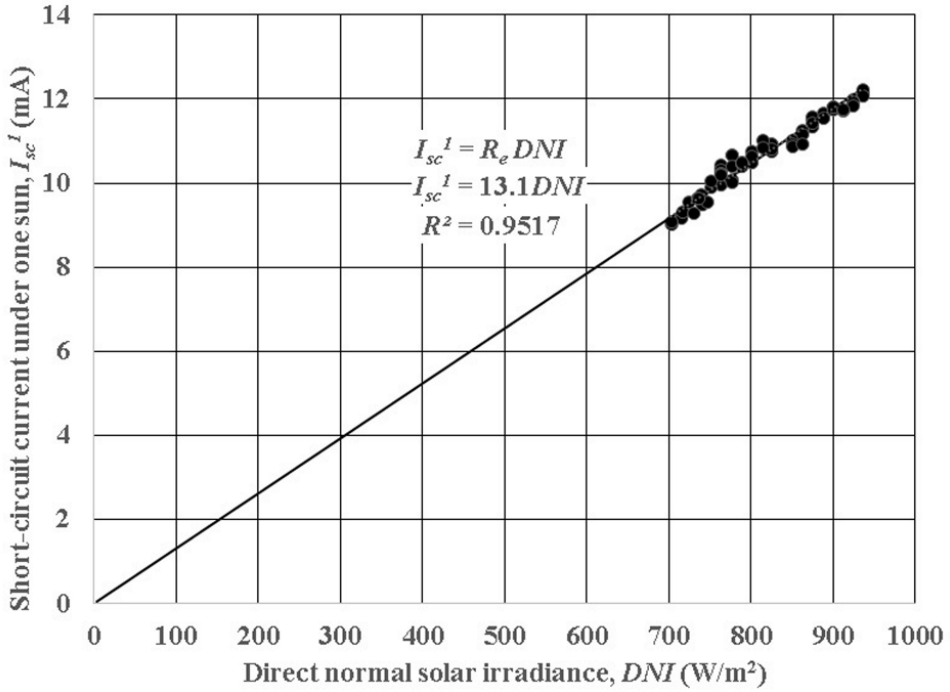

Figure 6.6: Calibration graph for one of the solar cells used in the high solar flux scanner. The calibration graphs of all the twenty solar cells show an excellent linear relationship between short-circuit current under one sun, I_{sc}^{1} and DNI with R^2 values of all the linear graphs higher than 0.95.

Regression analysis of the graphs was carried out to study the standard error of the regression lines for all the solar cells. The standard errors of all regression lines were calculated, and the errors were in the range between 0.19 mA and 0.20 mA. The standard errors of all regression lines provide simple measures of uncertainty in the calibrated short-circuit current of the solar cells. The standard errors can be caused by the uncertainties in irradiance (GSI and DNI) and current measurements as well as variation of local spectral irradiance.

The extrapolations of the calibrated values of the solar cells from one sun to 1182 sun are allowable based on the following two justifications. Firstly, the short-circuit current density (J_{sc}) under AM1.5D irradiance is linearly proportional to SCRs, i.e. 1 sun (J_{sc} = 13.85 mA/cm^2), 503 suns (J_{sc} = 6.96 A/cm^2) and 1182 suns (J_{sc} = 16.37 A/cm^2) as provided in Emcore datasheet (EMCORE Corporation, 2008). Secondly, the short-circuit current under local irradiance equals to about 95 % of the short-circuit currents under AM1.5D irradiance. The standard errors appear to be small, and hence, the linear regression model of I_{sc}^{1} as a function of the DNI was determined to be good. The calibrated short-circuit current of the solar cells can be represented by the following equation:

$$I_{sc}^{1} = R_e \mathrm{DNI} \tag{6.2}$$

where DNI is the direct normal solar irradiance reading from pyrheliometer (Wm^{-2}) and R_e is the responsivity per unit area of solar cell, which is a constant to describe the performance of cell in terms of the short-circuit current generated per incident optical power per unit area (mA/kWm^{-2}).

All the calibrated short-circuit current of solar cells under local irradiance are equal to about 95% of the corresponding short-circuit currents measured under AM1.5D spectrum (EMCORE Corporation, 2008). As a result, the effect of spectral mismatch between AM1.5D and local irradiances to the solar cells under clear sky conditions is not significant.

6.2.4 Signal Conditioning

For the solar flux distribution measurement, signal conditioning is necessary to convert the short-circuit current generated by the solar cell into a voltage that is required by the data acquisition (DAQ) device for digital data processing in a computer. The signal conditioning provides enhancement to both the performance and accuracy of DAQ device.

The three most common sensors to sense DC current are the resistive shunt, transimpedance amplifier, and Hall effect-based current sensor. The resistive shunt is simply a resistor placed in series with the solar cell. According to Ohm's law, the cell current can be determined by measuring the voltage drop across the known resistance. This technique offers the lowest cost and most accurate solution, but it is not suitable to be implemented for high current measurement. Resistive power dissipation that causes a heating effect becomes significant when a high current flows through the shunt resistor. This may induce an erroneous reading, and the resistor will rapidly deteriorate if it is operated near rated power without proper heat sinking. The transimpedance amplifier is a current-to-voltage converter. It is used to convert the current output of the sensor to a usable voltage by using an operational amplifier. The transimpedance amplifier presents a low impedance to the current sensor, and the output of the operational amplifier is isolated from the source. However, it is not suitable to be employed for designing the concentrated solar flux distribution measurement that is composed of a high input current. This is

mainly due to the amplifier is typically used to convert the low-level current of a sensor to a voltage.

In this study, Hall effect-based DC current sensing IC with measurable current ranging from 0 to 30 A is deployed to convert the short-circuit current into voltage. This device consists of a precise, low-offset and linear Hall circuit with a copper conduction path located near the surface of the die. This circuit converts the magnetic field generated by the copper conduction path to voltage linearly when current flows through the conduction path. It has an output sensitivity of 133 mV/A. The typical internal resistance of this conductive path is 1.2 mΩ, and it provides low resistive power loss. Hence, the device and solar cell are connected in series for determining the short-circuit current under the condition of approximately zero resistance load. This device can provide electrical isolation between the input, output and power supply. According to the datasheet, the output voltage of the instrument is desensitized to the effects of temperature and mechanical stress by using a chopper stabilization technique (Allegro, 2012). This technique also makes the device has an extremely stable offset voltage, which is the deviation of the instrument output from its ideal quiescent value due to nonmagnetic causes.

The differential amplifier is an essential interface between the Hall sensor and analog-to-digital converter (ADC). When the output voltage span of the sensor (in the millivolt range) and ADC input voltage span are unequal and offset, the sensor data is lost, and ADC dynamic range is not fully utilized. For the sake of achieving optimum performance, the differential amplifier is

used to shift and amplify the voltage span of the sensor to match the ADC voltage span ranging from 0 V to 5 V. A standalone Hall sensor with no input current is functioned as a reference sensor to provide the offset voltage for the amplifier. In addition to the offset voltage, the reference sensor is used to minimize the noise that is caused by the magnetic field from its surroundings. The amplifier can eliminate the error by shifting the noise voltage provided by the reference sensor.

After the voltage level shifting and amplification, the amplified voltage has to be converted to digital data via a microcontroller integrated with 13 channels of built-in 10-bit ADCs prior the data transferred to the computer. Owing to the limited number of ADC, multiplexers are required to extend the measurement channels of the microcontroller. An electronic circuit module consisted of ten single pole double throw (SPDT) relays functioned as 2-to-1 multiplexers or data selectors is used to measure the short-circuit currents from twenty solar cells. Figure 6.7 shows the schematic diagram of solar cells and the corresponding electronic circuit.

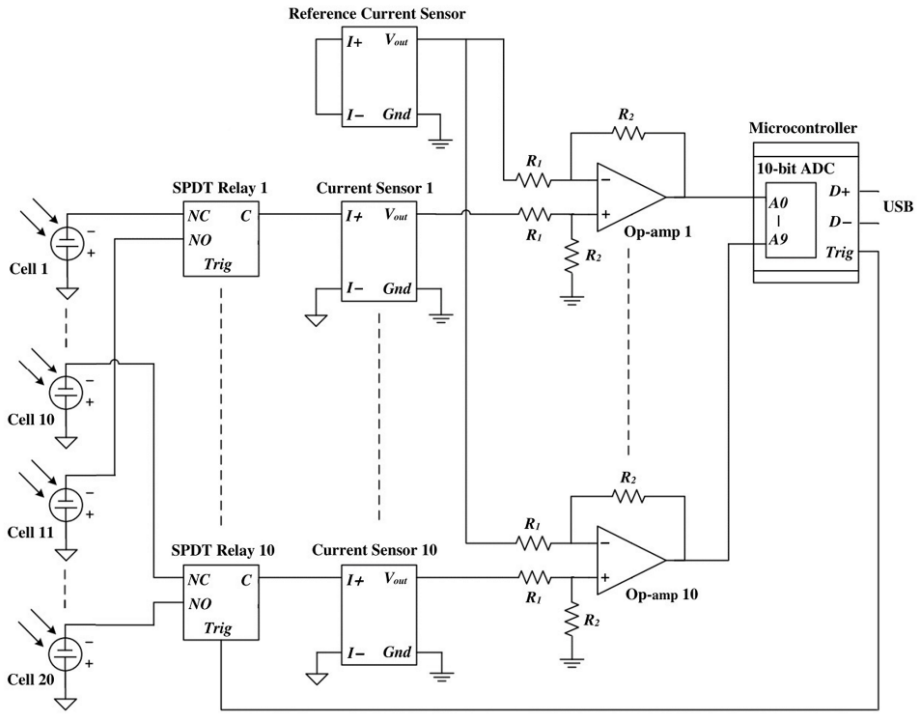

Figure 6.7: The electronic circuit layout of high solar flux scanner consisting of triple-junction solar cells and the corresponding electronic components.

The total response time of the signal conditioning circuit is determined by the acquisition and conversion time of the ADC, the slew rate of the differential amplifier, rise time of the current sensor and relay propagation delay time. The total acquisition and conversion time of the ADC is 4.2 μs. The amplifier has a slew rate of 8 V/μs. It takes 0.625 μs to increase from 0 V to 5 V, which is the maximum voltage read by the ADC. The current sensor has an output rise time of 5 μs and the delay time of the relay is 15 ms. The total response time is approximately 15 ms, which includes time taken from a signal acquired by the solar cell to converting it into a digital signal and finally to store the signal in the register. The response time of the data acquisition system is sufficiently fast as compared to the time taken for shifting the linear array of solar cells by 1 cm, which is approximately 0.4 s.

6.2.5 Calibration of Electronic Circuit

Prior to the measurement, the 10-bit ADCs output has been calibrated indoor by using variable current sources to replace output current from the solar cells as shown in Figure 6.7. The purpose of calibration is to eliminate the measurement error arisen from ADC conversion error and various noises of electronic circuits including relays, current sensors, and amplifiers. A custom designed user interface program is used to calculate the ADCs output in terms of analog voltage. Figure 6.8 shows an excellent linear relationship between one of the ADCs output voltages and the input current ranging from 0.1 A to 3.0 A. Regression analysis of all the calibration graphs have been performed to study the standard errors of the regression lines. The standard errors of all regression lines are within the range from 4.38 mA to 10.07 mA.

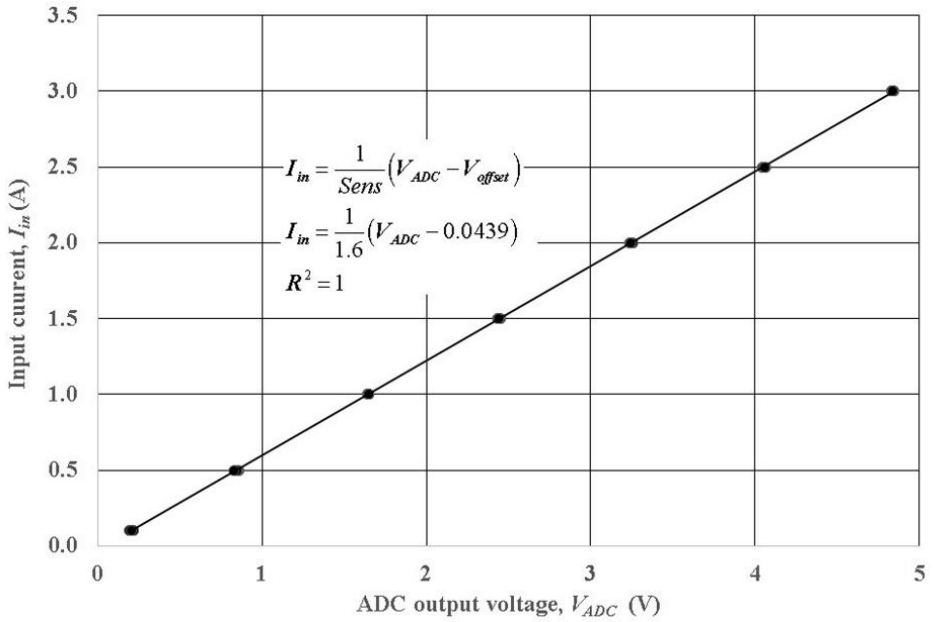

Figure 6.8: Linear relationship is shown in a graph between one of the ADCs output voltage and input current source range from 0.1 A to 3.0 A.

According to "Evaluation of measurement data: Guide to the expression of uncertainty in measurement", the uncertainties in the measurement of the short-circuit current under one sun (I_{sc}^{1}) and the input current measured by the signal conditioning circuit (I_{in}) are considered as Type A of standard uncertainty (JCGM, 2008). Therefore, the standard errors of all regression lines, which is determined by using regression analysis on the calibration graphs, are the uncertainties in the measurement of I_{sc}^{1} and I_{in}. The standard errors, also known as the standard uncertainty, of the measured input current is mainly contributed by the electrical uncertainties arise from the data acquisition system. The input current measured by the signal conditioning circuit can be calculated as

$$I_{in} = \frac{1}{Sens}\left(V_{ADC} - V_{offset}\right) \tag{6.3}$$

where *Sens* is the calibrated sensitivity of the signal conditioning circuit (V/A), V_{ADC} is the 10-bit ADC output voltage (V), and V_{offset} is the offset voltage caused by the ADC conversion error and offset from the electronic circuit (V).

6.3 Onsite Measurement

Figure 6.9 shows the experimental setup of high solar flux scanner for the onsite measurement of high concentrated solar flux distribution produced by NIDC prototype. The high solar flux scanner was installed at the receiver plane of the NIDC in such a way that the surface of linear array solar cells is

always normal to the optical axis of the concentrator. For a complete measurement, a total of 500 readings per full scanning is taken by the linear array of twenty solar cells to acquire the solar flux map with the total surface area of 25 cm × 24 cm on the receiver plane. The high solar flux scanner is capable of performing a complete measurement cycle within a period of 10 s.

Figure 6.9: Experimental setup of the high solar flux scanner to measure solar flux distribution of NIDC prototype consisting of 96 flat facet mirrors with a dimension of 20 cm × 20 cm each and focal distance of 210 cm.

Before the onsite measurement, the prototype is orientated to face the direct sunlight by using the most common two-axis sun-tracking system, which is the azimuth-elevation tracking system. Afterward, a command is sent to the microcontroller via the computer user interface to check the USB communication status. Referring to Figure 6.10, the flowchart illustrates the algorithm of how the solar flux scanner can obtain the concentrated solar flux

distribution. The measurement process can be started by moving the water-cooling block where the solar cell array is mounted for 1cm via stepper motor when the USB connection is detected. For moving the water-cooling block, the microcontroller has to calculate the number of step pulses needed by the stepper motor for 1 cm of movement. The microcontroller generates the required number of step pulses for driving the stepper motor after completing the calculation.

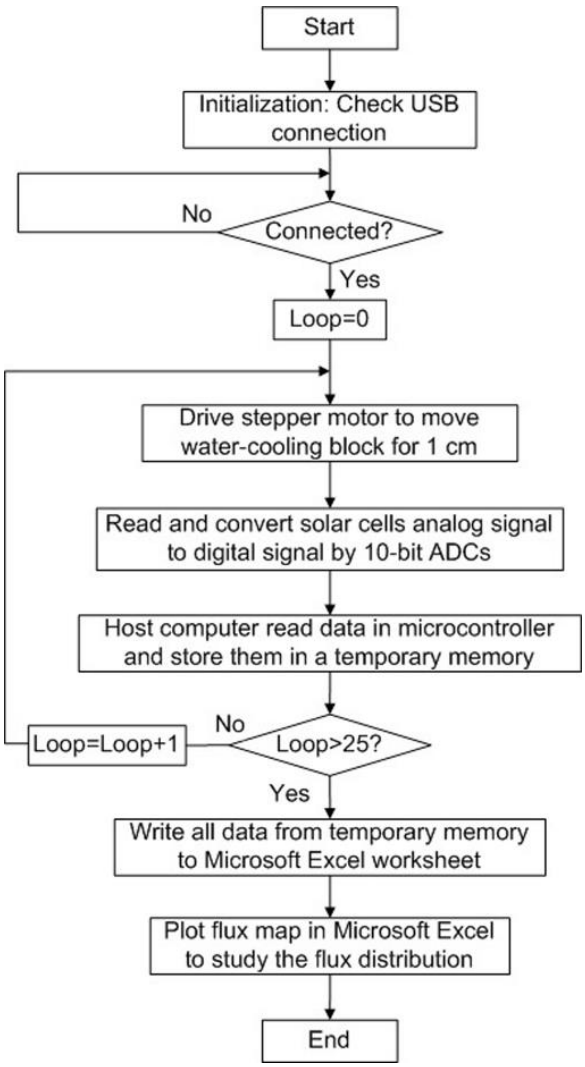

Figure 6.10: Flowchart shows the algorithm of data acquisition system of high solar flux scanner made of a linear array of triple-junction solar cells.

For each centimeter of movement of the water-cooling block, the microcontroller acquires the analog data from all the solar cells simultaneously through the signal conditioning circuit. The analog data are converted to the digital data via the 10-bit ADCs. The digital data are then stored in the USB communication registers in the microcontroller. After completing the conversion process, the host computer read the digital data in registers and stores them in a temporary memory. This data collection process is repeated 25 times. That is equal to 25 cm in the distance of the water-cooling block has been moved. After the measurement has completed, the data collected are written to a Microsoft Office Excel worksheet, and the flux map is then plotted. In this study, the flux map is represented by the measured SCR, $C_{measured}$ and it can be determined by the following equation:

$$C_{measured} = \frac{I_{in}\left[1-\alpha(T_{cell}-25)\right]}{I_{sc}^{1}} \tag{6.4}$$

where I_{in} is the measured short-circuit current that is generated by the solar cell under concentrated flux distribution, α is the temperature coefficient of short-circuit current (α = 0.065 %/℃), T_{cell} is the temperature of the solar cell during measurement in ℃, I_{sc}^{1} is the calibrated short-circuit current that responses linearly to DNI.

The high-speed scanning can reduce the problem of heat management of the solar cell array due to the short exposure time to solar radiation. The initial and final positions of the array are set to be off from the flux

distribution area so that the solar cells are not heated up before or after the scanning process. Furthermore, the solar cells are attached to the water-cooling block for improving heat dissipation and preventing the solar cells operate at high temperature during the scanning process. In order to study the effectiveness of the heat dissipation of water-cooling block, the solar cells on the solar flux scanner are used as the temperature sensors. According to the literature (Ju et al. 2013), the operating temperature of a solar cell can be estimated by measuring its open-circuit voltage, V_{OC}.The solar cell operating temperature (T_{cell}) in °C can be determined by the equation

$$T_{cell} = T_r + \frac{V_{OC} - V^1_{OC} - N\frac{kT_r}{q}\ln C}{\beta + N\frac{k}{q}\ln C} - 273 \qquad (6.5)$$

where T_r is the solar cell standard operating temperature (T_r = 298 Kelvin), V_{OC} and V^1_{OC} are open-circuit voltage of the solar cell under concentrated sunlight and one sun respectively, C is the SCR (suns), N is the effective diode ideality factor, k is the Boltzmann constant, q is the electronic charge and β is the temperature coefficient of open-circuit voltage (β = -7.6 mV/℃).

Several real-time open-circuit voltage (V_{OC}) measurements of the solar cells on the solar flux scanner were carried out under concentrated sunlight. The open-circuit voltages of the solar cells under concentrated sunlight and one sun are 2.88 V and 2.6 V respectively. The solar cells operating temperature can be determined by using Eq. (6.5) with the measured open-

circuit voltage (V_{OC} = 2.88 V and V^{1}_{OC} = 2.6 V). By assuming the effective diode ideality factor, N = 3 and C = 88 suns (the highest SCR modeled in Chapter 4), the solar cell operating temperature is 35 ℃, which is 10 ℃ higher than the standard operating temperature. In this case, the temperature effect on the accuracy of the SCR measurement is negligible by referring to Eq. (6.4).

6.4 Results and Discussions

Under clear sky condition, several real-time measurements of solar flux distribution profiles were acquired using the high solar flux scanner installed at the receiver plane. At the same time, GSI and DNI of the sunlight were measured by using pyranometer and pyrheliometer respectively. The results show that the measurements of solar flux distribution map are repeatable under similar weather conditions. Figure 6.11 shows one of the measured solar flux distribution maps with the resolution of 20 × 25 pixels (each pixel is 1.0 cm × 1.2 cm) equivalent to 24 cm × 25 cm of receiver area for NIDC prototype. According to the results, NIDC is capable of producing a flat-topped, non-Gaussian type of solar flux distribution.

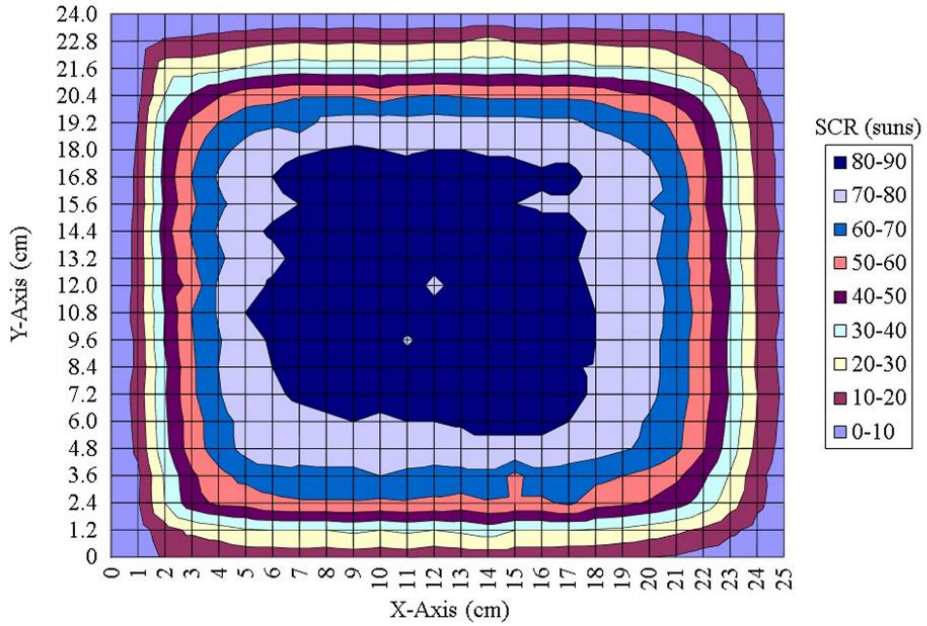

Figure 6.11: Measured solar flux distribution map with the resolution of 20 × 25 pixels (each pixel is 1.0 cm × 1.2 cm) equivalent to 24 cm × 25 cm of receiver area for NIDC prototype by using high solar flux scanner.

The prominent data of the solar flux distribution measurement presented in Figure 6.11 is summarized in Table 6.1. In this study, a measurement uncertainty analysis has been carried out. The uncertainties in the measurement of high concentrated solar flux distribution are mainly contributed by the uncertainty of the input current measured by the signal conditioning circuit (ΔI_{in}) and the uncertainty of the calibrated cell short-circuit current under one sun (ΔI_{sc}^{1}). By using the propagation of error formula, the measurement error of the high solar flux scanner can be calculated as

$$\Delta C_{measured} = \pm C_{measured} \sqrt{\left(\frac{\Delta I_{in}}{I_{in}}\right)^2 + \left(\frac{\Delta I_{sc}^{\ 1}}{I_{sc}^{\ 1}}\right)^2} \tag{6.6}$$

According to the calibration results, the values of ΔI_{in} are in the range from 4.38 to 10.07 mA and ΔI_{sc}^{1} range from 0.19 to 0.20 mA. For the average measured SCR of 82 suns in the uniform illumination area as shown in Table 1, the values of I_{in} and I_{sc}^{1} are 0.79 A and 9.52 mA respectively. As a result, the measurement error of the flux scanner is approximate $\Delta C = \pm 2$ suns.

Table 6.1: Summary of measured data for solar flux distribution measurement.

Global solar irradiance, GSI (Wm^{-2})	998
Direct normal irradiance, DNI (Wm^{-2})	727
DNI / GSI	0.73
Uniform illumination area (cm^2)	171.6
Average SCR in the uniform illumination area (suns)	82 ± 2*

* Measurement error of the flux scanner calculated by using the propagation of error formula

A comparison has been made between the solar flux profile modeled by numerical simulation and the solar flux profile measured by high flux scanner. Figure 6.12 shows the comparison of the measured flux profile (dotted line) and the modeled flux profile (solid line) by assuming unity mirror reflectivity and zero value for parameters ε, δ and χ. The modeled flux distribution has to be scaled by a factor of 0.93 to match the SCR in the uniform illumination area of the measured distribution. As shown in Figure 6.12, the measured flux distribution has narrow uniform illumination region and the broad base region as compared to the modeled flux distribution. The measured uniform flux distribution is about 50% less than the modeled uniform flux distribution. As discussed in Chapter 4, this phenomenon can be caused by the imperfection factors, i.e. mirror surface slope error and

circumsolar radiation (Wong et al., 2015). Moreover, the optical misalignment angles of the facet mirrors can be another factor that distorts the solar flux distribution.

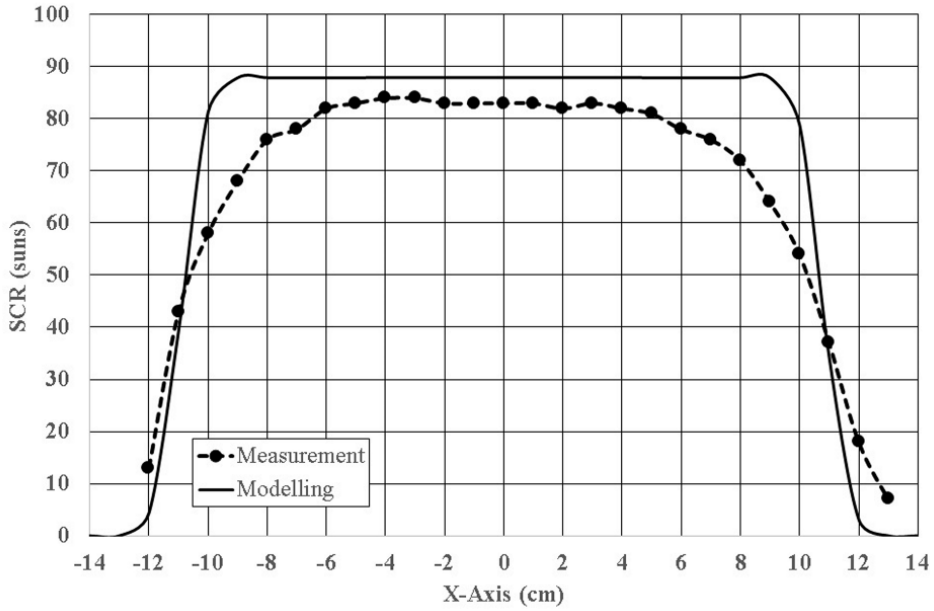

Figure 6.12: Comparison between the measured flux profile (dotted line) and the modeled ideal flux profile (solid line) at unity mirror reflectivity, $\varepsilon = 0°$, $\delta = 0$ mrad and $\chi = 0$.

For matching with the measured flux profile, the flux distribution of the NIDC has been simulated using the aforementioned ray-tracing method by changing the values of ε in the range from 0 to 0.3°, δ in the range from 0 to 4 mrad, and χ in the range from 0 to 0.2. According to Blanc et al. (2014), it has been verified that the value of χ is less than 0.2 if the DNI under clear sky condition is higher than 700 Wm^{-2}. In this study, the root-mean-square deviation (RMSD) is defined to quantify the difference between the simulated

SCR by ray-tracing method and the measured SCR by high flux scanner, which is expressed as follows:

$$\mathrm{RMSD} = \sqrt{\frac{\sum_{t=1}^{T}\left(C_{\mathrm{modeled},t} - C_{\mathrm{measured},t}\right)^{2}}{T}} \tag{6.7}$$

where T is the total number of readings.

Referring to Figure 6.13, the flowchart illustrates the procedure of how to determine the RMSD between the flux profile modeled by numerical simulation and the flux profile measured by high flux scanner with the application of Microsoft Office Excel. The process is started by inserting the SCR values, $C_{measured}$, of measured flux map (20 × 25 pixels of readings as shown in Figure 6.11) in 2-D matrix array into the corresponding arrangement of 20 × 25 cells in a Microsoft Office Excel sheet. The simulated solar flux distribution with the dimension of 24 cm × 25 cm is also sub-divided into 20 × 25 pixels (each pixel with an area of 1.0 cm × 1.2 cm) in which average SCR value, $C_{modeled}$, is computed for each pixel. Subsequently, the computed SCR values, $C_{modeled}$, are also written into the corresponding arrangement of 20 × 25 cells of Microsoft Office Excel sheet. By mapping the value of $C_{modeled}$ to the value of $C_{measured}$ based on their respective positions on the receiver plane, the RMSD is determined for each pixel by using the Eq. (6.7). The calculation is repeated for 500 times because there is a total of 500 pixels per receiver plane with a total surface area of 25 cm × 24 cm.

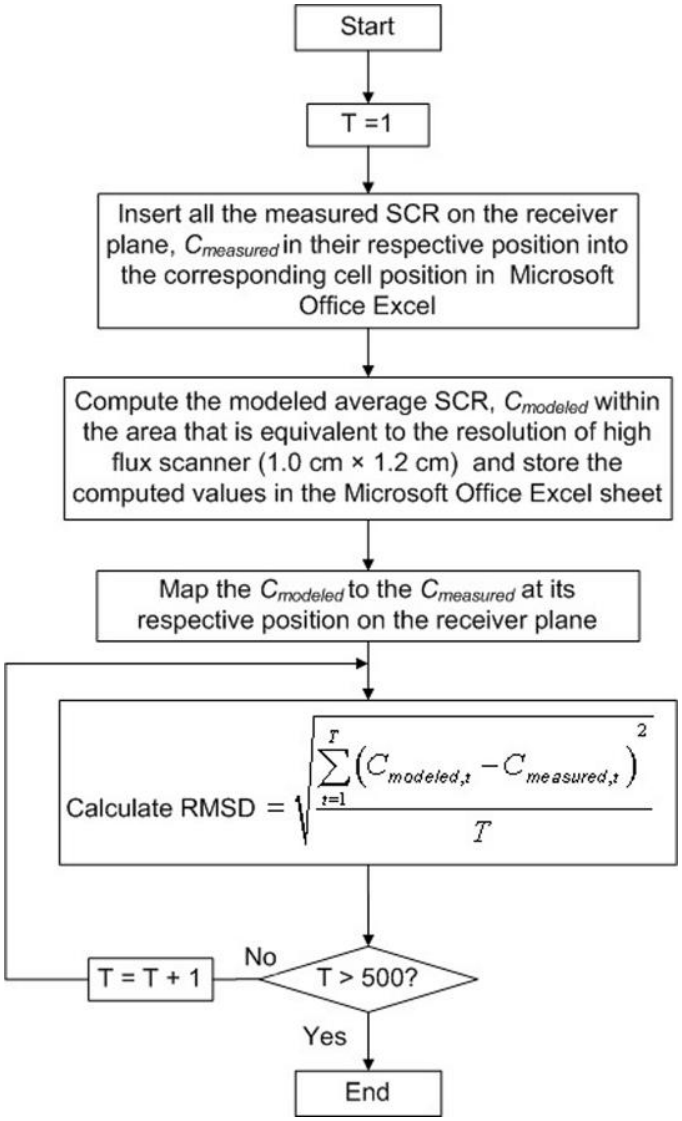

Figure 6.13: Flowchart to show algorithm of systematic technique to determine the root-mean-square deviation (RMSD) of the solar flux profile between simulated and measured results by high solar flux scanner.

The comparison of RMSD between the two flux profiles for the values of ε in the range from 0 to 0.3°, δ in the range from 0 to 4 mrad, and χ in the range from 0 to 0.2 have been calculated and summarized in Table 6.2. The summarized data are utilized to estimate the three imperfection factors (ε, δ andχ) of the NIDC prototype. According to the data shown in Table 6.2, the

smallest RMSD between the measured and simulated flux profiles is 3.18 suns at $\varepsilon = 0.2°$, $\delta = 3$ mrad and $\chi = 0.1$. The result indicates that the facet mirrors of NIDC prototype have the average slope error of 3 mrad and optical misalignment angles of 0.2°. Besides, the scaling factor of 0.93 can be used as the measure of average mirror reflectivity for the NIDC prototype.

Table 6.2: Summary of root-mean-square deviation (RMSD) between modeled and measured solar flux distribution.

		RMSD (suns)			
δ (mrad)	χ	$\varepsilon = 0°$	$\varepsilon = 0.1°$	$\varepsilon = 0.2°$	$\varepsilon = 0.3°$
0	0	10.98	8.42	5.35	5.39
	0.1	9.83	8.10	5.06	5.14
	0.2	8.88	7.30	4.89	5.01
1	0	9.63	8.07	5.73	4.95
	0.1	8.60	7.53	5.37	4.98
	0.2	7.75	6.83	5.35	5.72
2	0	6.90	5.88	4.19	4.38
	0.1	6.13	5.20	3.81	4.37
	0.2	5.52	4.67	3.55	4.40
3	0	4.42	3.82	3.28	4.30
	0.1	3.97	3.45	3.18	4.43
	0.2	3.66	3.21	3.19	4.56
4	0	3.50	3.36	3.76	5.19
	0.1	3.49	3.39	3.93	5.41
	0.2	3.55	3.47	4.10	5.61

Figure 6.14 shows the superposition of the measured flux profile (dotted line) and the modeled flux profile (solid line) at a mirror reflectivity of 0.93, ε = 0.2°, δ = 3 mrad and χ = 0.1. The modeled flux distribution illustrated in Figure 6.14 is correlated closely with the measured flux distribution. The comparison shows that the estimated three imperfection factors of NIDC prototype are reasonable. The RMSD value of 3.18 suns is slightly higher than the measurement error of flux scanner (2 suns) as listed in Table 6.1. It may be caused by the resolution of the flux scanner and the sun-tracking error that makes the measured flux distribution shifted from the center of receiver plane.

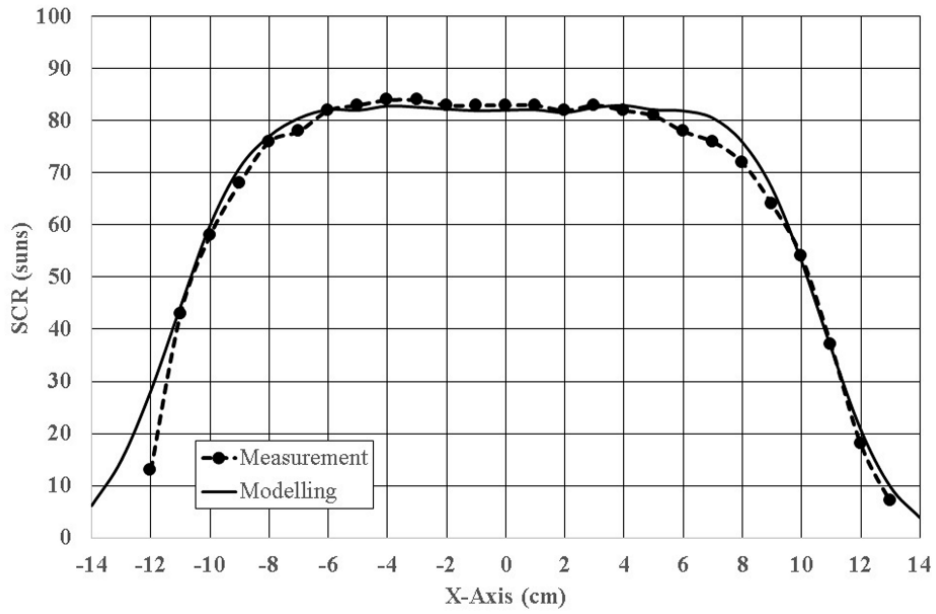

Figure 6.14: Comparison between the measured flux profile (dotted line) and the modeled flux profile (solid line) by setting the imperfection factors as mirror reflectivity of 0.93, ε = 0.2°, δ = 3 mrad and χ = 0.1.

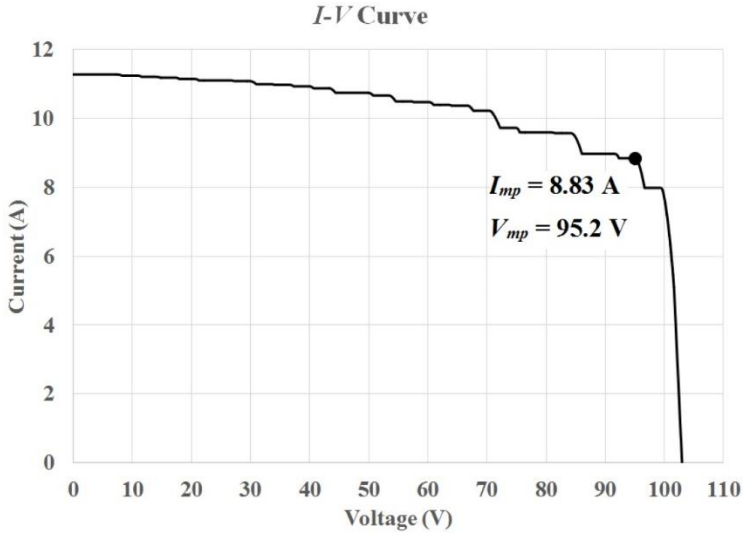

(a)

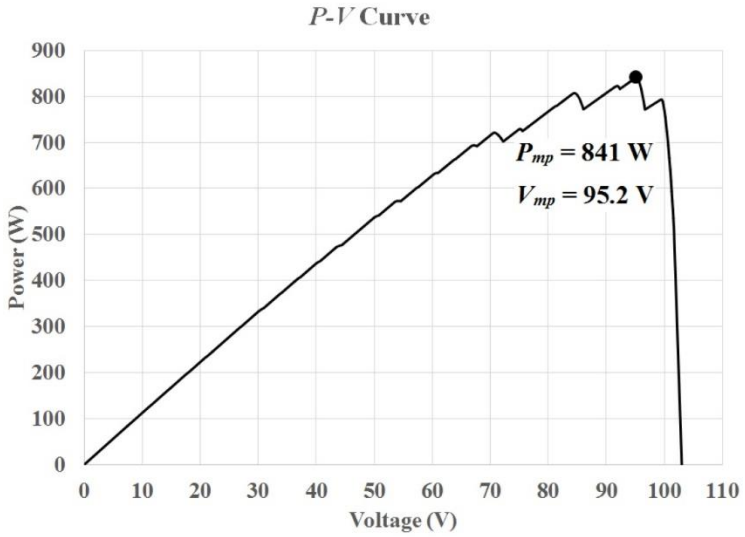

(b)

Figure 6.15: (a) *I-V* curve; (b) *P-V* curve for the optimal configuration V of DACPV module for the case of mirror reflectivity of 0.93, ε = 0.2°, δ = 3 mrad and χ = 0.1.

By using the best configuration of DACPV module as designed in Chapter 5, the optimal configuration V, *I-V* and *P-V* curves have been simulated for the case of mirror reflectivity of 0.93, ε = 0.2°, δ = 3 mrad and χ = 0.1 (see Figure 6.15). The electrical power loss is calculated by using the Eq.

(5.6). According to the results, the imperfection factors i.e. mirror reflectivity, mirror surface slope error, circumsolar radiation and optical misalignment cause a power loss of 23.6 % (260 W) as compared to the ideal case without considering the three imperfection factors. As presented in Chapter 5, the ideal case can produce a maximum output power of 1.1 kW.

6.5 Summary

A high solar flux scanner has been designed and constructed to acquire solar flux distribution profile of a non-imaging dish concentrator (NIDC). The scanner is capable of acquiring high concentrated solar flux distribution up to 1182 suns accurately and rapidly using an array of triple-junction solar cells. A systematic technique has been proposed to analyze the amount of various imperfection factors for the NIDC prototype by comparing the modeled and measured solar flux distribution profiles. Based on the results, average mirror reflectivity of 0.93, slope error of 3 mrad, circumsolar ratio of 0.1 and optical misalignment angles of 0.2° have been obtained. By using the optimal configuration V of DACPV module as designed in Chapter 5, the electrical power loss of the NIDC prototype with the imperfection factors is 23.6 % (260 W) as compared to the ideal case (without considering the imperfection factors) that produces a maximum output power of 1.1 kW. This shows that the imperfection factors can cause serious degradation in the electrical output power of a DACPV module.

CHAPTER 7

CONCLUSIONS AND FUTURE WORKS

7.1 NIDC System

The principle and the methodology of numerical simulation for analyzing the optical characteristics of the NIDC have been described in detail. From the simulated results, the author can conclude that the imperfection factors, i.e., circumsolar ratio, mirror slope error and optical misalignment can cause serious deterioration to the uniform flux distribution area and the percentage of energy within the uniform illumination area. The influence of the optical misalignment and slope error to the flux distribution at the receiver is more significant compared to that of the circumsolar radiation. In addition, the simulated results are very useful for the designer to optimize the size of the receiver by considering the spillage losses. In this research, the receiver with a dimension of 25 cm × 25 cm is chosen to capture more than 95% of solar irradiance. In general, the simulated results have shown a reasonably good uniformity of solar illumination and high SCR at the receiver plane. All the optical characteristics have strongly recommended that the NIDC is very suitable for the application in the DACPV system. It will be a cost-effective alternative with a simple mechanical, structural design and relatively low fabrication cost as compared to the other CPV systems.

7.2 Performance Optimization of DACPV System

A systematic approach to optimizing the electrical performance of DACPV system has been developed by considering both the effects of circumsolar radiation (χ) and mirror slope error (δ). The methodology to optimize the layout of solar cells interconnection circuit in DACPV module has been proposed. The optimal configuration I, II, III, IV and V are the most optimized layout of solar cells interconnection circuits, which are designed based on the simulated flux distribution with slope error at 0, 1 mrad, 2 mrad, 3 mrad and 4 mrad respectively in the case of $\chi = 0$. The optimal configuration V is the best configuration to minimize the electrical power losses caused by the increases of χ and δ. At $\chi = 0.4$ and $\delta = 4$ mrad, the maximum electrical power loss of this configuration is only 6.5 % (71.5 W) as compared to the ideal case (without considering imperfection factors) that produces a maximum output power of 1.1 kW. With this technique, the performance of DACPV system can be optimized for any concentrator such as a parabola, lens, and non-imaging concentrator with the use of any standard solar cells in the market. As a conclusion, a comprehensive study has been carried out to optimize the electrical output power of DACPV system by considering the circumsolar ratio and slope error in the solar flux distribution.

7.3 High Concentrated Solar Flux Scanner

A concentrated solar flux scanner equipped with an array of triple-junction solar cells has been constructed to measure the solar irradiance across a receiver plane of NIDC. The methodology and practical demonstration of the scanner are reported in details. The flux scanner has a linear behavior and instantaneous response to high concentrated solar radiation of thousands of SCR. By using the calibrated triple-junction solar cells as the transducers, the flux scanner is capable of acquiring the concentrated solar flux distribution profile on the receiver of NIDC prototype in a short period time of 10 seconds. The measured solar flux distribution shows deviation from a perfect uniform distribution owing to various imperfection factors.

According to the comparison study between the modeled and measured solar flux distribution profiles, the NIDC prototype with a peak SCR of 82 suns and an average mirror reflectivity of 0.93. Moreover, a systematic technique has been developed to analyze imperfection factor of NIDC prototype. By determining the root-mean-square deviation (RMSD) of the solar flux profile between simulated and measured results, slope error of 3 mrad, the circumsolar ratio of 0.1 and optical misalignment angles of 0.2° have been obtained. As a conclusion, the flux scanner can perform real time and direct measurement of high concentrated flux distribution profile with a good degree of accuracy and fast scanning speed. The study is significant to any newly constructed solar concentrator for the application of DACPV module consisted of solar cells same type as that of the solar cells mounted on

the high flux scanner. Less post-processing is required to design the layout of the solar cell interconnection circuit in the DACPV module since the short-circuit currents of solar cells can be measured directly via the flux scanner.

7.4 Concluding Remarks and Future Works

The overall aims of this research are to develop a novel NIDC prototype and a systematic methodology to optimize the electrical interconnection of DACPV module for solving the non-uniform solar illumination problem that restrains the electrical performance of solar cells. The research objectives of theoretical and experimental study in optimizing the electrical performance of DACPV system, as specified in Chapter 1, have been achieved. The major outcomes of this project are the design and development of an NIDC prototype, a new systematic method to optimize the layout of solar cells interconnection circuit in DACPV module, and the design and development of a high concentrated solar flux scanner. In conclusion, this research is confirmed to be capable of improving the output of solar cells with inhomogeneous illumination with a significant improvement in the electrical performance of DACPV system.

The main future works related to this research are descripted as follows:

- For the validation of the model with respect to the effects (deterioration in solar flux distribution and output power of solar cells) of circumsolar radiation, slope error and optical misalignment, it is desirable to assemble a DACPV module that is designed based on the optimal configuration V in the future.

- Future work could design an accurate, inexpensive and fast approach to align the flat facet mirrors of NIDC for eliminating the effect of optical misalignment on the solar flux distribution.

- It is also necessary to apply similar research approach on a bigger size of NIDC in order to find the most optimized DACPV system.

REFERENCES

Allegro, 2012. Fully Integrated, Hall Effect-Based Linear Current Sensor IC with 2.1 kVRMS Isolation and a Low-Resistance Current Conductor. ACS713 datasheet.

Andreev, V., Grilikhes, V., Rumyantsev, V., Timoshina, N. and Shvarts, M., 2003. Effect of nonuniform light intensity distribution on temperature coefficients of concentrator solar cells. *3rd World Conference on Photovoltaic Energy Conversion*, 2003, pp. 881-884.

Araki, K., and Yamaguchi, M., 2003. Influences of spectrum change to 3-junction concentrator cells. *Solar Energy Materials and Solar Cells*, 75, pp.707–714.

Baig, H., Heasman, K.C. and Mallick, T.K., 2012. Non-uniform illumination in concentrating solar cells. *Renewable and Sustainable Energy Reviews*. 16 (8), 5890–5909.

Ballestr ń, J. et al., 2003. Systematic error in the measurement of very high solar irradiance. *Solar Energy Materials and Solar Cells*, 80, pp. 375–381.

Ballestr ń, J. et al., 2004. High-heat-flux sensor calibration using calorimetry. *Metrologia*, 41(4), pp.314–318.

Bett, A.W., Dimroth, F., and Siefer, G., 2007. Multijunction Concentrator Solar Cells. In: *Concentrator Photovoltaics*. pp.67–87.

Blanc, P. et al., 2014. Direct normal irradiance related definitions and applications: The circumsolar issue. *Solar Energy*, 110, pp.561–577.

Bonnet-Eymard, M. et al., 2013. Optimized short-circuit current mismatch in multi-junction solar cells. *Solar Energy Materials and Solar Cells*, 117, pp.120–125.

Buie, D., Dey, C.J., and Bosi, S., 2003a. The effective size of the solar cone for solar concentrating systems. *Solar Energy*, 74(2003), pp.417–427.

Buie, D., Monger, a. G., and Dey, C.J., 2003b. Sunshape distributions for terrestrial solar simulations. *Solar Energy*, 74(2003), pp.113–122.

Chong, K.K. and Wong, C.W., 2009. General formula for on-axis sun-tracking system and its application in improving tracking accuracy of solar collector. *Solar Energy*, 83, pp. 298–305.

Chong, K.K, and Wong, C.W., 2010. General Formula for On-Axis Sun-Tracking System. In: *Solar Collectors and Panels, Theory and Applications*. p.444.

Chong, K.K. and Yew, T.K., 2011. Novel optical scanner using photodiodes array for two-dimensional measurement of light flux distribution. *IEEE Trans. Instrum. Meas.*, 60, pp. 2918–2925.

Chong, K.K. et al.,, 2009a. Integration of an on-axis general sun-tracking formula in the algorithm of an open-loop sun-tracking system. *Sensors,* 9, pp. 7849–7865.

Chong, K.-K., and Siaw, F.-L., 2012. Electrical characterization of dense-array concentrator photovoltaic system. In: *27th European Photovoltaic Solar Energy Conference and Exhibition*. pp.224–227.

Chong, K.K., Lau, S.L., Yew, T.K. and Tan, P.C.L., 2013a. Design and development in optics of concentrator photovoltaic system. *Renew. Sustain. Energy Rev*., 19, pp. 598 – 612

Chong, K.K., Siaw, F.L., Wong, C.W. and Wong, G.S., 2009b. Design and construction of non-imaging planar concentrator for concentrator photovoltaic system. *Renewable Energy*, 34, pp. 1364–1370.

Chong, K.-K., Tan, W.-C., and Wong, C.-W., 2012a. Second prototype non-imaging planar concentrator for concentrator photovoltaic system. In: *27th European Photovoltaic Solar Energy Conference and Exhibition*. 2012 pp. 257–259.

Chong, K.K., Wong, C.W., Siaw, F.L. and Yew, T.K., 2010. Optical Characterization of Nonimaging Planar Concentrator for the Application in Concentrator Photovoltaic System. *Journal of Solar Energy Engineering*, 132, 011011.

Chong, K.K., Wong, C.W., Yew, T.K. and Tan, M.H., 2012b. Solar concentrator assembly. Malaysian Patent No. PI 2012002439 (pending).

Chong, K.K., Wong, C.W., Yew, T.K. and Tan, M.H., 2013b. Solar concentrator assembly. U.S. Patent Application 13/901,519 (pending).

Chong, K.K., Yew, T.K., Wong, C.W. and Lau, S.L., 2011. Study of image quality of mirror via solar flux distribution measurement using a high speed optical scanner. *Applied Optics*, 50, pp. 4927–4935.

Cooper, T., Pravettoni, M., Cadruvi, M., Ambrosetti, G. and Steinfeld, A., 2013. The effect of irradiance mismatch on a semi-dense array of triple-junction concentrator cells. *Solar Energy Materials and Solar Cells*, 116, pp. 238–251.

Coventry, J.S., 2005. Performance of a concentrating photovoltaic/thermal solar collector. Solar Energy, 78, pp. 211-222.

EMCORE Corporation, 2008. Triple-junction high efficiency solar cells for terrestrial concentrated photovoltaic applications. EMCORE Photovoltaics datasheet.

Estrada, C.A., Jaramillo, O.A., Acosta, R. and Arancibia-Bulnes, C.A., 2007. Heat transfer analysis in a calorimeter for concentrated solar radiation measurements. *Solar Energy*, 81, pp. 1306–1313.

Faiman, D., Biryukov, S., and Pearlmutter, K.K., May 2002. PETAL: A research pathway to fossil-competitive solar electricity. 29th IEEE Photovoltaic Specialist Conference, New Orleans, USA, pp. 1384-1387.

Fernández-Reche, J. et al., 2008. Concentrating PV: An Alternative to Calorimeters for Measuring High Solar Flux Densities. *Journal of Solar Energy Engineering*, 130(4), p.044502.

Franklin, E.T., and Coventry, J.S., 2002. Effects of highly non-uniform illumination distribution on electrical performance of solar cells. ANSES Solar Conference. New Castle, Australia, pp. 1-8.

Green, M.A., Emery, K., Hishikawa, Y., Warta, W. and Dunlop, E.D., 2015. Solar cell efficiency tables (version 46). *Prog. Photovoltaics Res. Appl*., 23, pp. 805 – 812.

Haueter, P., Seitz, T. and Steinfeld, A., 1999. A New High-Flux Solar Furnace for High-Temperature Thermochemical Research. *Journal of Solar Energy Engineering*, 121, pp. 77.

Heinloth, K. (eds.), 2006, Energy Technologies Subvolume C: Renewable Energy, Springer, New York, pp. 242–278.

Johnston , G. and Shortis, M., 1997. Photogrammetry: an available surface characterization tool for solar concentrators, Part II: Assessment of surfaces. *Journal of Solar Energy Engineering*, 119(4), pp. 286–291.

Johnston, G., 1995. On the Analysis of Surface Error Distributions on Concentrated Solar Collectors. *Journal of Solar Energy Engineering*, 117(4), pp. 294–296

Johnston, G., Lovegrove, K., and Luzzi, A., 2003. Optical performance of spherical reflecting elements for use with paraboloidal dish concentrators. *Solar Energy*, 74(2), pp.133–140.

Joint Committee for Guides in Metrology (JCGM), 2008. Evaluation of measurement data: Guide to the expression of uncertainty in measurement.

Ju, X., Vossier, A., Wang, Z., Dollet, A., and Flamant, G., 2013. An improved temperature estimation method for solar cells operating at high concentrations. *Solar Energy*, 93, pp. 80-89.

Karatepe, E., Boztepe, M., and Çolak, M., 2007. Development of a suitable model for characterizing photovoltaic arrays with shaded solar cells. *Solar Energy*, 81(8), pp.977–992.

Kaushika, N.D., and Rai, A.K., 2007. An investigation of mismatch losses in solar photovoltaic cell networks. *Energy*, 32, pp.755–759.

King, R.R. et al., 2010. Band gap-voltage offset and energy production in next-generation multijunction solar cells. *Progress in Photovoltaics: Research and Applications*, 19(7), pp.6–11.

Kreske, K., 2002. Optical design of a solar flux homogenizer for concentrator photovoltaics. *Applied Optics*, 41(10), p.2053.

Kurtz, S., Emery, K., 2015. Conversion efficiencies of best research solar cells worldwide from 1976 through 2015 for various photovoltaic technologies [Online]. Available at: https://commons.wikimedia.org/wiki/File:PVeff(rev150806).jpg [Accessed: 8 November 2015].

Kussul, E. et al., 2008. Micro-facet solar concentrator. *Int. J. Sustain. Energy*, 27, pp. 61 – 71.

Liu, Y., Dai, J.M., Sun, X.G. and Yu,T.H., 2006. Factors influencing flux distribution on focal region of parabolic concentrators. In: *Proceeding of International Symposium on Instrumentation Science and Technology,* IOP Science, pp. 59-63.

Löckenhoff, R., Kubera, T., and Rasch, K.D., 2010. Water Cooled TJ Dense Array Modules for Parabolic Dishes. *Power*, 6, pp.9–12.

Luque, A. L. and Andreev, V. M. (eds.), 2007, Concentrator Photovoltaics, Springer, New York, pp. 113–132.

Luque, A., Sala, G., and Luque-Heredia, I., 2006. Photovoltaic concentration at the onset of its commercial deployment. *Progress in Photovoltaics: Research and Applications*, 14(5), pp.413–428.

März, T., Prahl, C., Ulmer, S., Wilbert, S., and Weber, C., 2011. Validation of Two Optical Measurement Methods for the Qualification of the Shape Accuracy of Mirror Panels for Concentrating Solar Systems. *Journal of Solar Energy Engineering*, 133(3), p.031022.

Mills, D.R., and Morrison, G.L., 2000. Compact Linear Fresnel Reflector solar thermal powerplants. *Solar Energy*, 68(3), pp.263–283.

Nishioka, K. et al., 2006. Evaluation of InGaP/InGaAs/Ge triple-junction solar cell and optimization of solar cell's structure focusing on series resistance for high-efficiency concentrator photovoltaic systems. *Solar Energy Materials and Solar Cells*, 90, pp. 1308–1321.

Noring, J.E., Grether, D.F. and Hunt, A.J., 1991. Circumsolar radiation data: the Lawrence Berkeley Laboratory reduced data base" In: National Renewable

Energy Laboratory. NREL/TP-262-4429 [Online]. Available at: http://rredc.nrel.gov/solar/pubs/circumsolar/title.html [Accessed: 15 December 2015].

Ota, Y., and Nishioka, K., 2012. Three-dimensional simulating of concentrator photovoltaic modules using ray trace and equivalent circuit simulators. *Solar Energy*, 86(1), pp.476–481.

Parretta, A. et al., 2007. Double-cavity radiometer for high-flux density solar radiation measurements. *Applied Optics*, 46, pp. 2166–2179.

Parretta, A., Privato, C., Nenna, G., Antonini, A. and Stefancich, M., 2006. Monitoring of concentrated radiation beam for photovoltaic and thermal solar energy conversion applications. Applied Optics, 45, pp. 7885–7897.

Philipps, S.P., Bett, A.W., Horowitz, K. and Kurtz, S., 2015. Current Status of Concentrator Photovoltaic (CPV) Technology [Online]. Available at: http://www.ise.fraunhofer.de/en/publications/veroeffentlichungen-pdf-dateien-en/studien-und-konzeptpapiere/current-status-of-concentrator-photovoltaic-cpv-technology.pdf [Accessed: 8 December 2015].

Philipps, S.P., Dimroth, F. and Bett, A.W., 2012. High-Efficiency III-V Multijunction Solar Cells, *in Practical Handbook of Photovoltaics*. pp. 417–448.

Picault, D., Raison, B., Bacha, S., de la Casa, J., and Aguilera, J., 2010. Forecasting photovoltaic array power production subject to mismatch losses. *Solar Energy*, 84(7), pp.1301–1309.

Pottler, K., Lüpfert, E.,, Johnston, G. and Shortis, M.R., 2005. Photogrammetry: A Powerful Tool for Geometric Analysis of Solar Concentrators and Their Components. *Journal of Solar Energy Engineering*, 127(1), pp. 94-101.

Pravettoni, M., Virtuani, A., Keller, K., Apolloni, M. and Müllejans, H., 2013. Spectral Mismatch Effect to the Open-circuit Voltage in the Indoor Characterization of Multi-junction Thin-film Photovoltaic Modules, *in: Conference Record of the 2013 IEEE 39th Photovoltaic Specialists Conference (PVSC).* pp. 706–711.

Reis, F., Pravettoni, M., Wemans, J., Sorasio, G. and Brito, M.C., 2013. Modelling the effects of inhomogeneous irradiation and temperature profiles on CPV cells behaviour. *IEEE J. Photovoltaics*, 5, pp. 112–122.

Ries, H., Gordon, J.M., and Lasken, M., 1997. High-flux photovoltaic solar concentrators with kaleidoscope-based optical designs. *Solar Energy*, 60(1), pp.11–16.

Röger, M. et al., 2014. Techniques to Measure Solar Flux Density Distribution on Large-Scale Receivers. *Journal of Solar Energy Engineering*, 136, pp. 031013.

Ryu, K., Rhee, J.G., Park, K.M., and Kim, J., 2006. Concept and design of modular Fresnel lenses for concentration solar PV system. *Solar Energy*, 80(12), pp.1580–1587.

Salomé, A., Chhel, F., Flamant, G., Ferrière, A. and Thiery, F., 2013. Control of the flux distribution on a solar tower receiver using an optimized aiming point strategy: Application to THEMIS solar tower. *Solar Energy*, 94, pp. 352–366.

Segev, G., and Kribus, A., 2013. Performance of CPV modules based on vertical multi-junction cells under non-uniform illumination. *Solar Energy*, 88, pp.120–128.

Segev, G., and Kribus, A., 2013. Performance of CPV modules based on vertical multi-junction cells under non-uniform illumination. *Solar Energy*, 88, pp.120–128.

Sharaf, O.Z. and Orhan, M.F., 2015. Concentrated photovoltaic thermal (CPVT) solar collector systems: Part I — Fundamentals, design considerations and current technologies. *Renewable and Sustainable Energy Reviews*. 50 (2015), 1500–1565.

Sherif, R., Cotal, H., Paredes, A., Lewandowski, A., Bingham, C. and Mehos, M., 2003. High concentration tests of a dense PV array using GaInP/GaAs/Ge triple-junction cells in the high flux solar furnace. 3rd World Conference on Photovoltaic Energy Conversion, Osaka, Japan, pp. 829-832.

Siaw, F.L. and Chong, K.K., 2012. Temperature effects on the performance of dense-array concentrator photovoltaic system. In: *Proceedings of the IEEE Conference on Sustainable Utilization and Development in Engineering and Technology* (IEEE, 2012), pp. 140–144.

Siaw, F.L. and Chong, K.K., 2013. A systematic method of interconnection optimization for dense-array concentrator photovoltaic system. *Sci. World J.*, 2013, pp. 1-11.

Siaw, F.L., Chong, K.K. and Wong, C.W., 2014. A comprehensive study of dense-array concentrator photovoltaic system using non-imaging planar concentrator. *Renewable Energy*, 62, pp. 542–555.

Spectrolab, Inc., 2010. CPV Dense Array Solar Cells. Spectrolab, Inc. datasheet.

Tan, M.-H., Chong, K.-K., Wong and C.-W., 2014. Optical characterization of nonimaging dish concentrator for the application of dense-array concentrator photovoltaic system. *Applied Optics*, 53, pp. 475–86.

Ulmer, S., Heller, P., and Reinalter, W., 2008. Slope Measurements of Parabolic Dish Concentrators Using Color-Coded Targets. *Journal of Solar Energy Engineering*, 130(1), p.011015.

Ulmer, S., Reinalter, W., Heller, P., Lüpfert, E. and Martínez, D., 2002. Beam Characterization and Improvement with a Flux Mapping System for Dish Concentrators. Journal of Solar Energy Engineering, 124, pp. 182.

Verlinden, P.J et al., 2006. Performance and reliability of multijunction III-V modules for concentrator dish and central receiver applications, *in: Conference Record of the 2006 IEEE 4th World Conference on Photovoltaic Energy Conversion, WCPEC-4*. pp. 592–597.

Vivar, M., Antón, I., and Sala, G., 2010. Radial CPV receiver. *Progress in Photovoltaics: Research and Applications*, 18(5), pp.353–362.

Vivar, M., Morilla, C., Antón, I., and Sala, G., 2009. Si-cells radial parquet for parabolic dish receivers. In: *Proceedings of the 24th European Photovoltaic Solar Energy Conference*, Hamburg, Germany, September 2009, pp. 141–144.

Vossier, A., Chemisana, D., Flamant, G., and Dollet, A., 2012. Very high fluxes for concentrating photovoltaics: Considerations from simple experiments and modeling. *Renewable Energy*, 38(1), pp.31–39.

Wang, Z., Zhang, H., Wen, D., Zhao, W., and Zhou, Z., 2013. Characterization of the InGaP/InGaAs/Ge triple-junction solar cell with a two-stage dish-style concentration system. *Energy Conversion and Management*, 76, pp.177–184.

Winston, R., Minano, J. C., and Benitez, P., 2005, Non-Imaging Optics, Elsevier, New York, pp. 1–6.

Wong, C.-W., Chong, K.-K. and Tan, M.-H., 2015. Performance optimization of dense-array concentrator photovoltaic system considering effects of circumsolar radiation and slope error. *Optics Express,* 23, pp. A841.

Wong, C.-W., and Chong, K.-K., 2016. Solar flux distribution study of non-imaging dish concentrator using linear array of triple-junction solar cells scanning technique *Solar Energy,* 125, pp. 86-98.

APPENDIX A

A.1 Main

```
clc
clear

SE = 0e-3;            % Mirror Slope Error Value
CSR = 0.0001;         % Circumsolar Ratio Value
AE = 0.0;             % Optical Misalignment Value

tic;    % Start Timer

% ========== Call function ==========
Initial()
Coordinate()
Rotate_Mirror()

% ========== Determine flux distribution ==========
data=zeros(PixSize);

for i=1:1:m
   for j=1:1:n
      for k=1:1:g
         for l=1:1:h
            SolarRay()
            weight = N{i,j,k,l}(3)/total;       % Get the weightage of Ray
            data=data+flux*weight;
         end
      end
   end
end

toc;    % End Timer

% ========== Plot flux distribution ==========
x=[1:PixSize];
y=[1:PixSize];

[X,Y]= meshgrid(x,y);
figure()
mesh((X-(PixSize/2+0.5))*TargetSize/PixSize,(Y-
(PixSize/2+0.5))*TargetSize/PixSize,data);
```

A.2 Initial()

```
% ========= Input ==========

alfa_1= 0.00465;                % Solar disc half angle (radian)
alfa_2= 0.0436;                 % Sun-shape half angle (radian)
m = 4;                          % No of mirrors in row
n = 24;                         % No of mirrors in column
MirrorSize = 20;                % Mirror size (cm)
m_MirrorRes = 201;              % Mirror resolution (Odd Num)
m_nR =101;                      % Solar disc resolution (Odd Num)
TargetSize = 40;                % Target size (cm)
L = 210.0;                      % Target distance (cm)
PixSize = 401;                  % Target Pixel Size


% ========== Initialize ==========
PI = 3.14159265358979323846264338327 95;
mc = (m + 1)/2;                 % Central mirror in row
nc = (n + 1)/2;                 % Central mirror in column
g = m_MirrorRes;                % No of Rays along mirror in row
h = m_MirrorRes;                % No of Rays along mirror in column
gc = (g - 1)/2;                 % Central Ray along rows
hc = (h - 1)/2;                 % Central Ray along columns
MirrorRes1 = MirrorSize/(g-1);  % Mirror resolution in row
MirrorRes2 = MirrorSize/(h-1);  % Mirror resolution in column
scale = PixSize/TargetSize;     % pixel per cm
TargetRes = TargetSize/PixSize; % cm per pixel

PixConcentration = (MirrorRes1*MirrorRes2)/TargetRes^2;

I=[0 0 1 1]';                   % Incident ray
Normal=[0 0 1 1]';              % Initial normal unit vector


delta = (alfa_2)/(m_nR + 0.5);  % Interval angles for subray (radian)

k1=0.9*log(13.5*CSR)*CSR^(-0.3);        % Parameter 1 for sun-shape
k2=2.2*log(0.52*CSR)*CSR^(0.43)-0.1;    % Parameter 2 for sun-shape
```

A.3 Coordinate()

```
% Quater1
% Row#1 (x5)
Hc{1,1}= [30.75; 14.25; 1.69];
Hc{1,2}= [10.25; 34.75; 1.93];
Hc{1,3}= [30.75; 34.75; 3.17];
Hc{1,4}= [51.25; 34.75; 5.64];
Hc{1,5}= [51.25; 14.25; 4.16];


% Row#2 (x5)
Hc{1,6}= [10.25; 55.25; 4.64];
Hc{1,7}= [30.75; 55.25; 5.88];
Hc{1,8}= [51.25; 55.25; 8.35];
Hc{1,9}= [71.75; 55.25; 12.06];
Hc{1,10}=[71.75; 34.75; 9.35];


% Row#3 (x5)
Hc{1,11}=[71.75; 14.25; 7.87];
Hc{1,12}=[10.25; 75.75; 8.59];
Hc{1,13}=[30.75; 75.75; 9.83];
Hc{1,14}=[51.25; 75.75; 12.30];
Hc{1,15}=[71.75; 75.75; 16];


% Row#4 (x5)
Hc{1,16}=[92.25; 75.75; 20.95];
Hc{1,17}=[92.25; 55.25; 17];
Hc{1,18}=[92.25; 34.75; 14.29];
Hc{1,19}=[92.25; 14.25; 12.81];
Hc{1,20}=[10.25; 96.25; 13.78];


% Row#5 (x4)
Hc{1,21}=[30.75; 96.25; 15.01];
Hc{1,22}=[51.25; 96.25; 17.49];
Hc{1,23}=[71.75; 96.25; 21.19];
Hc{1,24}=[92.25; 96.25; 26.14];
```

```
for j=1:1:n

   % Quater2
   Hc{3,j}=[-Hc{1,j}(1)
             Hc{1,j}(2)
             Hc{1,j}(3)];

   % Quater3
   Hc{2,j}=[Hc{1,j}(1)
           -Hc{1,j}(2)
            Hc{1,j}(3)];

   % Quater4
   Hc{4,j}=[-Hc{1,j}(1)
            -Hc{1,j}(2)
             Hc{1,j}(3)];
end
```

A.4 Rotate_Mirror()

```
%===== Set the reflective points coordinate after mirror alignment =====
for i=1:1:m
   for j=1:1:n

      % Overlap all the mirror images at target (0,0)
      CentralRay=[Hc{i,j}(1)
                  Hc{i,j}(2)
                  L - Hc{i,j}(3)];

      % Rotational angle along y-axis
      Sigma=atan(Hc{i,j}(1)/sqrt((Hc{i,j}(1))^2+2*(Hc{i,j}(2))^2+2*(L -
            Hc{i,j}(3))^2+2*(L - Hc{i,j}(3)) *
            sqrt(dot(CentralRay,CentralRay))));

      % Rotational angle along x-axis
      Gamma=atan(Hc{i,j}(2)/((L - Hc{i,j}(3)) +
               sqrt(dot(CentralRay,CentralRay))));

      % Transformation
      MatYSigma = makehgtform('yrotate',-
                    (Sigma+(cos(PI*rand(1))*(AE/180*PI))));
      MatXGamma = makehgtform('xrotate',Gamma+
                    (cos(PI*rand(1))*(AE/180*PI)));

     % Translation
      MatTrans1 =  makehgtform('translate',-Hc{i,j});
      MatTrans2 =  makehgtform('translate',Hc{i,j});

      for k=1:1:g
         for l=1:1:h

            % Reflective point
            H{i,j,k,l}=[Hc{i,j}(1)+MirrorSize*(gc -(k-1))/(g-1)
                        Hc{i,j}(2)+MirrorSize*(hc -(l-1))/(h-1)
                        Hc{i,j}(3)
                        1];




            % Slope error first angle
            Theta =((-2*SE^2)*log(1-rand(1)))^0.5;

            % Slope error second angle
            Phi = 2*PI*rand(1);

            % Transformation
            MatXTheta = makehgtform('xrotate',Theta);
```

```
            MatZPhi = makehgtform('zrotate',Phi);

            % New normal unit vector;
            N{i,j,k,l}=MatXGamma*(MatYSigma*(MatZPhi*(MatXTheta
                  *Normal)));

            % Rotated mirror to new position
            H{i,j,k,l}=MatTrans2*(MatXGamma*(MatYSigma
                  *(MatTrans1*H{i,j,k,l})));
         end
      end
   end
end
```

A.5 SolarRay()

```
%Get the directional vector of Master ray
MDir=(2*N{i,j,k,l}(3))*N{i,j,k,l} - I;

%Normalize the reflected ray
RayDir = MDir/(MDir(1)^2+MDir(2)^2+MDir(3)^2)^0.5;

beta = atan(RayDir(2)/sqrt((RayDir(1)^2+RayDir(3)^2)));
alpha = atan(RayDir(1)/RayDir(3));

if(RayDir(3)<0.0)
   alpha=PI+alpha;
end

c1=cos(beta); s1=sin(beta); c2=cos(alpha); s2=sin(alpha);
MatToZ=[1 0 0 0; 0 c1 -s1 0;0 s1 c1 0; 0 0 0 1]* [c2 0 -s2 0; 0 1  0 0; s2 0 c2
            0; 0 0  0 1];

IZ = inv(MatToZ);
z =(MatToZ * RayDir);
z3=z(3);

% Parameters used to calculate reflected ray
IZ1=IZ(1);IZ2=IZ(2);IZ3=IZ(3);IZ4=IZ(4);IZ5=IZ(5);
IZ6=IZ(6);IZ7=IZ(7);IZ8=IZ(8);IZ9=IZ(9);IZ10=IZ(10);
IZ11=IZ(11);IZ12=IZ(12);IZ13=IZ(13);IZ14=IZ(14);IZ15=IZ(15);

% Parameters used to calculate intersection point on the target
c1=L-H{i,j,k,l}(3);
H1=H{i,j,k,l}(1);
H2=H{i,j,k,l}(2);

MaxR_1 = abs(tan(z3*alfa_1));        % Maximum radius for solar disc
MaxR_2 = abs(tan(z3*alfa_2));        % Maximum radius for sun-shape

CountRay=1;
flux=zeros(PixSize);
total=0;

for xa=-m_nR:1:m_nR
   for ya=-m_nR:1:m_nR
      px = (xa + 0.5) * delta;
      py = (ya + 0.5) * delta;
      mag = sqrt(px^2 + py^2);
      tt=1000*mag/z3;

      if mag <= MaxR_2
```

```
        %Normalize the reflecred subray
        Dir{CountRay}=new/(new(1)^2+new(2)^2+new(3)^2)^2;
        Dir_x=IZ1*px+IZ5*py+IZ9*z3+IZ13;
        Dir_y=IZ2*px+IZ6*py+IZ10*z3+IZ14;
        Dir_z=IZ3*px+IZ7*py+IZ11*z3+IZ15;

        % Intersection point on the target
        Cx = fix((c1*Dir_x/Dir_z+ H1)*scale + 0.5*PixSize);
        Cy = fix((c1*Dir_y/Dir_z+ H2)*scale + 0.5*PixSize);

        if mag<=MaxR_1

                % Sunshape normalize magnitude
                SS = cos(0.326*tt)/cos(0.308*tt);
        else
                % Sunshape normalize magnitude
                SS =(tt^k2)*exp(k1);
        end

        total = total+SS;
        xx = Cx+Cy*PixSize;
        flux(xx) = flux(xx)+PixConcentration*SS;
        CountRay = CountRay + 1;
      end
    end
end
```